

Wireless Communications and Mobile Computing

Channel Modeling and Simulation for Vehicular Communications

Lead Guest Editor: Carlos A. Gutiérrez

Guest Editors: Rafael Perez-Jimenez, José M. Luna-Rivera, Neji Youssef,
and Jose Rabadán





Channel Modeling and Simulation for Vehicular Communications

Wireless Communications and Mobile Computing

Channel Modeling and Simulation for Vehicular Communications

Lead Guest Editor: Carlos A. Guti rrez

Guest Editors: Rafael Perez-Jimenez, Jos  M. Luna-Rivera,
Neji Youssef, and Jose Rabad n



Copyright © 2018 Hindawi. All rights reserved.

This is a special issue published in “Wireless Communications and Mobile Computing.” All articles are open access articles distributed under the Creative Commons Attribution License, which permits unrestricted use, distribution, and reproduction in any medium, provided the original work is properly cited.

Editorial Board

- Javier Aguiar, Spain
Wessam Ajib, Canada
Muhammad Alam, China
Eva Antonino-Daviu, Spain
Shlomi Arnon, Israel
Leyre Azpilicueta, Mexico
Paolo Barsocchi, Italy
Alessandro Bazzi, Italy
Zdenek Becvar, Czech Republic
Francesco Benedetto, Italy
Olivier Berder, France
Ana M. Bernardos, Spain
Mauro Biagi, Italy
Dario Bruneo, Italy
Jun Cai, Canada
Zhipeng Cai, USA
Claudia Campolo, Italy
Gerardo Canfora, Italy
Rolando Carrasco, UK
Vicente Casares-Giner, Spain
Luis Castedo, Spain
Ioannis Chatzigiannakis, Greece
Lin Chen, France
Yu Chen, USA
Hui Cheng, UK
Ernestina Cianca, Italy
Riccardo Colella, Italy
Mario Collotta, Italy
Massimo Condoluci, Sweden
Daniel G. Costa, Brazil
Bernard Cousin, France
Telmo Reis Cunha, Portugal
Igor Curcio, Finland
Laurie Cuthbert, Macau
Donatella Darsena, Italy
Pham Tien Dat, Japan
André de Almeida, Brazil
Antonio De Domenico, France
Antonio de la Oliva, Spain
Gianluca De Marco, Italy
Luca De Nardis, Italy
Liang Dong, USA
Mohammed El-Hajjar, UK
Oscar Esparza, Spain
- Maria Fazio, Italy
Mauro Femminella, Italy
Manuel Fernandez-Veiga, Spain
Gianluigi Ferrari, Italy
Ilario Filippini, Italy
Jesus Fontecha, Spain
Luca Foschini, Italy
A. G. Fragkiadakis, Greece
Sabrina Gaito, Italy
Óscar García, Spain
M. García Sánchez, Spain
L. J. García Villalba, Spain
José A. García-Naya, Spain
Miguel Garcia-Pineda, Spain
A.-J. García-Sánchez, Spain
Piedad Garrido, Spain
Vincent Gauthier, France
Carlo Giannelli, Italy
Carles Gomez, Spain
Juan A. Gomez-Pulido, Spain
Ke Guan, China
Antonio Guerrieri, Italy
Daojing He, China
Paul Honeine, France
Sergio Ilarri, Spain
Antonio Jara, Switzerland
Xiaohong Jiang, Japan
Minho Jo, Republic of Korea
Shigeru Kashiara, Japan
Dimitrios Katsaros, Greece
Minseok Kim, Japan
Mario Kolberg, UK
Nikos Komninos, UK
Juan A. L. Riquelme, Spain
Pavlos I. Lazaridis, UK
Tuan Anh Le, UK
Xianfu Lei, China
Hoa Le-Minh, UK
Jaime Lloret, Spain
M. López-Benítez, UK
M. López-Nores, Spain
Javier D. S. Lorente, Spain
Tony T. Luo, Singapore
Maode Ma, Singapore
- Imadeldin Mahgoub, USA
Pietro Manzoni, Spain
Álvaro Marco, Spain
Gustavo Marfia, Italy
Francisco J. Martinez, Spain
Davide Mattera, Italy
Michael McGuire, Canada
Nathalie Mitton, France
Klaus Moessner, UK
Antonella Molinaro, Italy
Simone Morosi, Italy
Kumudu S. Munasinghe, Australia
Enrico Natalizio, France
Keivan Navaie, UK
Thomas Newe, Ireland
Wing Kwan Ng, Australia
Tuan M. Nguyen, Vietnam
Petros Nicopolitidis, Greece
Giovanni Pau, Italy
R. Pérez-Jiménez, Spain
Matteo Petracca, Italy
Nada Y. Philip, UK
Marco Picone, Italy
Daniele Pinchera, Italy
Giuseppe Piro, Italy
Vicent Pla, Spain
Javier Prieto, Spain
R. C. Pryss, Germany
Sujan Rajbhandari, UK
Rajib Rana, Australia
Luca Reggiani, Italy
Daniel G. Reina, Spain
Abusayeed Saifullah, USA
Jose Santa, Spain
Stefano Savazzi, Italy
Hans Schotten, Germany
Patrick Seeling, USA
Muhammad Z. Shakir, UK
Mohammad Shojafar, Italy
Giovanni Stea, Italy
E. Stevens-Navarro, Mexico
Zhou Su, Japan
Luis Suarez, Russia
Ville Syrjälä, Finland



Hwee Pink Tan, Singapore
Pierre-Martin Tardif, Canada
Mauro Tortonesi, Italy
Federico Tramarin, Italy
Reza Monir Vaghefi, USA

J. F. Valenzuela-Valdés, Spain
Aline C. Viana, France
Enrico M. Vitucci, Italy
Honggang Wang, USA
Jie Yang, USA

Sherali Zeadally, USA
Jie Zhang, UK
Meiling Zhu, UK

Contents

Channel Modeling and Simulation for Vehicular Communications

Carlos A. Gutiérrez , Rafael Perez-Jimenez, José Martín Luna-Rivera , Neji Youssef,
and Jose Rabadán-Borges

Editorial (2 pages), Article ID 8765650, Volume 2018 (2018)

Statistical Modeling, Simulation, and Experimental Verification of Wideband Indoor Mobile Radio Channels

Yuanyuan Ma , Bjørn Olav Hogstad , Matthias Pätzold , and Pedro M. Crespo

Research Article (13 pages), Article ID 8271765, Volume 2018 (2018)

Modelling and Analysis of Nonstationary Vehicle-to-Infrastructure Channels with Time-Variant Angles of Arrival

Matthias Pätzold  and Carlos A. Gutierrez 

Research Article (9 pages), Article ID 6396173, Volume 2018 (2018)

A Triply Selective MIMO Channel Simulator Using GPUs

R. Carrasco-Alvarez , R. Carreón-Villal, J. Vázquez Castillo , J. Ortegón Aguilar, O. Longoria-Gandara,
and A. Castillo Atoche

Research Article (9 pages), Article ID 3517489, Volume 2018 (2018)

A Novel Simulation Model for Nonstationary Rice Fading Channels

Kaili Jiang, Xiaomin Chen , Qiuming Zhu , Lele Chen, Dazhuan Xu, and Bing Chen 

Research Article (9 pages), Article ID 8086073, Volume 2018 (2018)

Editorial

Channel Modeling and Simulation for Vehicular Communications

Carlos A. Gutiérrez ¹, **Rafael Perez-Jimenez**,² **José Martín Luna-Rivera** ¹,
Neji Youssef,³ and **Jose Rabadán-Borges**²

¹Faculty of Science, Universidad Autónoma de San Luis Potosí, San Luis Potosí, Mexico

²IDeTIC, Universidad de las Palmas de Gran Canaria, Las Palmas, Gran Canaria, Spain

³Ecole Supérieure des Communications de Tunis, Université de Carthage, Ariana, Tunisia

Correspondence should be addressed to Carlos A. Gutiérrez; cagutierrez@ieee.org

Received 23 September 2018; Accepted 23 September 2018; Published 18 October 2018

Copyright © 2018 Carlos A. Gutiérrez et al. This is an open access article distributed under the Creative Commons Attribution License, which permits unrestricted use, distribution, and reproduction in any medium, provided the original work is properly cited.

The interest that exists globally around the so-called intelligent transportation systems (ITS) has fostered a large amount of research activities aimed at developing new wireless communication technologies for the information exchange among vehicles on the move. The design of such technology gained an important momentum when in 1999 the American Federal Communications Commission (FCC) allocated a 75 MHz bandwidth in the 5.9 GHz band for dedicated short-range communications (DSRC) systems. The technology has seen a continuous development and the achievement of several milestones ever since. However, while the future ahead looks promising, the design of radio transceivers for vehicular communications continues to be a complex task, because the high speed at which the vehicles can move poses several new challenges that are not a concern for conventional mobile communication systems. For example, due to the rapidly changing propagation conditions that are typically found in vehicular communication environments, the Doppler shift effects and the nonstationary characteristics of the wireless channel become exacerbated. These issues significantly affect the performance of transceivers that are not optimized to operate over highly dispersive nonstationary channels. Proper channel models are therefore needed that provide insights into the physics of vehicle-to-vehicle (V2V) and vehicle-to-infrastructure (V2I) radio reception and, at the same time, that lend themselves to

mathematical and numerical system performance investigations.

This special issue aims to provide a global perspective on open problems, current research trends, new results and ideas, and hot topics in the area of channel modeling and simulation for vehicular communication systems. The special issue comprises a collection of four papers that were received from open call and accepted for publication after a thorough peer review.

In the paper entitled “Statistical Modeling, Simulation, and Experimental Verification of Wideband Indoor Mobile Radio Channels,” Y. Ma et al. present a geometry-based stochastic model for wideband indoor mobile radio channels. The model assumes that the transmitted signal is scattered by objects that are exponentially distributed over the two-dimensional horizontal plane of a rectangular room. Departing from this model, the authors investigate the probability density function (PDF) of the angle of arrival (AOA), the PDF of the path length, the power delay profile (PDP), and the frequency correlation function (FCF). In addition, they present an efficient sum-of-cisoids (SOC) channel simulator based on the proposed nonrealizable wideband indoor channel model. The channel model and its SOC simulator have been validated experimentally by empirical data collected in different indoor scenarios at 2.4, 5, and 60 GHz.

The design of computer simulators for nonstationary Rice fading channels under nonisotropic scattering scenarios is the subject of research of the paper “A Novel Simulation Model for Nonstationary Rice Fading Channels,” by K. Jiang et al. The authors of this paper present a simulation model based on sum-of-chirp signals that takes into account the smooth transition of fading phases between the adjacent channel states. They analyze the envelope and phase PDFs, autocorrelation function (ACF), and Doppler power spectrum density (DPSD) of the proposed simulator, and they also introduce a proper parameterization method for such simulator. Simulation results are presented to demonstrate the accuracy of the simulator in replicating the statistical properties of the reference Rice fading channel model under nonstationary and nonisotropic scenarios.

In the paper entitled “A Triply Selective MIMO Channel Simulator Using GPUs,” R. Carrasco-Alvarez et al. present a novel methodology based on graphics processing units (GPUs) for the simulation of triply selective multiple-input multiple-output (MIMO) radio channels. Compared with sequential implementations, the proposed GPU-based channel simulator is shown to achieve a 650-fold computational time improvement for an 8×8 MIMO channel. In addition to the computational improvement, the proposed simulator offers flexibility for testing a variety of propagation scenarios in V2V and V2I communication systems.

Finally, the paper “Modelling and Analysis of Nonstationary Vehicle-to-Infrastructure Channels with Time-Variant Angles of Arrival,” by M. Pätzold and C. A. Gutierrez, deals with the statistical modeling of fixed-to-mobile (F2M) multipath radio channels with time-varying angular statistics. In the state of the art, it is commonly assumed that the AOA statistics of the received multipath signal are time invariant. However, this assumption does not in general agree with real-world channels in which the AOAs vary with the position of a moving receiver. In their paper, the authors present a mathematical model for the time-varying AOAs. This model is then employed as a basis for the development of two nonstationary multipath fading channels models for V2I communications. The time-dependent ACF, time-dependent mean Doppler shift, time-dependent Doppler spread, and the Wigner-Ville spectrum of the proposed V2I channel models are analyzed. All in all, this paper provides a new view on the channel characteristics that go beyond ultrashort observation intervals over which the channel can be considered as wide-sense stationary.

Conflicts of Interest

I hereby declare that I and the other Guest Editors of the Special Issue have no conflicts of interest or private agreements with companies or organizations, as described in <https://about.hindawi.com/managing-conflicts-of-interest/>.

Acknowledgments

The Guest Editors want to thank the Authors for submitting their papers to the special issue, and the anonymous

referees for their valuable contributions to the peer-review process.

Carlos A. Gutiérrez
Rafael Perez-Jimenez
José Martín Luna-Rivera
Neji Youssef
Jose Rabadán-Borges

Research Article

Statistical Modeling, Simulation, and Experimental Verification of Wideband Indoor Mobile Radio Channels

Yuanyuan Ma ¹, Bjørn Olav Hogstad ², Matthias Pätzold ³, and Pedro M. Crespo⁴

¹College of Information Science and Engineering, Shandong Agricultural University, Shandong 271018, China

²Department of Mathematical Science, Norwegian University of Science and Technology, Teknologiveien 22, 2815 Gjøvik, Norway

³Faculty of Engineering and Science, University of Agder, P.O. Box 509, 4898 Grimstad, Norway

⁴CEIT and Tecnun, University of Navarra, 20018 San Sebastián, Spain

Correspondence should be addressed to Yuanyuan Ma; mayuanyuan@sdau.edu.cn

Received 19 October 2017; Revised 10 January 2018; Accepted 31 January 2018; Published 19 March 2018

Academic Editor: Jose Rabadán

Copyright © 2018 Yuanyuan Ma et al. This is an open access article distributed under the Creative Commons Attribution License, which permits unrestricted use, distribution, and reproduction in any medium, provided the original work is properly cited.

This paper focuses on the modeling, simulation, and experimental verification of wideband single-input single-output (SISO) mobile fading channels for indoor propagation environments. The indoor reference channel model is derived from a geometrical rectangle scattering model, which consists of an infinite number of scatterers. It is assumed that the scatterers are exponentially distributed over the two-dimensional (2D) horizontal plane of a rectangular room. Analytical expressions are derived for the probability density function (PDF) of the angle of arrival (AOA), the PDF of the propagation path length, the power delay profile (PDP), and the frequency correlation function (FCF). An efficient sum-of-cisoids (SOC) channel simulator is derived from the nonrealizable reference model by employing the SOC principle. It is shown that the SOC channel simulator approximates closely the reference model with respect to the FCF. The SOC channel simulator enables the performance evaluation of wideband indoor wireless communication systems with reduced realization expenditure. Moreover, the rationality and usefulness of the derived indoor channel model is confirmed by various measurements at 2.4, 5, and 60 GHz.

1. Introduction

Indoor wireless communications has attracted considerable attention in recent years due to a broad set of emerging indoor services offered by personal communication systems [1, 2], wireless local area networks [3, 4], and wireless private branch exchange networks [5]. The interest in indoor wireless communications is growing especially when optical wireless communication techniques [6, 7] are applied to indoor deployment scenarios. Numerous researches on modulation techniques [8], multiple access techniques [9], and propagation modeling [10] have been carried out for indoor optical wireless communications. In order to design an efficient indoor wireless communication system and to predict accurately its system performance, a prerequisite is to develop an appropriate indoor channel model that describes realistically the underlying propagation conditions.

To improve the indoor channel characterization and modeling, numerous measurement campaigns have been conducted in a variety of indoor environments, such as

offices, corridors, buildings, and factory halls. Measurement results have been reported in the literature for various frequency bands, including the frequency bands at 900 MHz [11–13], 1.5 GHz [14, 15], 2.4 GHz [16], 4–5.5 GHz [17–19], 17–18 GHz [18, 20], and 60 GHz [21–24]. Based on measurement results, several empirical statistical channel models [13, 24–27] have been developed for the simulation and performance analysis of various indoor communication systems. The advantage of measurement-based channel models is that they are characterizing the fading behavior utterly realistic. By changing the model parameters, the developed statistical channel models can be employed to simulate indoor propagation channels for a broad range of different scenarios. However, to determine appropriate parameters for different propagation scenarios, a large number of measurement data are required, which is time- and material-consuming and leads thus to high development costs. Alternatively, approaches based on ray-tracing techniques [28–31] have been developed to enable the simulation of indoor

propagation channels. Ray-tracing channel models [29, 32–34] can efficiently capture the fading behavior of specified indoor environments. Many developed ray-tracing channel models have shown good agreement with measured channels [35–37]. However, ray-tracing models greatly depend on the physical layouts and materials through which electromagnetic waves propagate, for example, walls, floors, and ceilings. In addition, the main drawback of ray-tracing models comes from their computational costs, which are widely determined by the size and complexity of the geographic database as well as the strategy used for the ray search. Therefore, a trade-off has to be found between the prediction accuracy and the simulation efficiency when modeling indoor propagation channels using ray-tracing techniques.

The two main types of indoor channel models, namely, the empirical statistical channel models and the ray-tracing channel models, have their own strengths and limitations. To cope with the drawbacks mentioned above, a geometrical channel model has been proposed in [38] for indoor environments, where it is assumed that the scatterers are randomly distributed inside of a circle with a base station (BS) in its centre. More specifically, this model is based on the assumption that the distance between the BS and the scatterers follows an exponential distribution. Such an assumption imposes severe restrictions on the applicability of the model. In addition, from the physical point of view, it is questionable whether it is reasonable to represent the geometry of indoor scattering areas, such as offices and corridors, by a circle. On the contrary, a rectangle is a more appropriate geometric figure to model typical indoor propagation environments. A geometrical rectangle scattering model has been proposed in [39] to characterize narrowband indoor radio propagation channels. However, to the best of the authors' knowledge, the modeling of wideband indoor radio channels by employing an appropriate geometrical scattering model that takes into consideration the unique indoor propagation conditions is still an open problem.

Motivated by the scarcity of proper wideband geometry-based indoor channel models, such a model was developed in [40] by extending the geometrical rectangle scattering model in [39] with respect to frequency selectivity. In this paper, we improve the statistical models in [39–41] for the characterization of the scatterer distribution. We concentrate on the statistical characterization of a wideband reference channel model, which is based on the assumption that an infinite number of scatterers are randomly distributed over the two-dimensional (2D) horizontal plane of a rectangular room. To be more specific, we assume that the probability for the occurrence of a scatterer decays exponentially with the distance from the walls. This assumption includes the uniform distribution of the scatterers as a specific case. In contrast to [42–44], we apply a different procedure for studying the statistical properties of the resulting reference channel model, which requires no knowledge of the complex channel gain. We derive the analytical expressions for the probability density function (PDF) of the angle of arrival (AOA), the PDF of the propagation path length, the power delay profile (PDP), and the frequency correlation function (FCF). Moreover, we derive a wideband sum-of-cisoids

(SOC) channel simulator from the reference model. It is shown that the designed wideband SOC channel simulator matches the underlying reference model accurately with respect to the FCF. The obtained SOC channel simulator enables the simulation of indoor mobile fading channels with reduced realization expenditure. At the end, we demonstrate the closeness to reality of the proposed reference channel model by comparing its mean excess delay and the root mean square (RMS) delay spread with the corresponding empirical quantities obtained from measured channels in laboratories at 2.4 GHz [16] and a conference room at 5 GHz [19] as well as corridors and offices at 60 GHz [23].

The remainder of this paper is structured as follows. In Section 2, we introduce the 2D geometrical indoor scattering model, which serves as a starting point for the derivation of the reference channel model. Section 3 analyzes the statistical characteristics of the wideband reference channel model with emphasis on the PDF of the AOA, the PDF of the propagation path length, the PDP, and the FCF. Section 4 introduces a design procedure for wideband indoor SOC channel simulators. Numerical and experimental results are presented in Section 5 to confirm the correctness of the obtained theoretical results. Section 6 validates the usefulness of the proposed indoor channel model by matching its statistical properties to those of measured (real-world) channels. Finally, Section 7 draws the conclusion.

2. The Geometrical Indoor Scattering Model

This section briefly describes the geometrical scattering model, which was first proposed in [40] to characterize indoor propagation scenarios. Although a room has three dimensions, we only consider the 2D horizontal plane in which all local scatterers as well as the BS and the mobile station (MS) are located. As shown in Figure 1, the rectangle represents the 2D horizontal plane of a room. Its length and width are denoted by A and B , respectively. The BS is considered as the transmitter, leaving the MS to play the role as the receiver. For convenience, it is also assumed that the MS moves along the x -axis. Moreover, we consider single bounce scattering, which means that the plane waves emitted from the BS are only bounced once by scatterers before reaching the MS. The black star in Figure 1 represents a single local scatterer. In real-world environments, the number of scatterers is limited and their locations differ from one propagation scenario to another. To avoid studying the fading characteristics for a specific indoor propagation scenario characterized by a specific realization of a finite number of scatterers, we focus on a general statistical model that results from averaging over all possible propagation scenarios. Therefore, we assume that an infinite number of scatterers are randomly distributed inside the room. Such a model acts here as a nonrealizable stochastic reference model. From the reference channel model, an efficient channel simulator with low realization expenditure can be derived by making use of the SOC principle [45].

A straightforward assumption would be that the scatterers are uniformly distributed inside the room. For the modeling of indoor channels, however, it is more realistic to assume

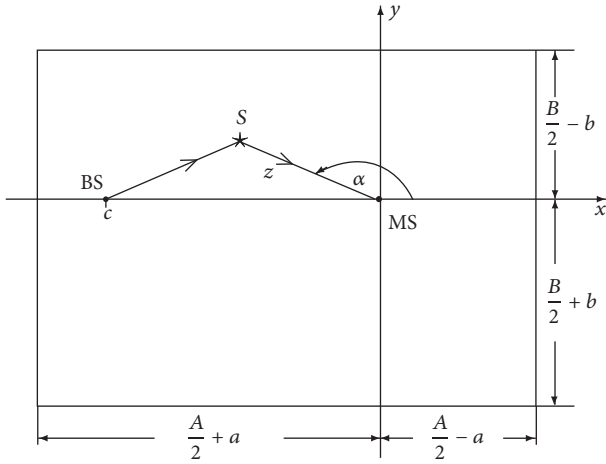


FIGURE 1: Geometrical indoor scattering model with local scatterers S , which are randomly distributed over the 2D horizontal plane of a room with length A and width B ($a \geq 0$ and $b \geq 0$).

that the probability of the occurrence of a scatterer decays exponentially with the distance from the walls. This implies that it is more likely that the received scattered components are coming from the walls rather than from objects located in the room's centre. Instead of the uniform distribution, we use therefore a mixture of exponential functions to model the distribution of the scatterers inside the 2D horizontal plane of the room. The exponential functions are more general and include the uniform distribution as a special case, as explained in the next section.

3. Statistical Characterization of the Reference Channel Model

This section studies the statistical properties of the proposed indoor wideband reference channel model. In this regard, the PDF of the AOA, the PDP, and the FCF are of special interest.

It is shown in Figure 1 that the BS is located at the position $(c, 0)$ ($c < 0$), while the MS is located at the origin of the coordinate system. The position of the local scatterer S is described by (x, y) , where x and y are independent random variables. As mentioned in Section 2, it is assumed that the scatterers are exponentially distributed within the 2D horizontal plane of the room. This implies that the random variables x and y must be exponentially distributed over the intervals $I_x = [-A/2 - a, A/2 - a]$ and $I_y = [-B/2 - b, B/2 - b]$, respectively. Thus, the PDF $p_x(x)$ of x and the PDF $p_y(y)$ of y are given by

$$p_x(x) = \begin{cases} P_1 [e^{-w_{11}(x+A/2+a)} + e^{w_{12}(x-A/2+a)}], & x \in I_x, \\ 0, & \text{otherwise,} \end{cases} \quad (1a)$$

$$p_y(y) = \begin{cases} P_2 [e^{-w_{21}(y+B/2+b)} + e^{w_{22}(y-B/2-b)}], & y \in I_y, \\ 0, & \text{otherwise,} \end{cases} \quad (1b)$$

where $w_{kl} \geq 0$ ($k, l = 1, 2$) are real-valued parameters and

$$P_1 = \frac{w_{11}w_{12}}{w_{12}(1 - e^{-w_{11}A}) + w_{11}(1 - e^{-w_{12}A})}, \quad (2a)$$

$$P_2 = \frac{w_{21}w_{22}}{w_{22}(1 - e^{-w_{21}B}) + w_{21}(1 - e^{-w_{22}B})}. \quad (2b)$$

It should be mentioned that the distributions in (1a) and (1b) include the uniform distribution as a special case if $w_{kl} \rightarrow 0$ for $k, l = 1, 2$. With the rule of de l'Hospital, it can be shown that in this case P_1 and P_2 tend to $P_1 = 1/(2A)$ and $P_2 = 1/(2B)$, respectively. Owing to the assumption that the random variables x and y are statistically independent, we can express the joint PDF $p_{xy}(x, y)$ of x and y as the product of the marginal PDFs $p_x(x)$ and $p_y(y)$; that is,

$$p_{xy}(x, y) = p_x(x) \cdot p_y(y). \quad (3)$$

Next, we describe the position of the scatterers by using polar coordinates (z, α) , where z denotes the path length from the position of the scatterer S to the MS, and α is the AOA (see Figure 1). Notice that z and α are random variables. The joint PDF $p_{z\alpha}(z, \alpha)$ of the position of the scatterers in polar coordinates (z, α) can be written by using (3) as

$$p_{z\alpha}(z, \alpha) = zp_{xy}(z \cos(\alpha), z \sin(\alpha)) \\ = zp_x(z \cos(\alpha)) \cdot p_y(z \sin(\alpha)). \quad (4)$$

Let D be the propagation path length, which is the plane wave's overall traveling distance from the BS via the scatterer S to the MS; then D is given by

$$D = z + \sqrt{z^2 - 2cz \cos(\alpha) + c^2}. \quad (5)$$

Our next focus is on finding the joint PDF of the path length D and the AOA α using (4). For this purpose, we introduce the auxiliary random variable $\theta = \alpha$. Solving the system of equations determined by $D = z + \sqrt{z^2 - 2cz \cos(\alpha) + c^2}$ and $\theta = \alpha$ gives us the following two solutions:

$$\alpha = \theta, \quad (6a)$$

$$z = \frac{D^2 - c^2}{2(D - c \cos \alpha)}. \quad (6b)$$

By applying the fundamental theorem of transformation of random variables [46, p. 201], the joint PDF $p_{D\theta}(D, \theta)$ of the path length D and the auxiliary random variable θ is given by

$$p_{D\theta}(D, \theta) = |J(D, \theta)| \cdot p_{z\alpha}\left(\frac{D^2 - c^2}{2(D - c \cos \theta)}, \theta\right), \quad (7)$$

where

$$J(D, \theta) = \begin{vmatrix} \frac{\partial \alpha}{\partial D} & \frac{\partial \alpha}{\partial \theta} \\ \frac{\partial z}{\partial D} & \frac{\partial z}{\partial \theta} \end{vmatrix} = -\frac{D^2 - 2Dc \cos \theta + c^2}{2(D - c \cos \theta)^2} \quad (8)$$

denotes the Jacobian determinant of the inverse transformation. Substituting (8) into (7) and using (4), (6a), and (6b), we find the expression for the joint PDF $p_{\mathbf{D}\theta}(D, \theta)$. Owing to $\theta = \alpha$, the joint PDF $p_{\mathbf{D}\alpha}(D, \alpha)$ can be expressed directly using the joint PDF $p_{\mathbf{D}\theta}(D, \theta)$ by replacing θ in (7) by α . Thus, we obtain

$$p_{\mathbf{D}\alpha}(D, \alpha) = \frac{[D^2 - 2Dc \cos(\alpha) + c^2](D^2 - c^2)}{4(D - c \cos(\alpha))^3} \cdot P_x \left(\frac{(D^2 - c^2) \cos(\alpha)}{2(D - c \cos(\alpha))} \right)$$

$$p_{\alpha}(\alpha) = \int_{D \in \mathbf{I}_{\mathbf{D}}} p_{\mathbf{D}\alpha}(D, \alpha) dD,$$

$$D_{\max}(\alpha) = \begin{cases} \frac{A_-}{2 \cos(\alpha)} + \sqrt{\left[\frac{A_-}{2 \cos(\alpha)} \right]^2 - cA_- + c^2}, & \text{if } -\arctan \frac{B_+}{A_-} < \alpha \leq \arctan \frac{B_-}{A_-}, \\ \frac{B_-}{2 \sin(\alpha)} + \sqrt{\left[\frac{B_-}{2 \sin(\alpha)} \right]^2 - cB_- \cot(\alpha) + c^2}, & \text{if } \arctan \frac{B_-}{A_-} < \alpha \leq \pi - \arctan \frac{B_-}{A_+}, \\ -\frac{A_+}{2 \cos(\alpha)} + \sqrt{\left[\frac{A_+}{2 \cos(\alpha)} \right]^2 + cA_+ + c^2}, & \text{if } \pi - \arctan \frac{B_-}{A_+} < \alpha \leq \pi, \quad -\pi < \alpha \leq -\pi + \arctan \frac{B_+}{A_+}, \\ -\frac{B_+}{2 \sin(\alpha)} + \sqrt{\left[\frac{B_+}{2 \sin(\alpha)} \right]^2 + cB_+ \cot(\alpha) + c^2}, & \text{if } -\pi + \arctan \frac{B_+}{A_+} < \alpha \leq -\arctan \frac{B_+}{A_-}, \end{cases}$$

where $\mathbf{I}_{\mathbf{D}}$ represents the interval $(D_{\min}, D_{\max}(\alpha))$ in which D_{\min} and $D_{\max}(\alpha)$ are the minimum and the maximum propagation path length, respectively. The minimum propagation path length D_{\min} follows from (5) for $z = 0$; that is, $D_{\min} = |c|$. Notice that the maximum propagation path length $D_{\max}(\alpha)$ depends on α . It is shown in Appendix A that $D_{\max}(\alpha)$ is given as in (11), where

$$A_{\pm} = A \pm 2a, \quad (12a)$$

$$B_{\pm} = B \pm 2b. \quad (12b)$$

$$\cdot P_y \left(\frac{(D^2 - c^2) \sin(\alpha)}{2(D - c \cos(\alpha))} \right), \quad (9)$$

where $p_x(\cdot)$ and $p_y(\cdot)$ are the densities given by (1a) and (1b), respectively.

3.1. The PDF of the AOA. In this subsection, we are concerned with the derivation of the PDF $p_{\alpha}(\alpha)$ of the AOA α . This PDF can be obtained from the joint PDF $p_{\mathbf{D}\alpha}(D, \alpha)$ in (9) by integrating over the range of D ; that is,

$$\begin{aligned} & \text{if } -\arctan \frac{B_+}{A_-} < \alpha \leq \arctan \frac{B_-}{A_-}, \\ & \text{if } \arctan \frac{B_-}{A_-} < \alpha \leq \pi - \arctan \frac{B_-}{A_+}, \\ & \text{if } \pi - \arctan \frac{B_-}{A_+} < \alpha \leq \pi, \quad -\pi < \alpha \leq -\pi + \arctan \frac{B_+}{A_+}, \\ & \text{if } -\pi + \arctan \frac{B_+}{A_+} < \alpha \leq -\arctan \frac{B_+}{A_-}, \end{aligned} \quad (11)$$

With $D_{\min} = |c|$ and $D_{\max}(\alpha)$, as given in (11), the PDF $p_{\alpha}(\alpha)$ can readily be obtained by solving the integral in (10) numerically.

3.2. The PDF of the Propagation Path Length. The PDF of the propagation path length \mathbf{D} , denoted by $p_{\mathbf{D}}(D)$, can be calculated by means of the relation

$$p_{\mathbf{D}}(D) = \int_{\alpha} p_{\mathbf{D}\alpha}(D, \alpha) d\alpha. \quad (13)$$

It is shown in Appendix B [see (B.9)] that the integral in (13) can be expressed by (14), which is presented as follows:

$$p_{\mathbf{D}}(D) = \begin{cases} g(-\pi, \pi), & \text{if } |c| \leq D \leq D_4, \\ g(-\pi, \alpha_1) + g_2(\alpha_2, \pi), & \text{if } D_4 < D \leq D_8, \\ g(-\pi, \alpha_3) + g_2(\alpha_4, \alpha_1) + g_2(\alpha_2, \pi), & \text{if } D_8 < D \leq D_1, \\ g(-\pi, \alpha_3) + g_2(\alpha_4, \alpha_5) + g_2(\alpha_6, \alpha_1) + g_2(\alpha_2, \pi), & \text{if } D_1 < D \leq D_2, \\ g(-\pi, \alpha_3) + g_2(\alpha_4, \alpha_5) + g_2(\alpha_2, \pi), & \text{if } D_2 < D \leq D_3, \\ g(-\pi, \alpha_3) + g_2(\alpha_2, \pi), & \text{if } D_3 < D \leq D_6, \\ g(\alpha_8, \alpha_3) + g_2(\alpha_2, \alpha_7), & \text{if } D_6 < D \leq D_5, \\ g(\alpha_8, \alpha_3), & \text{if } D_5 < D \leq D_7, \end{cases} \quad (14)$$

where the path lengths D_1, D_2, \dots, D_8 are given in Appendix B, and $g(\alpha_m, \alpha_n)$ denotes the integral

$$g(\alpha_m, \alpha_n) = \int_{\alpha_m}^{\alpha_n} p_{D\alpha}(D, \alpha) d\alpha, \quad (15)$$

in which

$$\alpha_{1,2} = 2 \arctan \left\{ \frac{D-c}{B_-} \mp \sqrt{\left(\frac{D-c}{B_-}\right)^2 - \frac{D-c}{D+c}} \right\}, \quad (16a)$$

$$\alpha_{3,4} = -2 \arctan \left\{ \frac{D-c}{B_+} \pm \sqrt{\left(\frac{D-c}{B_+}\right)^2 - \frac{D-c}{D+c}} \right\}, \quad (16b)$$

$$\alpha_{5,6} = \mp \arccos \left\{ \frac{DA_-}{D^2 - c^2 + cA_-} \right\}, \quad (16c)$$

$$\alpha_{7,8} = \pm \arccos \left\{ \frac{-DA_+}{D^2 - c^2 - cA_+} \right\}. \quad (16d)$$

3.3. The PDF and PDP of the Propagation Delays. The objective of this subsection is to find the PDF $p_{\tau'}(\tau')$ of the propagation delays τ' . Here, the propagation delay τ' is defined as

$$\tau' = \frac{D - |c|}{c_0}, \quad (17)$$

where c_0 denotes the speed of light. Taking this relation into account and applying the concept of transformation of random variables [46, p. 130], we can express the PDF $p_{\tau'}(\tau')$ of the propagation delays τ' as

$$p_{\tau'}(\tau') = c_0 p_D(c_0\tau' + |c|). \quad (18)$$

Here, $p_D(c_0\tau' + |c|)$ can be obtained directly from the PDF in (14) by replacing the variable D by the term $c_0\tau' + |c|$. For brevity, the expression for $p_D(c_0\tau' + |c|)$ is not presented here. Let the total power of the received multipath components be represented by $2\sigma_0^2$, and let us denote the PDP by $S_{\tau'}(\tau')$. Then, it follows that $\int_0^\infty S_{\tau'}(\tau') d\tau' = 2\sigma_0^2$ holds. By taking the relationship $S_{\tau'}(\tau') \sim p_{\tau'}(\tau')$ and the property $\int_0^\infty p_{\tau'}(\tau') d\tau' = 1$ into account, we can conclude that the following equation must hold for the PDP:

$$S_{\tau'}(\tau') = 2\sigma_0^2 p_{\tau'}(\tau') = 2c_0\sigma_0^2 p_D(c_0\tau' + |c|). \quad (19)$$

Hence, the PDP $S_{\tau'}(\tau')$ can be obtained directly from the PDF $p_D(D)$ in (14).

3.4. The FCF. According to the Wiener-Khinchin theorem, the PDP and the FCF form a Fourier transform pair. The FCF $r_{\tau'}(v')$ is defined as the Fourier transform of the PDP $S_{\tau'}(\tau')$; that is,

$$r_{\tau'}(v') = \int_0^\infty S_{\tau'}(\tau') e^{-j2\pi v' \tau'} d\tau'. \quad (20)$$

Substituting (19) in (20) results in the following expression for the FCF:

$$r_{\tau'}(v') = 2c_0\sigma_0^2 \int_0^\infty p_D(c_0\tau' + |c|) e^{-j2\pi v' \tau'} d\tau'. \quad (21)$$

Since no closed-form solution exists, the integral above has to be solved numerically.

4. Design of an SOC Wideband Indoor Channel Simulator

This section deals with the design of a stochastic SOC channel simulator for the proposed wideband indoor channel model. The time-variant impulse response of a wideband SOC channel simulator consisting of \mathcal{L} discrete propagation paths can be expressed as follows [47, Eq. (7.55)]:

$$\hat{\mathbf{h}}(\tau', t) = \sum_{\ell=0}^{\mathcal{L}-1} a_\ell \hat{\boldsymbol{\mu}}_\ell(t) \delta(\tau' - \tau'_\ell). \quad (22)$$

Here, the path gains a_ℓ are determined by the square root of the PDP assigned to the ℓ th discrete propagation delay. By applying the procedure described in [47, p. 374], we have

$$a_\ell = \sqrt{\int_{\tau' \in I_\ell} S_{\tau'}(\tau') d\tau'}, \quad \ell = 1, 2, \dots, \mathcal{L}, \quad (23)$$

where I_ℓ are the intervals defined in [47, p. 374]. The stochastic complex process $\hat{\boldsymbol{\mu}}_\ell(t)$ in (22) models the sum of all received scattered components having the same propagation delay τ'_ℓ . According to the SOC principle, such a stochastic process can be represented by a sum of N_ℓ cisoids of the form [45]

$$\hat{\boldsymbol{\mu}}_\ell(t) = \sum_{n=1}^{N_\ell} c_{n,\ell} e^{j(2\pi f_{n,\ell} t + \theta_{n,\ell})}. \quad (24)$$

Here, the quantities $c_{n,\ell}$, $f_{n,\ell}$, and $\theta_{n,\ell}$ represent the gain, the Doppler frequency, and the Doppler phase of the n th component of the ℓ th discrete path, respectively. The gains $c_{n,\ell}$ and the Doppler frequencies $f_{n,\ell}$ are constant. They can be determined by a proper parameter computation method, for example, the modified method of equal areas (MMEA) [48], according to which the gains $c_{n,\ell}$ are given by

$$c_{n,\ell} = \sigma_0 \sqrt{\frac{2}{N_\ell}}. \quad (25)$$

The Doppler frequencies $f_{n,\ell}$ are determined by the AOA $\alpha_{n,\ell}$ according to the well-known relation

$$f_{n,\ell} = f_{\max} \cos(\alpha_{n,\ell}), \quad (26)$$

where f_{\max} stands for the maximum Doppler frequency. The AOA $\alpha_{n,\ell}$ are constant parameters, which can be computed by means of the MMEA. This method requires solving the following equation:

$$\int_{-\pi}^{\alpha_{n,\ell}} p_{\alpha|\tau' \in I_\ell}(\alpha) d\alpha = \frac{1}{N_\ell} \left(n - \frac{1}{4} \right), \quad (27)$$

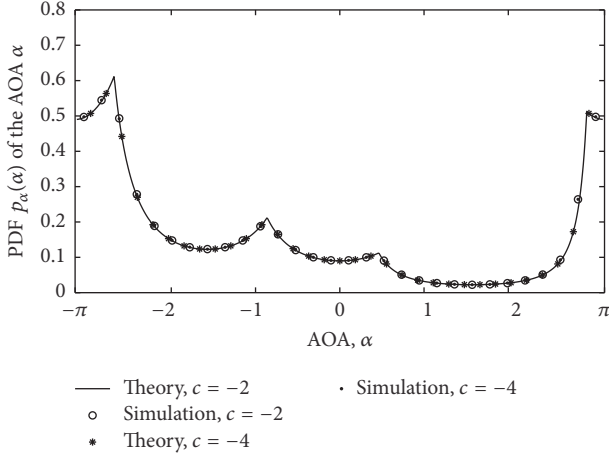


FIGURE 2: The PDF $p_\alpha(\alpha)$ of the AOA α for different locations of the BS.

for all $n = 1, 2, \dots, N_\ell$. The phases $\theta_{n,\ell}$ of the stochastic SOC channel simulator are independent and identically distributed (i.i.d.) random variables, each following a uniform distribution over $[0, 2\pi)$. Thus, the stochastic SOC channel simulator can be interpreted as a family of sample functions determined by the realizations of the phases $\theta_{n,\ell}$. A sample function can be obtained from the stochastic channel simulator by fixing all phases. Such a sample function, which can be interpreted as a waveform generated by a deterministic channel simulator, can be used to simulate the proposed wideband indoor channel.

5. Numerical and Simulation Results

This section illustrates the theoretical results given by (10) and (21). The correctness of the theoretical results will be verified by simulations. We will also show that the SOC channel simulator matches the reference channel model with respect to the FCF. The validity of the proposed indoor channel model is also confirmed by indoor channel measurements by studying the mean delay and the RMS delay spread. In all simulations, we consider a room with length $A = 10$ m and width $B = 5$ m as our indoor environment. The parameters a and b have been chosen to be equal to 2 and 1, respectively. The SOC channel simulator is designed by applying the MMEA [48] using $N_\ell = 8$ ($\ell = 1, 2, \dots, \mathcal{L}$) cisoids for each discrete propagation path.

The theoretical result of the PDF $p_\alpha(\alpha)$ of the AOA α [see (10)] of the wideband reference channel model is presented in Figure 2 for different BS locations ($c = -2$ and $c = -4$). It can be observed from this figure that the shape of the PDF of the AOA is independent of the position of the BS. The theoretical results illustrated in Figure 2 have been verified by experiments. In our experiments, we determined the horizontal (and vertical) locations of all scatterers in the Cartesian coordinate system as outcomes of a random generator, which generates uniformly distributed scatterers over $[-A/2 - a, A/2 - a]$ and $[-B/2 - b, B/2 - b]$ according to the distributions in (1a) and (1b), respectively. It should

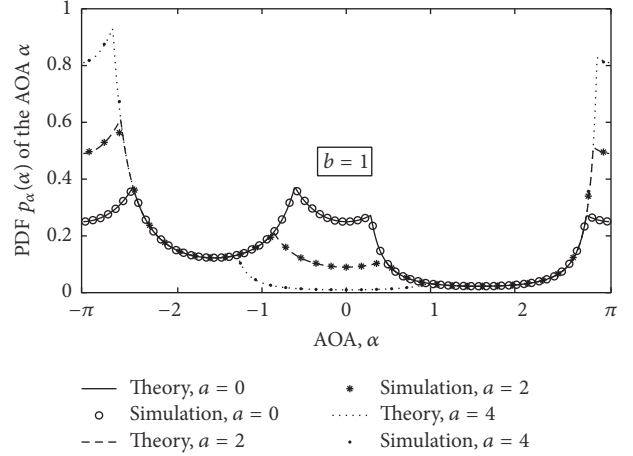


FIGURE 3: The PDF $p_\alpha(\alpha)$ of the AOA α for different locations of the MS.

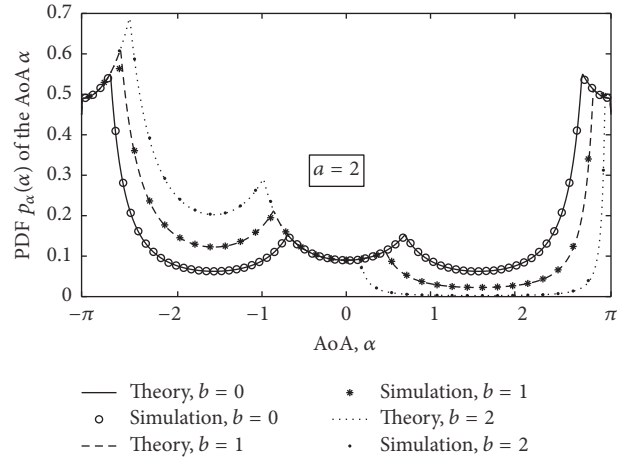


FIGURE 4: The PDF $p_\alpha(\alpha)$ of the AOA α for different locations of the MS.

be mentioned that the results in Figure 2 correspond to the PDF of the AOA of the narrowband channel model (see [39, Eq. (9)]). In Section 6, we will graphically present the PDF of the AOA in case that the locations of the scatterers are exponentially distributed. The impact of the parameters a and b on the shape of the PDF $p_\alpha(\alpha)$ of the AOA α is illustrated in Figures 3 and 4, respectively. It can be observed from Figure 3 that an increase in the value of a from 0 to 4 results in a decrease in the PDF $p_\alpha(\alpha)$ at small values of the AOAs, where they are confined to the interval $[-\arctan(B_+/A_-), \arctan(B_-/A_-)]$. In contrast, the PDF $p_\alpha(\alpha)$ increases with increasing values of a at large values of the AOA; that is, $\alpha \in [-\arctan(B_+/A_+), -\pi] \cup [\arctan(B_-/A_+), \pi]$.

Figure 4 reveals that an increase in b leads to an inverse effect on the shape of the PDF $p_\alpha(\alpha)$ compared to an increase in a . Figures 3 and 4 show that both the parameters a and b , which control the symmetry of the room, have impacts on the shape of the PDF of AOA. The main reason is that when a or b changes, it means the location of the mobile station relative to

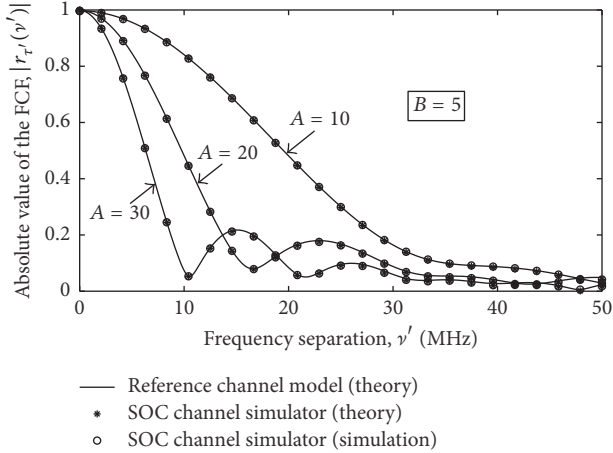


FIGURE 5: Absolute values of the FCFs $|r_{\tau'}(\nu')|$ (reference model) and $|\bar{r}_{\tau'}(\nu')|$ (simulation model) for different values of the room length A .

the room area moves (see the geometrical indoor scattering model in Figure 1). While a scatterer is fixed, the position of the mobile station determines the value of the AOA. If the mobile station moves closer to a wall, the AOA bounced by the scatterers in the triangle formed by the mobile station and two corners of the wall takes a larger range. Therefore, the PDF of one angle from that range decreases.

Figure 5 shows the absolute value of the FCF $r_{\tau'}(\nu')$ that has been calculated by using (21) for different values of the room length A . For comparison purposes, we also plot the theoretical curve for the absolute value of the FCF of the designed SOC simulation model by using Eq. (31) in [42]. We consider $\mathcal{L} = 20$ discrete propagation paths for the SOC channel simulator, where the corresponding delays τ'_ℓ are equally spaced between 0 and the maximum propagation delay τ'_{\max} . The value of τ'_{\max} can be obtained from (18) as the maximum value of τ' such that $p_{\tau'}(\tau') \neq 0$. The path powers assigned to different propagation paths have been calculated according to the method described in [47, pp. 374–375]. The AOAs of the SOC channel simulator are computed by employing the MMEA [48]. We observe from Figure 5 that the FCF of the SOC channel simulator can be brought into extremely good agreement with that of the reference model. The FCF decays faster with increasing the frequency separation ν' if the room length A increases (here from 10 m to 30 m). This means that the coherence bandwidth B_c becomes smaller as A increases (the coherence bandwidth B_c of a wideband mobile radio channel is the smallest positive value of the frequency separation variable $\nu' = B_c$ for which the condition $|r_{\tau'}(B_c)| = |r_{\tau'}(0)|/2$ is fulfilled).

The influence of the room width B on the FCF is presented in Figure 6 from which similar conclusions can be drawn as from Figure 5. When the dimensions of the room increase, the frequency correlation of time-variant transfer functions reduces at the same frequency separation. In other words, the time-variant transfer functions of the developed SOC channel simulator become independent at a smaller

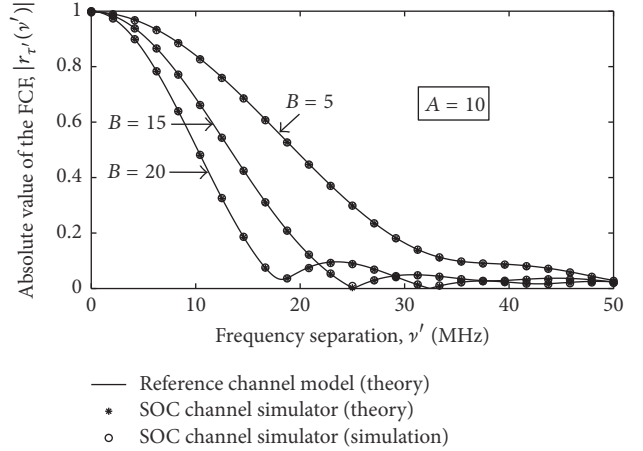


FIGURE 6: Absolute values of the FCFs $|r_{\tau'}(\nu')|$ (reference model) and $|\bar{r}_{\tau'}(\nu')|$ (simulation model) for different values of the room width B .

frequency separation, which leads to a smaller coherence bandwidth.

6. Experimental Verification

To demonstrate the usefulness of the proposed geometrical-based indoor reference channel model, we will show how the statistics of the reference channel model can be fitted to the statistics of measured real-world channels by optimizing the key parameters of the reference model. Here, two of the most important characteristic quantities of wideband mobile radio channels are considered, namely, the mean excess delay and the RMS delay spread.

The mean excess delay $m_{\tau'}$ is defined as the first moment of the PDP [26, 49]; that is,

$$m_{\tau'} = \frac{\int_0^{\infty} \tau' \cdot S_{\tau'}(\tau') d\tau'}{\int_0^{\infty} S_{\tau'}(\tau') d\tau'}. \quad (28)$$

The RMS delay spread $\sigma_{\tau'}$ is defined as the square root of the second central moment of the PDP [26, 49]; that is,

$$\sigma_{\tau'} = \sqrt{\frac{\int_0^{\infty} (\tau' - m_{\tau'})^2 \cdot S_{\tau'}(\tau') d\tau'}{\int_0^{\infty} S_{\tau'}(\tau') d\tau'}}. \quad (29)$$

The mean excess delay $m_{\tau'}$ and the RMS delay spread $\sigma_{\tau'}$ of the reference model can easily be calculated by substituting the PDP $S_{\tau'}(\tau')$ [see (19)] into (28) and (29), respectively.

The measurement results of the mean excess delay $m_{\tau'}^*$ and the RMS delay spread $\sigma_{\tau'}^*$ considered in this section are taken from [16, 19, 23]. The measurement campaigns were carried out in laboratories, a conference room, and corridors. The measurements in [16] have been obtained at 2.4 GHz in a laboratory with dimensions 7.8 m \times 9.95 m. Furthermore, the measurements reported in [19] have been obtained at 5 GHz in a conference room with dimensions 6.6 m \times 5.9 m. Finally, the measurements in [23] have been obtained at 60 GHz in

TABLE 1: Optimized parameters of the reference models for laboratory scenarios at 2.4 GHz based on the measurements in [16].

Locations	$m_{\tau'}^*$ (ns)	$\sigma_{\tau'}^*$ (ns)	$m_{\tau'}$ (ns)	$\sigma_{\tau'}$ (ns)	A	B	a	b	c	w_{11}	w_{12}	w_{21}	w_{22}
Loc. 1	57.04	30.55	57.04	30.49	7.8	9.95	3.51	4.32	-0.01	701.53	198.76	3.71	34.05
Loc. 2	43.40	24.12	43.40	24.12	7.8	9.95	3.48	3.93	-1.02	10.17	10.10	10.16	9.94
Loc. 3	49.10	22.19	49.10	22.12	7.8	9.95	3.76	3.59	-1.01	10.04	12.04	7.34	12.59
Loc. 4	54.85	26.82	54.85	26.82	7.8	9.95	3.87	4.97	-0.86	12.01	13.18	4.60	8.79

TABLE 2: Optimized parameters of the reference models for the conference room at 5 GHz based on the measurements in [19].

Locations	$m_{\tau'}^*$ (ns)	$\sigma_{\tau'}^*$ (ns)	$m_{\tau'}$ (ns)	$\sigma_{\tau'}$ (ns)	A	B	a	b	c	w_{11}	w_{12}	w_{21}	w_{22}
Loc. 1	20.5	18.6	20.5	18.6	6.6	5.9	2.99	2.78	-0.88	12.78	7.83	13.12	3.70
Loc. 2	16.4	16.2	16.4	16.2	6.6	5.9	2.84	2.09	-0.66	5.65	2.79	14.15	1.61
Loc. 3	19.7	17.8	19.7	17.8	6.6	5.9	3.03	2.62	-0.68	8.53	1.33	7.25	5.38
Loc. 4	21.8	18.5	21.8	18.5	6.6	5.9	3.01	2.62	-0.80	5.83	2.07	6.93	4.82
Loc. 5	18.0	16.6	18.0	16.6	6.6	5.9	3.21	2.29	-0.84	6.85	1.23	7.21	4.21
Loc. 6	17.2	15.5	17.2	15.5	6.6	5.9	2.87	2.11	-0.96	7.44	1.62	6.84	3.67
Loc. 7	17.9	16.4	17.9	16.4	6.6	5.9	3.10	2.29	-0.87	6.84	1.20	7.19	4.37
Loc. 8	14.3	15.9	14.3	15.9	6.6	5.9	3.17	2.28	-0.95	7.93	1.33	7.42	2.58
Loc. 9	19.0	20.2	19.0	20.2	6.6	5.9	3.00	2.90	-0.17	18.97	4.84	17.05	7.14
Loc. 10	20.8	20.7	20.8	20.7	6.6	5.9	3.00	2.90	-0.14	18.02	6.70	16.74	6.51
Loc. 11	23.6	20.4	23.6	20.4	6.6	5.9	2.89	2.90	-0.15	19.31	7.13	12.38	7.29
Loc. 12	24.0	19.9	24.0	19.9	6.6	5.9	2.78	2.90	-0.15	19.90	7.33	12.18	7.45

TABLE 3: Optimized parameters of the reference models for the corridor and laboratory (Lab) scenarios at 60 GHz based on the measurements in [23].

Locations	$m_{\tau'}^*$ (ns)	$\sigma_{\tau'}^*$ (ns)	$m_{\tau'}$ (ns)	$\sigma_{\tau'}$ (ns)	A	B	a	b	c	w_{11}	w_{12}	w_{21}	w_{22}
Loc. 1	5.17	13.70	5.17	13.70	30	1.75	13.26	0.45	-15.64	9.61	0.23	14.50	1.67
Loc. 2	8.18	15.04	8.18	15.04	30	1.75	13.66	0.53	-16.08	31.23	1.17	11.89	1.02
Loc. 3	3.84	12.35	3.84	12.35	30	1.75	14.62	0.57	-19.17	30.88	1.02	11.67	1.05
Loc. 4	5.37	12.34	5.37	12.34	30	1.75	14.01	0.44	-17.95	31.85	0.98	14.31	1.13
<i>Average corridor</i>	5.64	13.36	5.64	13.36	30	1.75	12.98	0.56	-15.61	10.38	0.16	21.75	1.01
Loc. 5	8.42	14.72	8.42	14.72	19.5	7.5	9.00	1.34	-7.53	9.87	0.40	11.05	0.45
Loc. 6	3.52	12.56	3.77	12.56	19.5	7.5	9.02	3.42	-5.65	5.04	0.71	232.37	2.96
<i>Average Lab (LOS)</i>	5.97	13.64	5.97	13.64	19.5	7.5	9.02	2.29	-5.62	4.36	0.82	185.74	1.38
Loc. 7	12.81	19.94	12.51	19.28	19.5	7.5	7.85	2.98	-7.13	3.22	0.22	20.71	2.29
Loc. 8	14.69	21.09	14.67	21.08	19.5	7.5	9.21	0.72	-8.21	1.93	0.21	0.01	0.68
<i>Average Lab (NLOS)</i>	13.75	20.52	13.72	20.51	19.5	7.5	9.00	1.72	-9.05	1.48	0.21	19.28	0.33
<i>Overall</i>	7.75	15.22	7.75	15.22	19.5	7.5	9.00	2.26	-3.97	1.24	0.63	30.97	0.74

two 30 m \times 1.75 m \times 2.80 m corridors as well as inside a laboratory with dimensions 19.5 m \times 7.5 m.

We combine all the relevant model parameters (except the parameters A and B) which control the mean excess delay $m_{\tau'}$ and the RMS delay spread $\sigma_{\tau'}$ of the reference channel model into a parameter vector denoted and defined by $\Omega := (a, b, c, w_{11}, w_{12}, w_{21}, w_{22})$. We also introduce the following error function:

$$E(\Omega) = W_1 \cdot |m_{\tau'}^* - m_{\tau'}| + W_2 \cdot |\sigma_{\tau'}^* - \sigma_{\tau'}|, \quad (30)$$

for measuring the deviations between the mean excess delays $m_{\tau'}^*$ and $m_{\tau'}$ as well as between the RMS delay spreads $\sigma_{\tau'}^*$ and $\sigma_{\tau'}$. In (30), W_1 and W_2 represent proper weighting factors.

The optimization of the parameter vector Ω has been carried out by minimizing numerically the above error

function $E(\Omega)$ by means of the quasi-Newton optimization procedure [50]. The optimization results are presented in Tables 1, 2, and 3, for the laboratory, the conference room, and corridor scenarios. For comparison purpose, the measured mean excess delay $m_{\tau'}^*$ and the measured RMS delay spread $\sigma_{\tau'}^*$, presented in [16, 19, 23], are also shown in Tables 1, 2, and 3. Note that the dimensions of the different rooms, which are controlled by the parameters A and B , have been chosen such that they are equal to the lengths and widths of the rooms in which the corresponding measurement campaigns have been conducted. Hence, A and B are fixed, and thus they have not been included in the optimization procedure. In Table 1, the measured mean excess delay $m_{\tau'}^*$ is in the range from 43.40 ns to 57.04 ns, while the RMS delay spread $\sigma_{\tau'}^*$ varies from 22.19 ns to 30.55 ns. Similarly, in Table 2, the

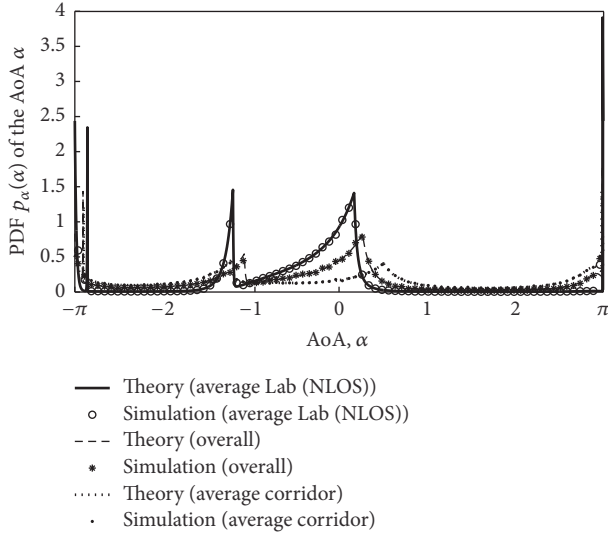


FIGURE 7: The PDF $p_\alpha(\alpha)$ of the AOA α for three different indoor propagation scenarios.

measured mean assess delay m_r^* , is in the range from 16.40 ns to 24.0 ns, while the RMS delay spread σ_r^* , varies from 15.5 ns to 20.7 ns. In Table 3, finally, the measured mean assess delay m_r^* , covers the range from 3.84 ns to 8.18 ns and holds for hallways, while the range from 3.52 ns to 14.69 ns refers to offices. In addition, the measured RMS delay spread σ_r^* , varies from 12.34 ns to 15.04 ns for corridors and from 12.56 ns to 21.09 ns for laboratories. In our optimization procedure, the weighting factors W_1 and W_2 were chosen to be 0.35 and 0.65, respectively. For reasons of brevity, we have only presented the values of the optimized parameters in all tables with two decimals of precision. As shown in Tables 1, 2, and 3, the mean excess delay m_r and the RMS delay spread σ_r of the proposed wideband indoor channel model are very close to the corresponding measured quantities for all considered indoor propagation scenarios, which demonstrates that the reference channel model is useful for characterizing real-world wideband indoor mobile radio channels.

For completeness, we present in Figure 7 the nonuniform PDF $p_\alpha(\alpha)$ of the AOA α for three of the indoor propagation scenarios, namely, the Average Corridor, the Average Lab (NLOS), and the overall channel scenario. In this figure, we see that the PDF of the AOA has 4 peaks corresponding to the characteristics of the exponential distribution within the 2D horizontal plan of the room. The results in this figure have been obtained by evaluating (10) with the optimized channel parameters listed in Table 1.

7. Conclusion

In this paper, we have developed a wideband mobile radio channel model for indoor propagation environments. The starting point for the derivation of the reference channel model was a geometrical scattering model, where we have assumed that an infinite number of scatterers are exponentially distributed within the 2D horizontal plane of a

rectangular room. Analytical expressions have been derived for the PDF of the AOA, the PDF of the propagation delays, the PDP, and the FCF. We have shown that the shape of the PDF of the AOA is independent of the position of the transmitter (BS). Both the room length and width have a strong influence on the PDF of the AOA and the FCF. If the room length or width increases, the FCF decays faster if the frequency separation increases. The coherence bandwidth decreases with increasing the room size. The usefulness of the proposed reference channel model has been demonstrated by a close match between the channel statistics of the reference model and measured channels.

An efficient channel simulator has been derived from the reference channel model by applying the SOC principle. It has been shown that the SOC channel simulator matches closely the wideband reference model with respect to the FCF. The designed SOC channel simulator can be used for the performance evaluation of wideband indoor wireless communication systems under realistic propagation conditions.

Appendix

A. Derivation of the Maximum Propagation Path Length for a Given Value of the AOA

The function $D(z, \alpha)$, defined by

$$D(z, \alpha) = z + \sqrt{z^2 - 2cz \cos \alpha + c^2}, \quad (\text{A.1})$$

describes the propagation path length from the BS to the MS via a single scatterer S located at an arbitrary place of the 2D horizontal plane of the room. Owing to the fact that the derivative of $D(z, \alpha)$ with respect to z is always positive, that is,

$$\frac{d}{dz} D(z, \alpha) = 1 + \frac{z - c \cos \alpha}{\sqrt{z^2 - 2cz \cos \alpha + c^2}} \geq 0, \quad (\text{A.2})$$

we may conclude that $D(z, \alpha)$ is a monotonic increasing function with respect to z . That means, for a given value of the AOA α , the propagation path length $D(z, \alpha)$ takes a maximum value if the distance z from the MS to the scatterer S is maximum. The maximum of z , denoted by z_{\max} , always occurs if a scatterer is located at the boundary of the rectangle.

For the derivation of the maximum propagation path length, we partition the scattering region inside the room into four subregions R_1, R_2, \dots, R_4 , as illustrated in Figure 8. In the Subregion R_1 , the AOA α is confined to the interval, $(-\arctan(B_+/A_-), \arctan(B_-/A_-)]$.

According to the geometrical relationship in Figure 8, we have

$$z_{\max} = \frac{A_-}{2 \cos(\alpha)}. \quad (\text{A.3})$$

Substituting (A.3) into (A.1) gives an analytical expression for the maximum propagation path length $D_{\max}(\alpha)$:

$$D_{\max}(\alpha) = D(z_{\max}, \alpha) = \frac{A_-}{2 \cos(\alpha)} + \sqrt{\left[\frac{A_-}{2 \cos(\alpha)}\right]^2 - cA_- + c^2}, \quad (\text{A.4})$$

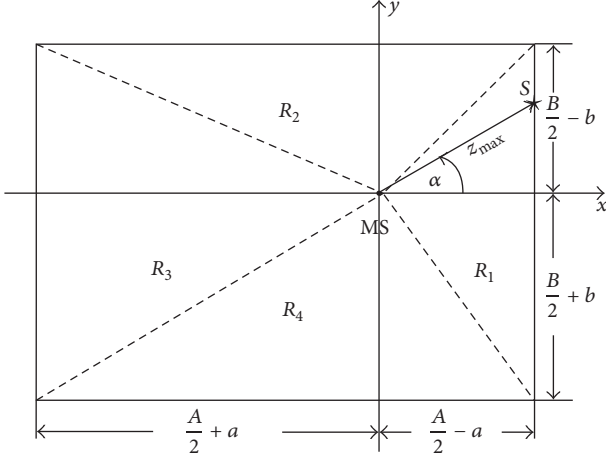


FIGURE 8: Partitioning of the scattering region inside a rectangular room into four subregions: R_1 , R_2 , R_3 , and R_4 , separated by dashed lines (---).

which depends only on the AOA α . The maximum propagation path length $D_{\max}(\alpha)$ for the other subregions R_2 , R_3 , and R_4 can be computed analogously. For brevity, we only present the final expression for $D_{\max}(\alpha)$ in (11).

B. Determination of the Values for D_i and α_i in (14)

In this appendix, we first determine the maximum value and the minimum value of D_{\max} for the four scattering subregions illustrated in Figure 8.

Subregion R_1 . $-\arctan(B_+/A_-) < \alpha \leq \arctan(B_-/A_-)$. It can easily be seen from (A.4) that $D_{\max}(\alpha)$ is a monotonic increasing function with respect to α within the range $[0, \arctan(B_-/A_-)]$. We find that $D_{\max}(\alpha)$ takes the minimum value D_1 if $\alpha = 0$, whereas $D_{\max}(\alpha)$ equals the maximum value D_2 if $\alpha = \arctan(B_-/A_-)$; that is,

$$D_1 = \min(D_{\max}(\alpha)) = D_{\max}(\alpha)|_{\alpha=0} = A_- - c, \quad (\text{B.1a})$$

$$D_2 = \max(D_{\max}(\alpha)) = D_{\max}(\alpha)|_{\alpha=\arctan(B_-/A_-)} \\ = \frac{\sqrt{A_-^2 + B_-^2} + \sqrt{(A_- - 2c)^2 + B_-^2}}{2}. \quad (\text{B.1b})$$

If $\alpha \in (-\arctan(B_+/A_-), 0)$, then $D_{\max}(\alpha)$ decreases if α increases. Thus, the maximum $D_{\max}(\alpha)$ over this range is given by

$$D_3 = \max(D_{\max}(\alpha)) = D_{\max}(\alpha)|_{\alpha=-\arctan(B_+/A_-)} \\ = \frac{\sqrt{A_-^2 + B_+^2} + \sqrt{(A_- - 2c)^2 + B_+^2}}{2}. \quad (\text{B.2})$$

Subregion R_2 . $\arctan(B_-/A_-) < \alpha \leq \pi - \arctan(B_-/A_+)$. If a given value of the AOA α belongs to the range

$(\arctan(B_-/A_-), \pi - \arctan(B_-/A_+))$, then we obtain the fixed point $\alpha = \pi + \arctan(B_-/c)$ by setting the first derivative of $D_{\max}(\alpha)$ [see the second part of the piecewise function in (11)] with respect to α to zero. Since the second derivative of $D_{\max}(\alpha)$ with respect to α is positive, it follows that $D_{\max}(\alpha)$ has a minimum value D_4 at the fixed AOA $\alpha = \pi + \arctan(B_-/c)$; that is,

$$D_4 = \min(D_{\max}(\alpha)) = D_{\max}(\alpha)|_{\alpha=\pi+\arctan(B_-/c)} \\ = \sqrt{B_-^2 + c^2}. \quad (\text{B.3})$$

We notice that $D_{\max}(\alpha)$ is a monotonic increasing function if $\alpha \in (\pi + \arctan(B_-/c), \pi - \arctan(B_-/A_+))$. Therefore, $D_{\max}(\alpha)$ takes a maximum value D_5 at $\alpha = \pi - \arctan(B_-/A_+)$; that is,

$$D_5 = \max(D_{\max}(\alpha)) = D_{\max}(\alpha)|_{\alpha=\pi-\arctan(B_-/A_+)} \\ = \frac{\sqrt{A_+^2 + B_-^2} + \sqrt{(A_+ + 2c)^2 + B_-^2}}{2}. \quad (\text{B.4})$$

If $\alpha \in (\arctan(B_-/A_-), \pi + \arctan(B_-/c))$, then $D_{\max}(\alpha)$ decreases if α increases. Thus, we have $D_{\max}(\alpha) < D_2$.

Subregion R_3 . $\alpha \in (\pi - \arctan(B_-/A_+), \pi] \cup (-\pi, -\pi + \arctan(B_+/A_+))$. By studying the first and second derivatives of $D_{\max}(\alpha)$ [see the third part of the piecewise function in (11)], it can be shown that $D_{\max}(\alpha)$ is a monotonic decreasing function within $(\pi - \arctan(B_-/A_+), \pi]$. Thus, we have $D_6 \leq D_{\max}(\alpha) < D_5$, where

$$D_6 = \min(D_{\max}(\alpha)) = D_{\max}(\alpha)|_{\alpha=\pi} = A_+ + c. \quad (\text{B.5})$$

If $\alpha \in (-\pi, -\pi + \arctan(B_+/A_+))$, then $D_6 < D_{\max}(\alpha) \leq D_7$, where

$$D_7 = \max(D_{\max}(\alpha)) = D_{\max}(\alpha)|_{\alpha=-\pi+\arctan(B_+/A_+)} \\ = \frac{\sqrt{A_+^2 + B_+^2} + \sqrt{(A_+ + 2c)^2 + B_+^2}}{2}. \quad (\text{B.6})$$

Subregion R_4 . $-\pi + \arctan(B_+/A_+) < \alpha \leq -\arctan(B_+/A_-)$. By conducting similar calculations as for the Subregion R_2 , we obtain the range of $D_{\max}(\alpha)$ for the remaining interval of the AOA $\alpha \in (-\pi + \arctan(B_+/A_+), -\arctan(B_+/A_-))$. For brevity, we present only the final results here. The function $D_{\max}(\alpha)$ has a minimum value at the fixed AOA $\alpha = -\pi - \arctan(B_+/c)$; that is,

$$D_8 = \min(D_{\max}(\alpha)) = D_{\max}(\alpha)|_{\alpha=-\pi-\arctan(B_+/c)} \\ = \sqrt{B_+^2 + c^2}. \quad (\text{B.7})$$

The value of $D_{\max}(\alpha)$ decreases if the AOA changes from $-\pi + \arctan(B_+/A_+)$ to the fixed AOA given above. Within this range, we have $D_8 \leq D_{\max}(\alpha) < D_7$. If $\alpha \in (-\pi - \arctan(B_+/c), -\arctan(B_+/A_-))$, then $D_{\max}(\alpha)$ increases and the maximum value occurs at $\alpha = -\arctan(B_+/A_-)$, and thus we have $D_8 < D_{\max}(\alpha) \leq D_3$.

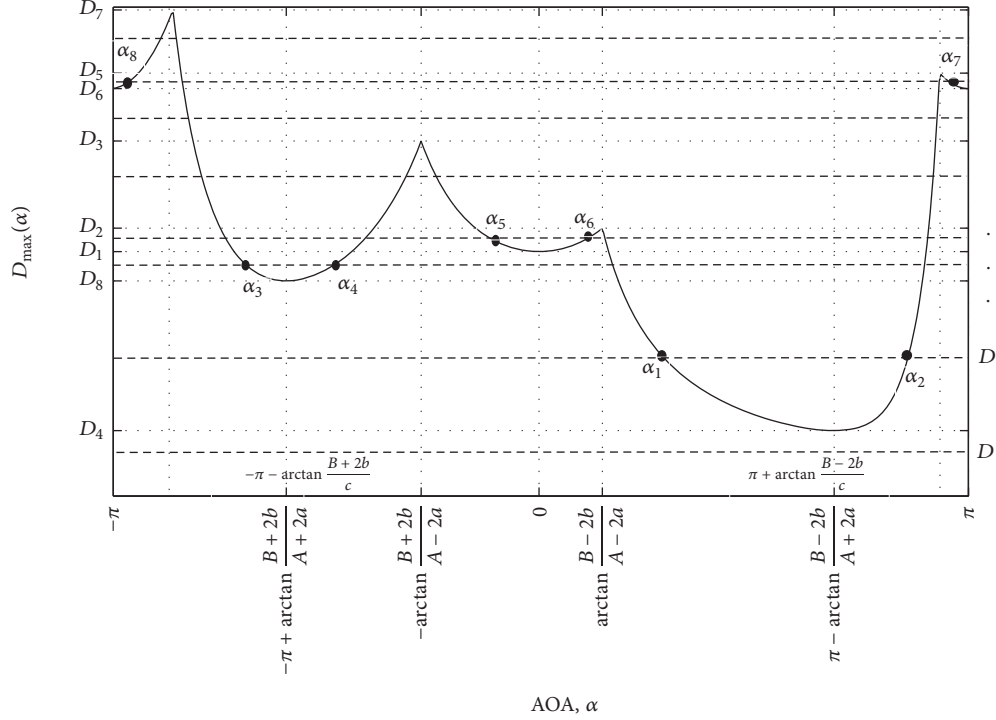


FIGURE 9: The maximum propagation path length $D_{\max}(\alpha)$ for different values of the AOA α ($A = 10$ m, $B = 5$ m, $a = 2$ m, $b = 1$ m, and $c = -2$ m).

An example for the maximum path length $D_{\max}(\alpha)$ is illustrated in Figure 9. It should be mentioned that the path length D is always less than or equal to $D_{\max}(\alpha)$. Since D_4 is the minimum value of $D_{\max}(\alpha)$ [see Figure 9], for a given value of the path length $D \leq D_4$, we can conclude that all AOAs $\alpha \in (-\pi, \pi]$ satisfy the inequality $D \leq D_{\max}(\alpha) \leq D_4$. However, if the path length $D_4 < D \leq D_8$, then the inequality $D \leq D_{\max}(\alpha)$ can only be guaranteed if $\alpha \in (-\pi, \alpha_1]$ or $\alpha \in [\alpha_2, \pi]$. Here, the AOAs α_1 and α_2 can be obtained by solving the equation

$$D_{\max}(\alpha) = D. \quad (\text{B.8})$$

As shown in Figure 9, $\alpha_1, \alpha_2 \in (\arctan(B_-/A_-), \pi - \arctan(B_-/A_+)]$. Thus, we select the second piece of $D_{\max}(\alpha)$ in (11) as the expression for the left-hand side of (B.8). Solving (B.8) results finally in the expressions for α_1 and α_2 as presented in (16a).

For the other given values of D , it is necessary to meet the condition $D \leq D_{\max}(\alpha)$. According to Figure 9, we obtained the relations in (B.9), which are presented as follows:

- (1) $\alpha \in (-\pi, \alpha_3] \cup [\alpha_4, \alpha_1] \cup [\alpha_2, \pi]$
if $D_8 < D \leq D_1$,
- (2) $\alpha \in (-\pi, \alpha_3] \cup [\alpha_4, \alpha_5] \cup [\alpha_6, \alpha_1] \cup [\alpha_2, \pi]$
if $D_1 < D \leq D_2$,
- (3) $\alpha \in (-\pi, \alpha_3] \cup [\alpha_4, \alpha_5] \cup [\alpha_2, \pi]$
if $D_2 < D \leq D_3$,

$$(4) \quad \alpha \in (-\pi, \alpha_3] \cup [\alpha_2, \pi] \quad \text{if } D_3 < D \leq D_6,$$

$$(5) \quad \alpha \in [\alpha_8, \alpha_3] \cup [\alpha_2, \alpha_7] \quad \text{if } D_6 < D \leq D_5,$$

$$(6) \quad \alpha \in [\alpha_8, \alpha_3] \quad \text{if } D_5 < D \leq D_7.$$

(B.9)

The AOAs α_i ($i = 3, 4, \dots, 8$) can be determined similarly by solving (B.8). The expression for $D_{\max}(\alpha)$ on the left-hand side of (B.8) is chosen in accordance with the range of α_i . For example, as $\alpha_3 \in (-\pi + \arctan(B_+/A_+), -\arctan(B_+/A_-)]$, the fourth part of $D_{\max}(\alpha)$ [see (11)] corresponding to the Subregion R_4 is selected.

Disclosure

This paper is an extended version of “Modeling and Statistical Characterization of Wideband Indoor Radio Propagation Channels,” which was published in the proceedings of the International Congress on Ultra Modern Telecommunications and Control Systems and Workshops (ICUMT), 2010. The starting point in this submitted paper is new. A mixture of exponential functions is used to model the distribution of scatterers. The new mixture exponential functions are more general and include the uniform distribution considered in the ICUMT paper as a special case. This influences all key results of the paper. In addition, the authors in this paper validate the developed channel model with experimental data. The paper shows, by optimizing some of the key parameters with proper methods, that it is possible to use

the geometrical channel mode to represent different realistic propagation scenarios.

Conflicts of Interest

The authors declare that there are no conflicts of interest regarding the publication of this paper.

Acknowledgments

This work was supported in part by the Key Scientific Research Team Cultivation Project founded by College of Information Science and Engineering, Shandong Agricultural University, China. Also, this work was supported in part by the Spanish Ministry of Economy and Competitiveness through the RACHEL Project (TEC2013-47141-C4-2-R), the CARMEN Project (TEC2016-75067-C4-3-R), and the COMONSENS network (TEC2015-69648-REDC).

References

- [1] J. E. Padgett, C. G. Gunther, and T. Hattori, "Overview of wireless personal communications," *IEEE Communications Magazine*, vol. 33, no. 1, pp. 28–41, 1995.
- [2] J. Karaoğuz, "High-rate wireless personal area networks," *IEEE Communications Magazine*, vol. 39, no. 12, pp. 96–102, 2001.
- [3] A. F. Molisch, *Wireless Communications*, John Wiley & Sons, Chichester, England, 2005.
- [4] P. Ferré, A. Doufexi, J. Chung-How, A. R. Nix, and D. R. Bull, "Robust video transmission over wireless LANs," *IEEE Transactions on Vehicular Technology*, vol. 57, no. 4, pp. 2596–2602, 2008.
- [5] P. Lin and Y.-B. Lin, "Implementation and performance evaluation for mobility management of a wireless PBX network," *IEEE Journal on Selected Areas in Communications*, vol. 19, no. 6, pp. 1138–1146, 2001.
- [6] H. Elgala, R. Mesleh, and H. Haas, "Indoor optical wireless communication: Potential and state-of-the-art," *IEEE Communications Magazine*, vol. 49, no. 9, pp. 56–62, 2011.
- [7] K. Wang, A. Nirmalathas, C. Lim, and E. Skafidas, "High-speed optical wireless communication system for indoor applications," *IEEE Photonics Technology Letters*, vol. 23, no. 8, pp. 519–521, 2011.
- [8] T. Ohtsuki, "Multiple-subcarrier modulation in optical wireless communications," *IEEE Communications Magazine*, vol. 41, no. 3, pp. 74–79, 2003.
- [9] H. Elgala, R. Mesleh, and H. Haas, "Indoor broadcasting via white LEDs and OFDM," *IEEE Transactions on Consumer Electronics*, vol. 55, no. 3, pp. 1127–1134, 2009.
- [10] J. B. Carruthers, S. M. Carroll, and P. Kannan, "Propagation modelling for indoor optical wireless communications using fast multi-receiver channel estimation," *IEEE Proceedings—Optoelectronics*, vol. 150, no. 5, pp. 473–481, 2003.
- [11] J. Kunthong and C. F. Bunting, "Statistical characterization of the 900 MHz and 1800 MHz indoor propagation using reverberation source stirring technique," in *Proceedings of the 2009 IEEE International Symposium on Antennas and Propagation and USNC/URSI National Radio Science Meeting, APSURSI 2009*, Charleston, SC, USA, June 2009.
- [12] E. Banner and A. B. Sesay, "Effects of antenna height, antenna gain, and pattern downtilting for cellular mobile radio," *IEEE Transactions on Vehicular Technology*, vol. 45, no. 2, pp. 217–224, 1996.
- [13] S. Y. Seidel and T. S. Rappaport, "914 MHz path loss prediction models for indoor wireless communications in multifloored buildings," *IEEE Transactions on Antennas and Propagation*, vol. 40, no. 2, pp. 207–217, 1992.
- [14] A. A. Saleh and R. A. Valenzuela, "A statistical model for indoor multipath propagation," *IEEE Journal on Selected Areas in Communications*, vol. 5, no. 2, pp. 128–137, 1987.
- [15] J. A. Wepman, J. R. Hoffman, and L. H. Loew, "Analysis of impulse response measurements for PCS channel modelling applications," *IEEE Transactions on Vehicular Technology*, vol. 44, no. 3, pp. 613–620, 1995.
- [16] T. A. Wysocki and H.-J. Zepernick, "Characterization of the indoor radio propagation channel at 2.4 GHz," *Journal of Telecommunications and Information Technology*, vol. 3–4, 2000.
- [17] D. A. Hawbaker and T. S. Rappaport, "Indoor wideband radiowave propagation measurements at 1.3 GHz and 4.0 GHz," *IEEE Electronics Letters*, vol. 26, no. 21, pp. 1800–1802, 1990.
- [18] G. Santella and E. Restuccia, "Analysis of frequency domain wide-band measurements of the indoor radio channel at 1, 5.5, 10 and 18 GHz," in *Proceedings of the GLOBECOM '96*, pp. 1162–1166, London, UK.
- [19] M. Peter and W. Keusgen, "Analysis and comparison of indoor wideband radio channels at 5 and 60 GHz," in *Proceedings of the 3rd European Conference on Antennas and Propagation, (EuCAP '09)*, pp. 3830–3834, Berlin, Germany, 2009.
- [20] H. Droste and G. Kadel, "Measurement and analysis of wide band indoor propagation characteristics at 17 GHz and 60 GHz," in *Proceedings of the 9th International Conference on Antennas and Propagation*, vol. 2, pp. 288–291, Eindhoven, Netherlands, April 1995.
- [21] W. Fu, J. Hu, and S. Zhang, "Frequency-domain measurement of 60 GHz indoor channels: a measurement setup, literature data, and analysis," *IEEE Instrumentation & Measurement Magazine*, vol. 16, no. 2, pp. 34–40, 2013.
- [22] N. Moraitis and P. Constantinou, "Indoor channel measurements and characterization at 60 GHz for wireless local area network applications," *IEEE Transactions on Antennas and Propagation*, vol. 52, no. 12, pp. 3180–3189, 2004.
- [23] N. Moraitis and P. Constantinou, "Measurements and characterization of wideband indoor radio channel at 60 GHz," *IEEE Transactions on Wireless Communications*, vol. 5, no. 4, pp. 880–889, 2006.
- [24] T. Zwick, T. J. Beukema, and H. Nam, "Wideband channel sounder with measurements and model for the 60 GHz indoor radio channel," *IEEE Transactions on Vehicular Technology*, vol. 54, no. 4, pp. 1266–1277, 2005.
- [25] H. Hashemi, "Impulse response modeling of indoor radio propagation channels," *IEEE Journal on Selected Areas in Communications*, vol. 11, no. 7, pp. 967–978, 1993.
- [26] D. Tholl and H. Hashemi, "Statistical modeling and simulation of the RMS delay spread of indoor radio propagation channels," *IEEE Transactions on Vehicular Technology*, vol. 43, no. 1, pp. 110–120, 1994.
- [27] K. Yu, M. Bengtsson, B. Ottersten, D. McNamara, P. Karlsson, and M. Beach, "Modeling of wide-band MIMO radio channels based on NLoS indoor measurements," *IEEE Transactions on Vehicular Technology*, vol. 53, no. 3, pp. 655–665, 2004.

- [28] S. Chamaani, S. A. Mirtaheri, Y. I. Nechayev, and P. S. Hall, "MICS band indoor channel modeling using ray tracing method," in *Proceedings of the 5th International Symposium on Telecommunications, (IST '10)*, pp. 126–131, Kish Island, Iran, December 2010.
- [29] S. Loredó, A. Rodríguez-Alonso, and R. P. Torres, "Indoor MIMO channel modeling by rigorous GO/UTD-based ray tracing," *IEEE Transactions on Vehicular Technology*, vol. 57, no. 2, pp. 680–692, 2008.
- [30] S.-H. Cheu and S.-K. Jeng, "All SBR/image approach to indoor radio propagation modeling," in *Proceedings of the IEEE Antennas and Propagation Society, AP-S international symposium (Digest)*, pp. 1952–1955, Newport Beach, Calif, USA, June 1995.
- [31] M. C. Lawton and J. P. McGeehan, "The application of a deterministic Ray launching algorithm for the prediction of radio channel characteristics in small-cell environments," *IEEE Transactions on Vehicular Technology*, vol. 43, no. 4, pp. 955–969, 1994.
- [32] Z. Ji, B.-H. Li, H.-X. Wang, H.-Y. Chen, and T. K. Sarkar, "Efficient ray-tracing methods for propagation prediction for indoor wireless communications," *IEEE Antennas and Propagation Magazine*, vol. 43, no. 2, pp. 41–49, 2001.
- [33] A. Ö. Kaya, L. J. Greenstein, and W. Trappe, "Characterizing indoor wireless channels via ray tracing combined with stochastic modeling," *IEEE Transactions on Wireless Communications*, vol. 8, no. 8, pp. 4165–4175, 2009.
- [34] G. Tiberi, S. Bertini, W. Q. Malik, A. Monorchio, D. J. Edwards, and G. Manara, "Analysis of realistic ultrawideband indoor communication channels by using an efficient ray-tracing based method," *IEEE Transactions on Antennas and Propagation*, vol. 57, no. 3, pp. 777–785, 2009.
- [35] G. E. Athanasiadou, A. R. Nix, and J. P. McGeehan, "Microcellular ray-tracing propagation model and evaluation of its narrow-band and wide-band predictions," *IEEE Journal on Selected Areas in Communications*, vol. 18, no. 3, pp. 322–335, 2000.
- [36] G. Liang and H. L. Bertoni, "A new approach to 3-D ray tracing for propagation prediction in cities," *IEEE Transactions on Antennas and Propagation*, vol. 46, no. 6, pp. 853–863, 1998.
- [37] T. Rautiainen, G. Wolfle, and R. Hoppe, "Verifying path loss and delay spread predictions of a 3D ray tracing propagation model in urban environment," in *Proceedings of the IEEE 56th Vehicular Technology Conference*, pp. 2470–2474, Vancouver, Canada, 2002.
- [38] L. Jiang and S. Y. Tan, "Geometrically based statistical channel models for outdoor and indoor propagation environments," *IEEE Transactions on Vehicular Technology*, vol. 56, no. 6, pp. 3587–3593, 2007.
- [39] Y. Ma and M. Patzold, "Design and simulation of narrowband indoor radio propagation channels under LOS and NLOS propagation conditions," in *Proceedings of the IEEE 71st Vehicular Technology Conference*, pp. 1–7, Taipei, Taiwan, May 2010.
- [40] Y. Ma and M. Pätzold, "Modeling and statistical characterization of wideband indoor radio propagation channels," in *Proceedings of the 2010 International Congress on Ultra Modern Telecommunications and Control Systems and Workshops, ICUMT 2010*, pp. 777–783, Moscow, Russia, October 2010.
- [41] Y. Ma, *Broadband wireless communication systems: Channel modeling and system performance analysis*[Ph.D. thesis], Dept. of Inform. and Commun. Technol., University of Agder, Grimstad, Norway, 2011, <https://brage.bibsys.no/xmlui/handle/11250/137621>.
- [42] M. Pätzold and B. O. Hogstad, "A wideband space-time MIMO channel simulator based on the geometrical one-ring model," in *Proceedings of the 2006 IEEE 64th Vehicular Technology Conference, VTC-2006 Fall*, pp. 133–138, Montreal, Canada, September 2006.
- [43] M. Pätzold and B. O. Hogstad, "A wideband MIMO channel model derived from the geometric elliptical scattering model," in *Proceedings of the 3rd International Symposium on Wireless Communication Systems 2006, ISWCS '06*, pp. 138–143, Valencia, Spain, September 2006.
- [44] Y. Ma and M. Pätzold, "Wideband two-ring MIMO channel models for mobile-to-mobile communications," in *Proceedings of the 10th International Symposium on Wireless Personal Multimedia Communications, WPMC 2007*, pp. 380–384, Jaipur, India, 2007.
- [45] M. Pätzold and B. Talha, "On the statistical properties of sum-of-cisoids-based mobile radio channel simulators," in *Proceedings of the 10th International Symposium on Wireless Personal Multimedia Communications, WPMC 2007*, pp. 394–400, Jaipur, India, 2007.
- [46] A. Papoulis and S. U. Pillai, *Probability, Random Variables, and Stochastic Processes*, McGraw-Hill, New York, NY, USA, 4th edition, 2002.
- [47] M. Pätzold, *Mobile Radio Channels*, John Wiley & Sons, Chichester, UK, 2nd edition, 2011.
- [48] C. A. Gutierrez-Diaz-De-Leon and M. Pätzold, "Sum-of-sinusoids-based simulation of flat fading wireless propagation channels under non-isotropic scattering conditions," in *Proceedings of the 50th Annual IEEE Global Telecommunications Conference, GLOBECOM 2007*, pp. 3842–3846, Washington, Wash, USA, November 2007.
- [49] H. Xu, V. Kukshya, and T. S. Rappaport, "Spatial and temporal characteristics of 60-GHZ indoor channels," *IEEE Journal on Selected Areas in Communications*, vol. 20, no. 3, pp. 620–630, 2002.
- [50] R. Fletcher and M. J. D. Powell, "A rapidly convergent descent method for minimization," *The Computer Journal*, vol. 6, no. 2, pp. 163–168, 1963.

Research Article

Modelling and Analysis of Nonstationary Vehicle-to-Infrastructure Channels with Time-Variant Angles of Arrival

Matthias Pätzold ¹ and Carlos A. Gutierrez ²

¹Faculty of Engineering and Science, University of Agder, 4898 Grimstad, Norway

²Universidad Autonoma de San Luis Potosi, 78290 San Luis Potosi, SLP, Mexico

Correspondence should be addressed to Matthias Pätzold; matthias.paetzold@uia.no

Received 17 October 2017; Revised 16 January 2018; Accepted 4 February 2018; Published 15 March 2018

Academic Editor: Enrico M. Vitucci

Copyright © 2018 Matthias Pätzold and Carlos A. Gutierrez. This is an open access article distributed under the Creative Commons Attribution License, which permits unrestricted use, distribution, and reproduction in any medium, provided the original work is properly cited.

In mobile radio channel modelling, it is generally assumed that the angles of arrival (AOAs) are independent of time. This assumption does not in general agree with real-world channels in which the AOAs vary with the position of a moving receiver. In this paper, we first present a mathematical model for the time-variant AOAs. This model serves as the basis for the development of two nonstationary multipath fading channels models for vehicle-to-infrastructure communications. The statistical properties of both channel models are analysed with emphasis on the time-dependent autocorrelation function (ACF), time-dependent mean Doppler shift, time-dependent Doppler spread, and the Wigner-Ville spectrum. It is shown that these characteristic quantities are greatly influenced by time-variant AOAs. The presented analytical framework provides a new view on the channel characteristics that goes well beyond ultra-short observation intervals over which the channel can be considered as wide-sense stationary.

1. Introduction

In a typical downlink scenario, where plane waves travel from a base station (BS) to a mobile station (MS) via a large number of fixed scattering objects, the angles of arrival (AOAs) of the received signals are changing along the moving route of the MS. Only for very short observation intervals in which the MS travels a few tens of the wavelengths [1], the temporal variation of the AOAs can be neglected justifying the wide-sense stationary assumption of multipath fading channels. The lengths of the stationary intervals during which the mobile radio channel can be considered as wide-sense stationary or quasi-stationary have been investigated (e.g., in [2–4] and the references therein). By pushing the observation interval beyond the stationary interval, the received signal captures nonstationary effects that call for new channel modelling approaches using time-frequency analysis techniques [5]. One of the effects that come with long observation intervals is that the AOAs and thus the Doppler frequencies are changing with time along the MS's moving route.

Attempts to include the temporal variations of the AOAs in mobile radio channel models have been made in [6–8]. In [6], a nonstationary multiple-input multiple-output (MIMO) vehicle-to-vehicle (V2V) channel model has been derived by assuming that the AOAs and AODs are piecewise constant. In [7], a proposal has been made for the extension of the IMT-Advanced channel model [9] by replacing the time-invariant model parameters, such as the propagation delays, AOAs, and the angels of departure (AODs) by time-variant parameters. In [8], a nonstationary one-ring model has been introduced in which the time-variant AOAs have been modelled by stochastic processes rather than random variables.

This paper is an extended version of our conference paper [10]. It expands on the recent results by studying the impact of time-variant AOAs on the statistical properties of multipath fading channels. It is shown that the multipath fading channel becomes non-wide-sense stationary if the AOAs change with time. Two new nonstationary channel models with time-variant AOAs are derived. The first one has an instantaneous channel phase that is related to the instantaneous Doppler

frequency via the phase-frequency relationship [11], while the second one is based on a sum-of-cisoids (SOC) model in which the time-independent Doppler frequencies are replaced by time-dependent Doppler frequencies. The latter approach is simple, straightforward, and intuitive but results in a less accurate nonstationary channel model. The statistical properties of both channel models are investigated with emphasis on the time-dependent autocorrelation function (ACF), time-dependent mean Doppler shift, time-dependent Doppler spread, and the Wigner-Ville spectrum. Our analysis shows that our first proposed nonstationary channel model is consistent with respect to the mean Doppler shift and the Doppler spread, while this consistency property is not fulfilled by the SOC model with time-variant Doppler frequencies. The two proposed nonstationary channel models provide a trade-off between accuracy and complexity concerning the mathematical expressions.

One of the main differences between [6–8] and our paper is that the AOAs are modelled in different ways. For example, in [6], the AOAs are modelled as piecewise constant functions, that is, these parameters are considered as constant apart from a finite number of jumps, while in our paper the AOAs are modelled in our paper as continuous time-variant functions. Another difference is that the models in [6–8] have been developed for different propagation scenarios. The V2V channel model in [6] has been developed to simulate propagation scenarios which are typical for T-junctions. The BS-to-MS channel model in [7] covers basically the same scenarios as the IMT-Advanced channel model [9], while the model in [8] is restricted to scenarios that can be generated by the one-ring model under the assumption of isotropic scattering. This contrasts with our nonstationary generic model which is not restricted to any specific propagation scenario. The drawback of the models in [6–8] is that they are inconsistent with respect to the mean Doppler shift and the Doppler spread. Our preferred model avoids this drawback by using an integral relationship between the instantaneous channel phases and the corresponding instantaneous Doppler frequencies.

The organization of this paper is as follows. Section 2 presents the derivation of two nonstationary multipath fading channel models with time-variant AOAs. Their statistical properties will be analysed in Section 3. The numerical key results of our study are visualized in Section 4. Section 5 provides guidelines for various extensions of the model. Finally, Section 6 draws the conclusion and suggests possible future research topics in relation to the issues addressed in this paper.

2. Derivation of the Nonstationary Multipath Channel Models

2.1. Time-Variant AOAs. We consider a downlink non-line-of-sight (NLOS) propagation scenario in which a fixed BS operates as transmitter, and an MS acts as receiver. It is supposed that the BS and the MS are equipped with omnidirectional antennas. The BS antenna is elevated and unobstructed by any object, whereas the MS antenna is surrounded by a large number of N fixed scattering objects called

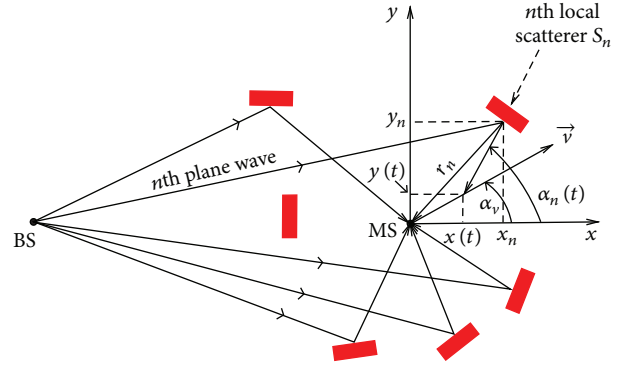


FIGURE 1: A multipath propagation scenario with time-variant AOAs $\alpha_n(t)$.

henceforth scatterers S_n ($n = 1, 2, \dots, N$). The coordinate system has been chosen such that the MS is located at the origin $(0, 0)$ of the xy -plane at $t = 0$. Furthermore, it is assumed that the MS moves with constant velocity \vec{v} in the direction determined by the angle of motion α_v as indicated in Figure 1. For reasons of clarity, this figure highlights only the location of the scatterer S_n from which the MS receives the n th multipath component (plane wave) $\mu_n(t)$ in the form of $\mu_n(t) = c_n \exp\{j\theta_n(t)\}$, where c_n denotes the path gain which is supposed to be constant, and $\theta_n(t)$ is the associated channel phase that will be studied in Section 2.3. The corresponding AOA $\alpha_n(t)$ is defined as the angle between the propagation direction of the n th incident plane wave and the x -axis, that is,

$$\alpha_n(t) = \text{atan2}(y_n - y(t), x_n - x(t)) \quad (1)$$

for $n = 1, 2, \dots, N$, where $\text{atan2}(y, x)$ denotes the four-quadrant inverse tangent function. It should be mentioned that the four-quadrant inverse tangent function $\text{atan2}(y, x)$ returns the angle of the vector (x, y) with the positive x -axis in the range $(-\pi, \pi)$. This function contrasts with the inverse tangent function $\text{atan}(y/x)$, whose results are limited to the interval $(-\pi/2, \pi/2)$. In (1), the symbols x_n and y_n denote the coordinates of the scatterer S_n ; and $x(t)$ and $y(t)$ indicate the position of the MS at time t . According to (1), the AOA $\alpha_n(t)$ is a nonlinear function of time t , which can be turned into a linear function by developing $\alpha_n(t)$ in a Taylor series around $t = 0$ and retaining only the first two terms. This results in the following model for the time-variant AOA:

$$\alpha_n(t) = \alpha_n + \gamma_n \cdot t, \quad (2)$$

where

$$\alpha_n = \alpha_n(0) = \text{atan2}(y_n, x_n), \quad (3)$$

$$\gamma_n = \left. \frac{d}{dt} \alpha_n(t) \right|_{t=0} = \frac{v}{r_n} \sin(\alpha_n - \alpha_v). \quad (4)$$

In (4), r_n denotes the distance from the scatterer S_n to the origin of the xy -plane, that is, $r_n = \sqrt{x_n^2 + y_n^2}$, as can be deduced from the geometrical model in Figure 1. In Section 4,

it is shown that the two-term Taylor series expansion of $\alpha_n(t)$ in (2) is sufficiently accurate for small observation intervals T .

2.2. Time-Variant Doppler Frequencies. Owing to the Doppler effect combined with the new feature that the AOAs $\alpha_n(t)$ vary with time, it follows that the n th incident plane wave highlighted in Figure 1 experiences a time-variant Doppler shift of $f_n(t) = f_{\max} \cos(\alpha_n(t) - \alpha_v)$ that can be expressed by using (2) as

$$f_n(t) = f_{\max} \cos(\alpha_n - \alpha_v + \gamma_n t) \quad (5)$$

for $n = 1, 2, \dots, N$, where f_{\max} stands for the maximum Doppler frequency. For a given propagation scenario with constant parameters f_{\max} , α_n , α_v , and γ_n , the time-variant Doppler shift $f_n(t)$ is a deterministic function of time. Otherwise, if one or several model parameters, for example, α_n and thus γ_n , are random variables, then $f_n(t)$ represents a stochastic process. If the MS moves during the time interval $[0, T]$, then $f_n(t)$ describes a curve starting from the initial Doppler frequency $f_n(0) = f_{\max} \cos(\alpha_n - \alpha_v)$ and ending with the finishing Doppler frequency $f_n(T) = f_{\max} \cos(\alpha_n - \alpha_v + \gamma_n T)$.

The time-dependent mean Doppler shift $B_f^{(1)}(t)$ and the time-dependent Doppler spread $B_f^{(2)}(t)$ can be computed according to

$$B_f^{(1)}(t) = \frac{\sum_{n=1}^N c_n^2 f_n(t)}{\sum_{n=1}^N c_n^2}, \quad (6)$$

$$B_f^{(2)}(t) = \sqrt{\frac{\sum_{n=1}^N c_n^2 f_n^2(t)}{\sum_{n=1}^N c_n^2} - \left(B_f^{(1)}(t)\right)^2}. \quad (7)$$

2.3. Instantaneous Channel Phase. The instantaneous channel phase $\theta_n(t)$ of the n th multipath component $\mu_n(t) = c_n \exp\{j\theta_n(t)\}$ is related to the instantaneous Doppler frequency $f_n(t)$ via the phase-frequency relationship [5, Eq. (1.3.40)]

$$\theta_n(t) = 2\pi \int_{-\infty}^t f_n(x) dx \quad (8)$$

for $n = 1, 2, \dots, N$. Using (5), the instantaneous phase $\theta_n(t)$ can be developed as follows:

$$\begin{aligned} \theta_n(t) &= 2\pi \underbrace{\int_{-\infty}^0 f_n(x) dx}_{\theta_n} + 2\pi \int_0^t f_n(x) dx \\ &= \theta_n \\ &\quad + 2\pi \frac{f_{\max}}{\gamma_n} [\sin(\alpha_n - \alpha_v + \gamma_n t) - \sin(\alpha_n - \alpha_v)], \end{aligned} \quad (9)$$

where $\theta_n = \theta_n(0)$ denotes the initial phase at $t = 0$. The initial phases θ_n are generally unknown and modelled by independent identically distributed (i.i.d.) random variables, each with uniform distribution over the interval $(0, 2\pi]$: that

is, $\theta_n \sim \mathcal{U}(0, 2\pi]$. Equation (9) tells us that the instantaneous phase $\theta_n(t)$ is not only a nonlinear function of time t but also periodic with period $T_n = 2\pi/\gamma_n$ if the AOA $\alpha_n(t)$ varies with time according to (2). In the limit $\gamma_n \rightarrow 0$, however, it can be shown by applying L'Hôpital's rule to (9) that

$$\lim_{\gamma_n \rightarrow 0} \theta_n(t) = \theta_n + 2\pi f_n t, \quad (10)$$

where $f_n = f_n(0) = f_{\max} \cos(\alpha_n - \alpha_v)$. This result reveals a linear relationship between the instantaneous phase $\theta_n(t)$ and time t , which holds only for constant AOAs $\alpha_n(t) = \alpha_n$. It should be noticed that the expression in (10) can be identified as the standard phase term of SOC channel models for Rayleigh/Rice fading channels [12, Section 4.5].

A simpler but less accurate expression than (9) can be obtained for the instantaneous phase $\theta_n(t)$ by developing $\theta_n(t)$ in a first-order Taylor series around $t = 0$ as follows:

$$\begin{aligned} \theta_n(t) &\approx \theta_n(0) + \theta'_n(0)t = \theta_n + 2\pi f_{\max} \cos(\alpha_n - \alpha_v)t \\ &= \theta_n + 2\pi f_n t, \end{aligned} \quad (11)$$

where $\theta'_n(0)$ denotes the time derivative of $\theta_n(t)$ at $t = 0$. By comparing the last two equations, we can conclude that the linear phase term $\theta_n(t) = \theta_n + 2\pi f_n t$ can be obtained from the nonlinear phase term $\theta_n(t)$ [see (9)] either in the limit $\gamma_n \rightarrow 0$ or by developing the nonlinear phase $\theta_n(t)$ in a first-order Taylor series around $t = 0$.

2.4. Complex Channel Gain. A model for the complex channel gain, denoted by $\mu(t)$, of a narrowband multipath fading channel is obtained by the superposition of all N plane wave components $\mu_n(t) = c_n \exp\{j\theta_n(t)\}$, that is,

$$\mu(t) = \sum_{n=1}^N c_n e^{j\theta_n(t)}. \quad (12)$$

Substituting the instantaneous channel phase $\theta_n(t)$ according to (9) in (12) results in the complex channel gain of the proposed nonstationary multipath fading channel with time-variant AOAs

$$\mu(t) = \sum_{n=1}^N c_n e^{j\{2\pi(f_{\max}/\gamma_n)[\sin(\alpha_n - \alpha_v + \gamma_n t) - \sin(\alpha_n - \alpha_v)] + \theta_n\}}. \quad (13)$$

On the other hand, starting from the SOC model for Rayleigh fading channels [12, Eq. (4.97)] and replacing there intuitively the time-independent Doppler frequencies f_n by the instantaneous Doppler frequencies $f_n(t)$ according to (5) provide the complex channel gain $\mu(t)$ in a much simpler form, namely,

$$\mu(t) = \sum_{n=1}^N c_n e^{j(2\pi f_n(t)t + \theta_n)}. \quad (14)$$

This intuitive mathematical manipulation results in a nonstationary channel model that is inconsistent with respect to the mean Doppler shift $B_f^{(1)}(t)$ and the Doppler spread

$B_f^{(2)}(t)$, as we will see in Section 3.2. Although the expression in (14) is mathematically simpler than the one in (13), the difference is not significant in terms of implementation costs and simulation time.

From the discussions in the previous subsection, it can be summed up that the two complex channel gains $\mu(t)$ in (13) and (14) include the original SOC model [13]

$$\mu(t) = \sum_{n=1}^N c_n e^{j(2\pi f_n t + \theta_n)} \quad (15)$$

as a special case that arises if the AOA $\alpha_n(t)$ is supposed to be either constant ($\gamma_n = 0$) or if the instantaneous phase $\theta_n(t)$ in (12) is approximated by a first-order Taylor series [see (11)]. The main difference between the three stochastic channel models above is that the former two are non-wide-sense stationary, whereas the third one is wide-sense stationary. The statistical properties of the SOC model have been studied in [13], while those of the new non-wide-sense stationary models will be analysed in the next section.

3. Analysis of the Nonstationary Multipath Channel Models

3.1. Time-Dependent ACF. The time-dependent ACF $\mathcal{R}_\mu(\tau, t)$ of a complex stochastic process $\mu(t)$ is defined as

$$\mathcal{R}_\mu(\tau, t) = E \left\{ \mu \left(t + \frac{\tau}{2} \right) \mu^* \left(t - \frac{\tau}{2} \right) \right\}, \quad (16)$$

where $E\{\cdot\}$ denotes the expectation operator and $(\cdot)^*$ stands for the complex conjugation operator. In the Appendix, it is proved that the time-dependent ACF $\mathcal{R}_\mu(\tau, t)$ of the complex channel gain $\mu(t)$ in (13) can be written as

$$\mathcal{R}_\mu(\tau, t) = \sum_{n=1}^N c_n^2 e^{j2\pi f_n(t) \cdot \text{sinc}(\gamma_n \tau / 2) \cdot \tau}, \quad (17)$$

where $\text{sinc}(\cdot)$ denotes the sinc function, which is defined by $\text{sinc}(x) = \sin(x)/x$.

Analogously, it can be shown that the time-dependent ACF $\mathcal{R}_\mu(\tau, t)$ of the complex channel gain $\mu(t)$ introduced in (14) can be expressed by

$$\mathcal{R}_\mu(\tau, t) = \sum_{n=1}^N c_n^2 e^{j2\pi [f_n(t) \cos(\gamma_n(\tau/2)) + f_n'(t) \text{sinc}(\gamma_n(\tau/2))t] \tau}, \quad (18)$$

where $f_n(t)$ is the time-variant Doppler shift in (5) and $f_n'(t)$ denotes its derivative with respect to time t .

For the special case that the AOA $\alpha_n(t)$ is constant, that is, $\gamma_n = 0$, it is obvious that the two time-dependent ACFs in (17) and (18) reduce to

$$\mathcal{R}_\mu(\tau) = \mathcal{R}_\mu(\tau, t) = \sum_{n=1}^N c_n^2 e^{j2\pi f_n \tau} \quad (19)$$

which represents the ACF of the SOC model described by (15). In this case, the ACF depends only on the time

separation τ but not on time t , which was to be expected, because the SOC process $\mu(t)$ is wide-sense stationary.

Furthermore, if $\gamma_n = 0$ and $\alpha_n \sim \mathcal{U}(0, 2\pi]$, then the expressions in (17)–(19) reduce to the ACF $\mathcal{R}_\mu(\tau) = 2\sigma_0^2 J_0(2\pi f_{\max} \tau)$, where $2\sigma_0^2 = \sum_{n=1}^N c_n^2$ denotes the mean power of the complex channel gain $\mu(t)$, and $J_0(\cdot)$ is the zeroth-order Bessel function of the first kind [14, Eq. (8.411-1)]. In other words, the proposed nonstationary multipath fading channel models include the classical Jakes/Clarke model [1, 15] as a special case.

3.2. Time-Dependent Mean Doppler Shift and Time-Dependent Doppler Spread. From the time-dependent ACF $\mathcal{R}_\mu(\tau, t)$, the time-dependent mean Doppler shift $B_\mu^{(1)}(t)$ and the time-dependent Doppler spread $B_\mu^{(2)}(t)$ can be derived by means of

$$B_\mu^{(1)}(t) = \frac{1}{2\pi j} \frac{\dot{\mathcal{R}}_\mu(0, t)}{\mathcal{R}_\mu(0, t)}, \quad (20)$$

$$B_\mu^{(2)}(t) = \frac{1}{2\pi} \sqrt{\left(\frac{\dot{\mathcal{R}}_\mu(0, t)}{\mathcal{R}_\mu(0, t)} \right)^2 - \frac{\ddot{\mathcal{R}}_\mu(0, t)}{\mathcal{R}_\mu(0, t)}}, \quad (21)$$

respectively, where $\dot{\mathcal{R}}_\mu(0, t)$ ($\ddot{\mathcal{R}}_\mu(0, t)$) denotes the first (second) order derivative of $\mathcal{R}_\mu(\tau, t)$ with respect to τ at $\tau = 0$. Inserting (17) in (20) and (21) results after some straightforward mathematical steps in the following closed-form solutions:

$$B_\mu^{(1)}(t) = \frac{\sum_{n=1}^N c_n^2 f_n(t)}{\sum_{n=1}^N c_n^2}, \quad (22)$$

$$B_\mu^{(2)}(t) = \sqrt{\frac{\sum_{n=1}^N c_n^2 f_n^2(t)}{\sum_{n=1}^N c_n^2} - (B_\mu^{(1)}(t))^2}. \quad (23)$$

A comparison of (22) with (6) and (23) with (7) reveals that the equalities $B_\mu^{(1)}(t) = B_f^{(1)}(t)$ and $B_\mu^{(2)}(t) = B_f^{(2)}(t)$ hold, from which we can conclude that the proposed nonstationary multipath fading channel model described by (13) is consistent with respect to both the mean Doppler shift and the Doppler spread.

On the other hand, if we insert (18) in (20) and (21), then we obtain

$$B_\mu^{(1)}(t) = \frac{\sum_{n=1}^N c_n^2 (f_n(t) + f_n'(t) \cdot t)}{\sum_{n=1}^N c_n^2}, \quad (24)$$

$$B_\mu^{(2)}(t) = \sqrt{\frac{\sum_{n=1}^N c_n^2 (f_n(t) + f_n'(t) \cdot t)^2}{\sum_{n=1}^N c_n^2} - (B_\mu^{(1)}(t))^2}. \quad (25)$$

This result demonstrates that the simple nonstationary channel model introduced in (14) is inconsistent with respect to the mean Doppler shift and the Doppler spread, because $B_\mu^{(1)}(t) \neq B_f^{(1)}(t)$ and $B_\mu^{(2)}(t) \neq B_f^{(2)}(t)$ hold. Concerning

the SOC process $\mu(t)$ in (15), we mention for completeness that the equalities $B_\mu^{(1)} = B_f^{(1)}$ and $B_\mu^{(2)} = B_f^{(2)}$ hold, where $B_\mu^{(1)}$ and $B_\mu^{(2)}$ are the same quantities as in (22) and (23), respectively, if we replace $f_n(t)$ by f_n . Thus, the SOC model is consistent with respect to the mean Doppler shift and the Doppler spread. More information on the consistency of nonstationary multipath fading channels can be found in [16].

3.3. Wigner-Ville Spectrum. The Wigner-Ville spectrum, which is also called the time-varying spectrum or the evolutive spectrum, will be denoted by $\mathcal{S}_\mu(f, t)$. This function is defined as the Fourier transform of the time-dependent ACF $\mathcal{R}_\mu(\tau, t)$ with respect to τ [11]: that is,

$$\mathcal{S}_\mu(f, t) = \int_{-\infty}^{\infty} \mathcal{R}_\mu(\tau, t) e^{-j2\pi f\tau} d\tau. \quad (26)$$

Inserting (17) in (26) and using the property $\mathcal{R}_\mu(\tau, t) = \mathcal{R}_\mu^*(-\tau, t)$, we can express the Wigner-Ville spectrum $\mathcal{S}_\mu(f, t)$ of the proposed nonstationary multipath fading channel model described by (13) as

$$\begin{aligned} \mathcal{S}_\mu(f, t) &= 2 \sum_{n=1}^N c_n^2 \int_0^{\infty} \cos \left\{ 2\pi \left[f - f_n(t) \operatorname{sinc} \left(\gamma_n \frac{\tau}{2} \right) \right] \tau \right\} d\tau. \end{aligned} \quad (27)$$

For the wide-sense stationary case, for which $\gamma_n = 0$ holds, the Wigner-Ville spectrum $\mathcal{S}_\mu(f, t)$ in (27) reduces to the Doppler power spectral density (PSD) of the SOC process $\mu(t)$ presented in (15), that is,

$$\mathcal{S}_\mu(f) = \sum_{n=1}^N c_n^2 \delta(f - f_n). \quad (28)$$

Furthermore, for the isotropic scattering case, in which c_n and α_n are i.i.d. random variables with $E\{c_n^2\} = 2\sigma_0^2/N$ and $\alpha_n \sim \mathcal{U}(0, 2\pi]$, we obtain the Jakes/Clarke PSD [1, 15] after computing the expected value of $\mathcal{S}_\mu(f)$ in (28). Hence, the Wigner-Ville spectrum $\mathcal{S}_\mu(f, t)$ in (27) includes the classical Jakes/Clarke Doppler spectrum as a special case.

4. Numerical Results

This section presents a selection of numerical results to illustrate the main findings of this paper. In all considered propagation scenarios, we have set the number of multipath components N to $N = 10$. The gains c_n and initial AOs $\alpha_n = \alpha_n(0)$ have been computed by using the extended method of exact Doppler spread (EMEDS) [17]. According to this method, the parameters c_n and α_n are given by

$$c_n = \sigma_0 \sqrt{\frac{2}{N}}, \quad (29)$$

$$\alpha_n = \frac{2\pi}{N} \left(n - \frac{1}{4} \right), \quad (30)$$

respectively, and the initial phases $\theta_n = \theta_n(0)$ are considered as realizations of independent random variables, each characterized by a uniform distribution over the interval $(0, 2\pi]$. If

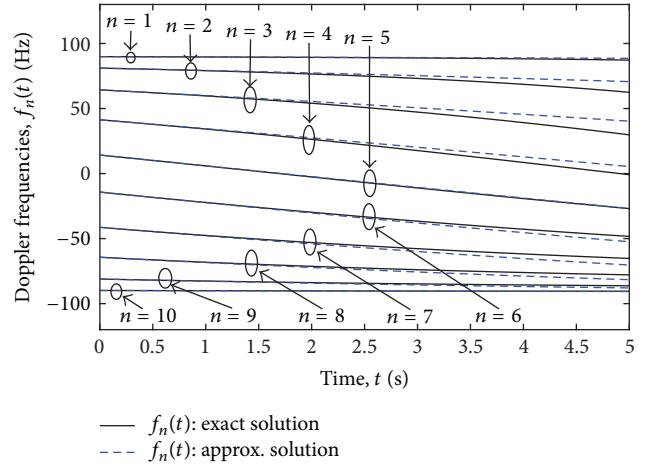


FIGURE 2: Trend of the time-variant Doppler frequencies $f_n(t)$ ($n = 1, 2, \dots, N$) by using the exact solution (black solid line) and the approximate solution (blue dashed line), where $N = 10$.

not stated otherwise, the radii r_n in Figure 1 have been set to 50 m for all $n = 1, 2, \dots, N$. For the mean power (variance) σ_0^2 of the in-phase and quadrature components of $\mu(t)$, we have chosen the value $\sigma_0^2 = 1$. The carrier frequency was set to 5.9 GHz, and the maximum Doppler frequency f_{\max} was supposed to be $f_{\max} = 91$ Hz. This corresponds to a mobile speed of $v = |\vec{v}| = 16.65$ km/h, where we have assumed that the MS moves in x -direction, implying that the angle of motion α_v equals zero, that is, $\alpha_v = 0$.

Figure 2 depicts the trend of the time-variant Doppler frequencies $f_n(t)$ by using the exact expression for the AOs $\alpha_n(t)$ according to (1). For comparison, this figure also shows the behaviour of $f_n(t)$ for the approximate solution of $\alpha_n(t)$ in (2). Figure 2 shows clearly that the first-order approximation is quite good over the interval from 0 to 2.162 s during which the MS has covered a distance of 10 m.

Figure 3 illustrates the signal envelope $|\mu(t)|$ by using the SOC model [see (15), Case I], the proposed nonstationary multipath fading channel model [see (13), Case II], and the simple nonstationary model [see (14), Case III]. This figure demonstrates clearly that the temporal variations of the AOs $\alpha_n(t)$ have a great influence on the temporal behaviour of the signal envelope $|\mu(t)|$. It is interesting to note that the three signal envelopes are identical at $t = 0$ and very similar for small values of $t > 0$, but they differ considerably with increasing values of t . It should be mentioned that different realizations of the initial phases $\theta_n = \theta_n(0)$ result in different sample functions of the signal envelopes, but the aforementioned trend is the same for all realizations.

Figures 4 and 5 present the ACF $\mathcal{R}_\mu(\tau)$ of the SOC process $\mu(t)$ in (15) and the time-dependent ACF $\mathcal{R}_\mu(\tau, t)$ of the nonstationary process $\mu(t)$ in (13), respectively. It can be observed that both ACFs are identical at the origin $t = 0$, but the temporal correlation properties of the nonstationary model differ more and more if time t proceeds. This means that the temporal variations of $\alpha_n(t)$ influence greatly the fading behaviour of the signal envelope $|\mu(t)|$.

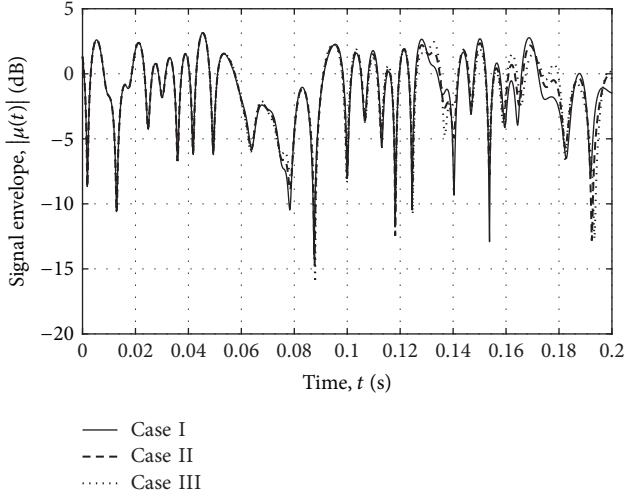


FIGURE 3: Illustration of the signal envelope $|\mu(t)|$ of a sample function of a wide-sense stationary SOC process [see (15)] in comparison with the signal envelopes $|\mu(t)|$ of the nonstationary processes described by (13) and (14).

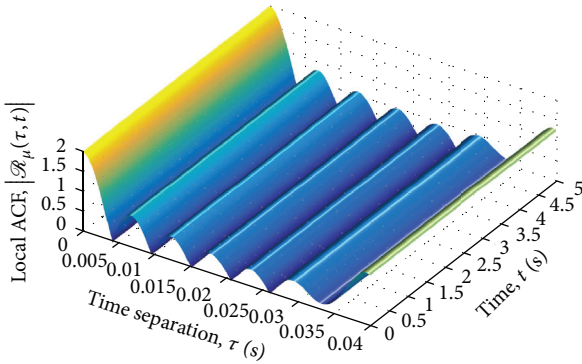


FIGURE 4: ACF $\mathcal{R}_\mu(\tau) = \mathcal{R}_\mu(\tau, t)$ of a SOC process $\mu(t)$ with constant AOAs α_n for $N = 10$.

Figures 6 and 7 depict the corresponding Doppler PSD $\mathcal{S}_\mu(f)$ [see (28)] of the SOC process $\mu(t)$ in (15) and the Wigner-Ville spectrum $\mathcal{S}_\mu(f, t)$ [see (27)] of the nonstationary process $\mu(t)$ in (13), respectively. A comparison of the two spectral representations shows clearly that the influence of the time-variant AOAs $\alpha_n(t)$ cannot be neglected. This statement is obvious as the Doppler frequencies of the Wigner-Ville spectrum (Doppler PSD) associated with the stationary SOC process remain constant over time t (see Figure 6), while the spectral components of the nonstationary process experience a drift if time t proceeds (see Figure 7). Finally, we mention that the results in Figure 7 have been obtained numerically by setting the upper limit of τ in the integral of (27) to $\tau = \tau_{\max} = 1$ s and evaluating the integral by considering $N_s = 1000$ samples, which results in a resolution of $\tau_{\max}/N_s = 0.001$ s.

Figures 8 and 9 are devoted to a study on the influence of the (ring) radii r_n on the time-dependent mean Doppler shift $B_\mu^{(1)}(t)$ and the time-dependent Doppler spread $B_\mu^{(2)}(t)$, respectively. The presented graphs show that the smaller the

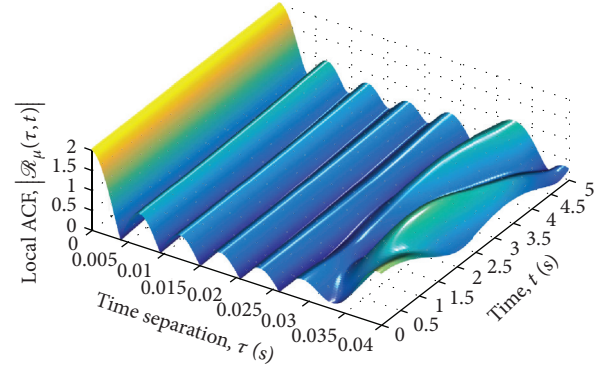


FIGURE 5: Time-dependent ACF $\mathcal{R}_\mu(\tau, t)$ of the proposed nonstationary process $\mu(t)$ with time-variant AOAs $\alpha_n(t)$ for $N = 10$.

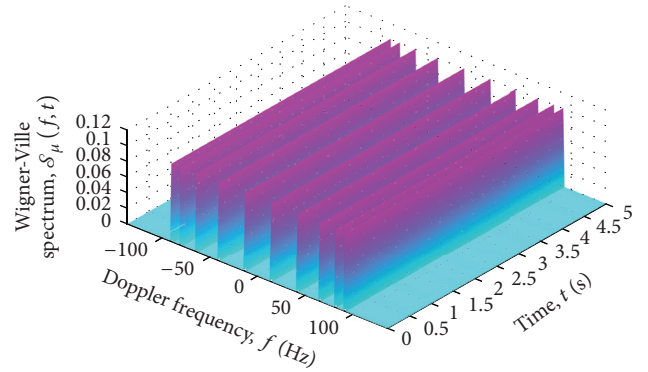


FIGURE 6: Wigner-Ville spectrum (Doppler PSD) $\mathcal{S}_\mu(f) = \mathcal{S}_\mu(f, t)$ of an SOC process $\mu(t)$ with constant AOAs α_n for $N = 10$.

radii r_n are, the faster the functions $B_\mu^{(1)}(t)$ and $B_\mu^{(2)}(t)$ are changing over time t . Figure 8 shows also a comparison between the time-dependent mean Doppler shift $B_\mu^{(1)}(t)$ of the consistent model described by (14) and the inconsistent model according to (15). Both models have the same mean Doppler shift $B_\mu^{(1)}(t)$ at the origin $t = 0$, but the mean Doppler shifts deviate considerably from each other with increasing values of time t . The same statement holds for the time-dependent Doppler spread shown in Figure 9. These results underline the importance of consistency, as the deviations between (22) and (24) as well as between (23) and (25) cannot be neglected.

5. Model Extensions

To isolate the effect of time-variant AOAs on the Doppler characteristic, we have assumed that the channel is frequency-nonspecific and that the transmitter and receiver are equipped with single omnidirectional antennas. To relax these assumptions, we will provide some guidelines on model extensions in the following subsections.

5.1. Extension to Frequency-Selectivity. Starting from the narrowband multipath fading channel model in (12) and taking into account the fact that the n th plane wave component

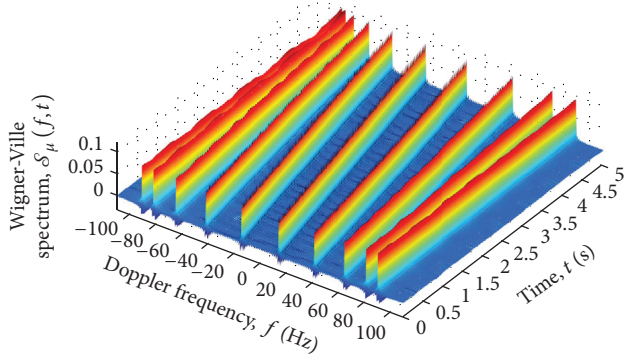


FIGURE 7: Wigner-Ville spectrum $S_\mu(f, t)$ of the proposed nonstationary process $\mu(t)$ with time-variant AOAs $\alpha_n(t)$ for $N = 10$.

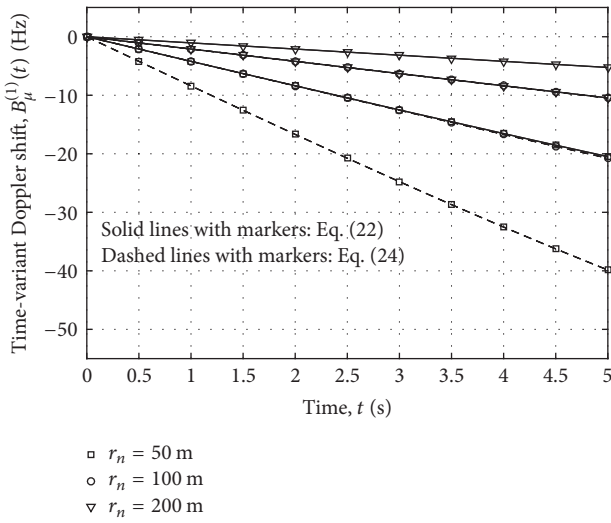


FIGURE 8: Time-dependent mean Doppler shift $B_\mu^{(1)}(t)$ of the nonstationary channel models for different values of the radii r_n .

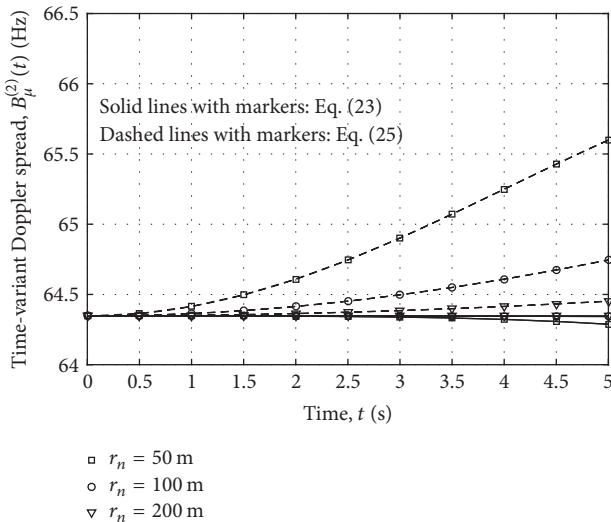


FIGURE 9: Time-dependent Doppler spread $B_\mu^{(2)}(t)$ of the nonstationary channel models for different values of the radii r_n for $n = 1, 2, \dots, N$ ($N = 10$).

$\mu_n(t) = c_n \exp\{j\theta_n(t)\}$ will be received after a time-variant propagation delay denoted by $\tau'_n(t)$, the impulse response $h(\tau', t)$ of the resulting non-wide-sense stationary single-input single-output channel model can be expressed as

$$h(\tau', t) = \sum_{n=1}^N c_n e^{j\theta_n(t)} \delta(\tau' - \tau'_n(t)), \quad (31)$$

where $\theta_n(t)$ is given by (9) for the consistent model or by $\theta_n(t) = 2\pi f_n(t)t + \theta_n$ for the inconsistent model. The time-variant delay $\tau'_n(t)$ can be derived from the geometrical model in Figure 1 as

$$\tau'_n(t) = \frac{1}{c_0} \left[\sqrt{(D + x_n)^2 + y_n^2} + r_n(t) \right], \quad (32)$$

where c_0 denotes the speed of light, D is the distance between the BS and MS, and $r_n(t) = \sqrt{(x_n - x(t))^2 + (y_n - y(t))^2}$.

5.2. *Extension to MIMO.* Let $h_{k\ell}(\tau', t)$ denote the impulse response of a frequency-selective MIMO channel with M_T transmit and M_R receive antennas; then the propagation link from the ℓ th transmit antenna to the k th receive antenna can be modelled as

$$h_{k\ell}(\tau', t) = \sum_{n=1}^N g_{k\ell n}(t) e^{j\theta_n(t)} \delta(\tau' - \tau'_n(t)) \quad (33)$$

for $k = 1, 2, \dots, M_R$ and $\ell = 1, 2, \dots, M_T$, where $g_{k\ell n}(t)$ is the same as in [18, Eq. (9)] apart from the fact that we have to replace there the time-invariant quantities r_n and α_n^R by time-variant quantities $r_n(t)$ and $\alpha_n^R(t)$, respectively. The expression in (33) can be derived by applying the design steps of the generalized principle of deterministic channel modelling [12, Section 8.1].

5.3. *Other Model Extensions.* The proposed model is only applicable to omnidirectional antennas. The extension to directional antennas is possible through a proper adjustment of the constant path gains c_n , which have to be replaced by time-variant path gains $c_n(t)$. The temporal characteristics of $c_n(t)$ depend on the antenna pattern and the direction in which the MS moves. It is also possible to consider birth-and-death effects of the scatterers. This extension results in a multiplication of each multipath component by a birth-and-death process or, equivalently, by replacing the time-invariant path gains c_n by proper time-variant path gains $c_n(t)$. The analysis of the Wigner-Ville spectrum of nonstationary mobile radio channels with time-variant path gains $c_n(t)$ is substantially different from the analysis in Section 3.3 and beyond the scope of this paper.

6. Conclusion

In this paper, we have developed and analysed multipath fading channel models with time-variant AOAs. Our study has shown that the effect of time-variant AOAs results

in a non-wide-sense stationary multipath fading channel model. Expressions have been derived for the time-dependent ACF, time-dependent mean Doppler shift, time-dependent Doppler spread, and the Wigner-Ville spectrum of the proposed non-wide-sense stationary channel model. By comparing these statistical quantities with known results of studies assuming constant AOAs, we can conclude that the assumption of constant AOAs is only justified for very short observation intervals. The proposed nonstationary channel model allows extending the observation interval over a wider range without losing accuracy. The price for this added accuracy is a higher degree of complexity concerning the mathematical expressions.

One of the remaining problems that might be tackled in an upcoming study is to develop quantitative methods for the investigation of the length of the observation interval over which the proposed nonstationary channel models are sufficiently accurate. Another topic could be to extend the presented framework to the modelling of MIMO channels with time-dependent AOAs.

Appendix

Derivation of the Time-Dependent ACF

$\mathcal{R}_\mu(\tau, t)$ in (17)

Substituting (13) in the definition of the time-dependent ACF

$\mathcal{R}_\mu(\tau, t) = E\{\mu(t + \tau/2)\mu^*(t - \tau/2)\}$ gives

$$\begin{aligned} \mathcal{R}_\mu(\tau, t) &= E \left\{ \sum_{n=1}^N \sum_{m=1}^N c_n c_m e^{j2\pi(f_{\max}/\gamma_n)[\sin(\alpha_n - \alpha_v + \gamma_n(t + \tau/2)) - \sin(\alpha_n - \alpha_v)] + \theta_n} \right. \\ &\quad \left. \cdot e^{-j2\pi(f_{\max}/\gamma_m)[\sin(\alpha_m - \alpha_v + \gamma_m(t - \tau/2)) - \sin(\alpha_m - \alpha_v)] + \theta_m} \right\}. \end{aligned} \quad (\text{A.1})$$

Using $E\{e^{j(\theta_n - \theta_m)}\} = 1$ if $n = m$ and 0 if $n \neq m$, we obtain

$$\begin{aligned} \mathcal{R}_\mu(\tau, t) &= \sum_{n=1}^N c_n^2 e^{j2\pi(f_{\max}/\gamma_n)\sin(\alpha_n - \alpha_v + \gamma_n(t + \tau/2))} \\ &\quad \cdot e^{-j2\pi(f_{\max}/\gamma_n)\sin(\alpha_n - \alpha_v + \gamma_n(t - \tau/2))} \\ &= \sum_{n=1}^N c_n^2 e^{j2\pi(f_{\max}/(\gamma_n/2))\cos(\alpha_n - \alpha_v + \gamma_n t)\sin(\gamma_n(\tau/2))} \\ &= \sum_{n=1}^N c_n^2 e^{j2\pi f_n(t)\text{sinc}(\gamma_n \tau/2)\tau}, \end{aligned} \quad (\text{A.2})$$

where we have used the sinc function defined as $\text{sinc}(x) = \sin(x)/x$.

Conflicts of Interest

The authors declare that there are no conflicts of interest regarding the publication of this paper.

References

- [1] W. C. Jakes, Ed., *Microwave Mobile Communications*, IEEE Press, Piscataway, NJ, USA, 1994.
- [2] R. He, O. Renaudin, V.-M. Kolmonen et al., "Characterization of quasi-stationarity regions for vehicle-to-vehicle radio channels," *IEEE Transactions on Antennas and Propagation*, vol. 63, no. 5, pp. 2237–2251, 2015.
- [3] D. Umansky and M. Pätzold, "Stationarity test for wireless communication channels," in *Proceedings of the 2009 IEEE Global Telecommunications Conference, GLOBECOM 2009*, Honolulu, Hawaii, USA, December 2009.
- [4] A. Ispas, C. Schneider, G. Ascheid, and R. Thomä, "Analysis of the local quasi-stationarity of measured dual-polarized MIMO channels," *IEEE Transactions on Vehicular Technology*, vol. 64, no. 8, pp. 3481–3493, 2015.
- [5] B. Boashash, Ed., *Time-Frequency Signal, Analysis and Processing: A Comprehensive Reference*, Elsevier Academic Press, 2nd edition edition, 2015.
- [6] A. Chelli and M. Pätzold, "A non-stationary MIMO vehicle-to-vehicle channel model based on the geometrical T-junction model," in *Proceedings of the 2009 International Conference on Wireless Communications and Signal Processing, WCSP 2009*, Nanjing, China, November 2009.
- [7] Z. Zhu, Y. Zhu, T. Zhang, and Z. Zeng, "A time-variant MIMO channel model based on the IMT-Advanced channel model," in *Proceedings of the 2012 International Conference on Wireless Communications and Signal Processing, WCSP 2012*, Huangshan, China, 2012.
- [8] A. Borhani and M. Pätzold, "A non-stationary one-ring scattering model," in *Proceedings of the 2013 IEEE Wireless Communications and Networking Conference, WCNC 2013*, pp. 2661–2666, Shanghai, China, April 2013.
- [9] ITU-R Rep. M2135, "Guidelines for evaluation of radio interface technologies for IMT-Advanced," 2008, https://www.itu.int/dms_pub/itu-r/opb/rep/R-REP-M.2135-2008-PDF-E.pdf.
- [10] M. Pätzold and C. A. Gutiérrez, "Modelling and analysis of nonstationary multipath fading channels with time-variant angles of arrival," in *Proceedings of the 2017 IEEE 85th Vehicular Technology Conference (VTC Spring)*, Sydney, Australia, June 2017.
- [11] W. Martin, "Time-frequency analysis of random signals," in *Proceedings of the IEEE International Conference on Acoustics, Speech, and Signal Processing*, vol. 3, pp. 1325–1328, Paris, France, May 1982.
- [12] M. Pätzold, *Mobile Radio Channels*, John Wiley & Sons, Chichester, England, 2nd edition edition, 2011.
- [13] M. Pätzold and B. Talha, "On the statistical properties of sum-of-cisoidsbased mobile radio channel simulators," in *Proceedings of the 10th International Symposium on Wireless Personal Multimedia Communications, WPMC 2007*, pp. 394–400, Jaipur, India, 2007.
- [14] I. S. Gradshteyn and I. M. Ryzhik, *Table of Integrals, Series, and Products*, Elsevier Academic Press, 7th edition edition, 2007.
- [15] R. H. Clarke, "A statistical theory of mobile-radio reception," *Bell Labs Technical Journal*, vol. 47, no. 6, pp. 957–1000, 1968.
- [16] M. Pätzold, C. A. Gutiérrez, and N. Youssef, "On the consistency of non-stationary multipath fading channels with respect to the average doppler shift and the doppler spread," in *Proceedings of the 2017 IEEE Wireless Communications and Networking Conference, WCNC 2017*, San Francisco, CA, USA, March 2017.

- [17] M. Pätzold, B. O. Hogstad, and N. Youssef, "Modeling, analysis, and simulation of MIMO mobile-to-mobile fading channels," *IEEE Transactions on Wireless Communications*, vol. 7, no. 2, pp. 510–520, 2008.
- [18] M. Pätzold and C. A. Gutiérrez, "Enhancing the Resolution of the Spectrogram of Non-Stationary Mobile Radio Channels by Using Massive MIMO Techniques," in *Proceedings of the 2017 IEEE 86th Vehicular Technology Conference (VTC-Fall)*, Toronto, Canada, September 2017.

Research Article

A Triply Selective MIMO Channel Simulator Using GPUs

R. Carrasco-Alvarez ¹, **R. Carreón-Villal**,¹ **J. Vázquez Castillo** ², **J. Ortegón Aguilar**,²
O. Longoria-Gandara,³ and **A. Castillo Atoche**⁴

¹Department of Electronic Engineering, UDG-CUCEI, 44430 Guadalajara, JAL, Mexico

²Department of Engineering, Universidad de Quintana Roo, 77019 Chetumal, QROO, Mexico

³Department of Electronics, Systems, and IT, ITESO, 45604 Tlaquepaque, JAL, Mexico

⁴Department of Mechatronics, Universidad Autónoma de Yucatán, 97000 Mérida, YUC, Mexico

Correspondence should be addressed to R. Carrasco-Alvarez; r.carrasco@academicos.udg.mx

Received 29 September 2017; Revised 23 January 2018; Accepted 6 February 2018; Published 5 March 2018

Academic Editor: Neji Youssef

Copyright © 2018 R. Carrasco-Alvarez et al. This is an open access article distributed under the Creative Commons Attribution License, which permits unrestricted use, distribution, and reproduction in any medium, provided the original work is properly cited.

A methodology for implementing a triply selective multiple-input multiple-output (MIMO) simulator based on graphics processing units (GPUs) is presented. The resulting simulator is based on the implementation of multiple double-selective single-input single-output (SISO) channel generators, where the multiple inputs and the multiple received signals have been transformed in order to supply the corresponding space correlation of the channel under consideration. A direct consequence of this approach is the flexibility provided, which allows different propagation statistics to each SISO channel to be specified and thus more complex environments to be replicated. It is shown that under some specific constraints, the statistics of the triply selective MIMO simulator are the same as those reported in the state of art. Simulation results show the computational time improvement achieved, up to 650-fold for an 8×8 MIMO channel simulator when compared with sequential implementations. In addition to the computational improvement, the proposed simulator offers flexibility for testing a variety of scenarios in vehicle-to-vehicle (V2V) and vehicle-to-infrastructure (V2I) systems.

1. Introduction

With the growing demand by users of rapid transfer of high amounts of data, it has been necessary to develop new transmissions strategies and, consequently, to verify their performance in order to accomplish the established goals. In this sense, multiple-input multiple-output (MIMO) simulator has been considered in recent years a fundamental part of new communication standards embraced by long-term evolution-vehicle (LTE-V) and vehicle-to-vehicle (V2V) technologies. This is due to the fact that MIMO can take advantage of space diversity and multipath scattering for increasing the data transmission rate considerably in comparison with single-input single-output (SISO) communication systems [1]. Because of its relevance, several mathematical channel models and hence diverse channel simulators/emulators have been proposed in order to prove the performance of MIMO-based communication systems.

In this sense, as summarized by [2], MIMO channel models can be classified in diverse ways; the broadest classification considers physical models and analytical models. Physical models take into account the electromagnetic propagation and the environment under study for obtaining a channel model. Moreover, such models can be categorized as deterministic models [3], geometric-based stochastic models [4], or stochastic models [5, 6]. Analytical models, on the other hand, abstract the complex electromagnetic propagation mechanisms into tractable channel impulse responses for modeling the MIMO channels. Moreover, analytical models can be classified as propagation-based models and correlation-based models, where the distinguished Kronecker model [7] and the Weichselberger model [8] fit in the latter classification. These models are the most commonly used models for simulating MIMO channels due to their simplicity and the conceptualization of the propagation environment.

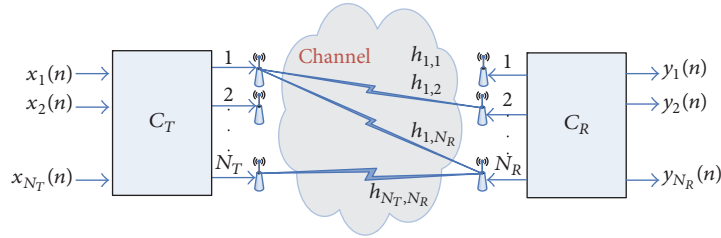


FIGURE 1: MIMO system of $N_T \times N_R$ antennas.

This paper considers an analytical model based on correlation, which assumes a triply selectivity; that is, the propagation channel for each transmitter and receiver antenna pair presents both time and frequency selectivity and a spatial correlation. This model was chosen to capture the nature of the propagation channel with greater precision. As expected, the implementation of this triply selective channel simulator is highly complex; for example, if a MIMO system made up of $N_T = 8$ transmitter antennas and $N_R = 8$ receiver antennas is considered, then it is necessary to implement $N_T \times N_R = 64$ independent SISO channel simulators in parallel. This number of SISO channels increases as well as the number of antennas is increased. Therefore, graphics processing units and GPU-accelerated computing techniques can help to manage the computational complexity in the MIMO channel simulator.

The GPU-accelerated computing techniques use the GPU together with CPUs, which are available in affordable computers or servers. The purpose is to accelerate scientific computation and engineering calculations, among others. As a result, several works related to wireless channel simulators have been presented in order to handle the computational complexity in the implementation of channel simulators [9–12] and high demanding digital signal processing algorithms [13, 14].

In [9], the authors present a GPU-based implementation, which uses the filtering method for developing a doubly selective SISO channel simulator (frequency and time selective). In [10], a full 3-D GPU-based beam-tracing method is presented for propagation modeling in complex indoor environments. Likewise, the study in [11] presents an improved path loss simulation incorporating a three-dimensional terrain model using parallel coprocessors or GPUs. In addition, in [12] and references therein, a selection of GPU-based implementations is presented, which improves the computational processing time and reports GPU-based implementations with significant speedups. However, even though many GPU-based implementations have been reported in the state of the art, a complete triply selective fading channel simulator has not been reported in the open literature. Examples of complete MIMO fading channel simulators and emulators can be found in [15–17], but these architectures do not exploit the triple selectivity at the same time, or they configure the hardware with a low number of antennas.

This paper presents a triply selective MIMO channel simulation methodology using GPU techniques; the methodology will be based on SISO channel generators presented in

[9]. This simulator includes the phenomenology of the propagation environment (time, frequency and space selectivities), which has been left out of the state-of-art simulators due to the computational complexity. Likewise, the introduced methodology exhibits enough flexibility for implementing channel simulators with different MIMO channel configurations.

1.1. Notation. Bold upper (lower) case letters are used for denoting matrices (vectors); $(\cdot)^T$, $(\cdot)^H$, $\lceil \cdot \rceil$, and $E(\cdot)$ denote transpose, complex transpose (Hermitian), the ceil function, and the expectation operator, respectively. $[A]_{i,j}$ denotes the element in the i th row and j th column of A . $\text{vec}(A)$ is the reordering of the columns of A into a single column vector. $\text{diag}(\mathbf{a})$ is a diagonal matrix whose elements are those from vector \mathbf{a} . \mathbf{I}_j denotes an identity matrix of length $j \times j$. Finally, \otimes stands for the Kronecker product of two matrices.

1.2. Organization. The paper is organized as follows: in Section 2, the mathematical model of the triply selective channel is analyzed. The methodology for implementing this mathematical model using GPUs is described in Section 3. Implementation results assuming diverse scenarios are presented in Section 4. Finally, some concluding remarks in Section 5 close this paper.

2. Triply Selective Channel Model

Assume a baseband discrete time MIMO communication channel that presents time, frequency, and spatial selectivity (triple-selective channel). Moreover, consider that this communication system is conformed of N_T transmit antennas and N_R receive antennas as depicted in Figure 1. This system can be envisaged as an array of $N_T \times N_R$ SISO channels where a transmitter and a receiver correlation stage are included in order to provide the corresponding spatial correlation statistics. Without loss of generality, if it is stated that all the SISO channels are modeled as FIR filters of L coefficients, then the MIMO system at time index n can be expressed mathematically as follows:

$$\mathbf{y}(n) = \mathbf{C}_R \mathbf{H}(n) \widehat{\mathbf{C}}_T \mathbf{x}(n), \quad (1)$$

where $\mathbf{y}(n) \in \mathbb{C}^{N_R}$ with $\mathbf{y}(n) = [y_1(n), y_2(n), \dots, y_{N_R}(n)]^T$ is a vector containing the samples received from each antenna, $\mathbf{C}_R \in \mathbb{C}^{N_R \times N_R}$ is the matrix that provides the spatial correlation due to the receive antennas, and $\widehat{\mathbf{C}}_T = \mathbf{C}_T \otimes \mathbf{I}_L$,

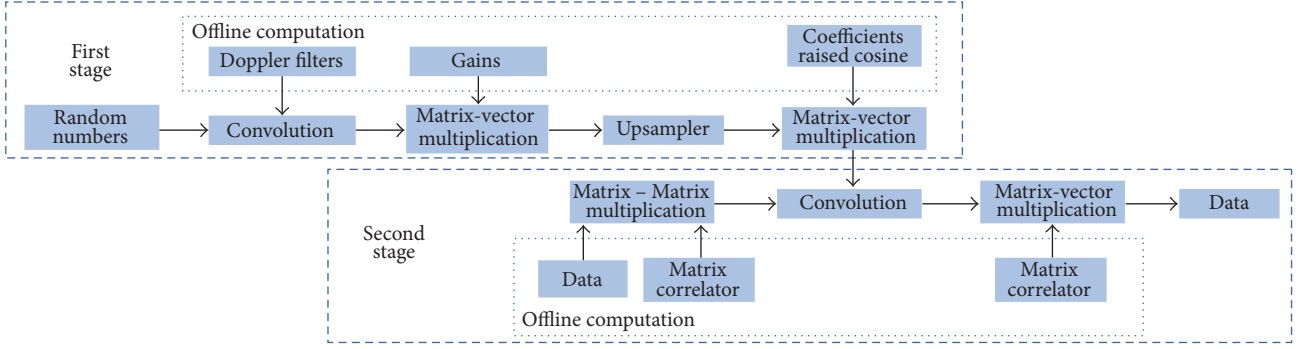


FIGURE 2: Triply selective MIMO channel simulator scheme.

Substituting (9) into (5), $\mathbf{R}_{\mathbf{H}^T}(n_1, n_2)$ is

$$\begin{aligned} \mathbf{R}_{\mathbf{H}^T}(n_1, n_2) &= (\mathbf{C}_R \otimes \widehat{\mathbf{C}}_T^T) \mathcal{F}(\widetilde{\Sigma} \widetilde{\Lambda}(n_1 - n_2)) \mathcal{F}^H(\mathbf{C}_R \otimes \widehat{\mathbf{C}}_T^T)^H. \end{aligned} \quad (11)$$

Function (11) is the autocorrelation function of the proposed model (3). It is possible to observe that this model offers great flexibility by allowing the subchannels to have different statistics, for example, different power delay profile (PDP) and power Doppler spectrum (PDS). As a special case, if all the paths of all subchannels are forced to have the same PDS, then $\widetilde{\Lambda}(n_1 - n_2) = \mathbf{I}f(n_1 - n_2)$, where $f(n_1 - n_2)$ is the autocorrelation function of all the paths. As a particular case, if Jakes' model is considered, where the different scatters propagate in the azimuth plane and arrive at the receivers with an angle of arrival distributed uniformly between $[0, 2\pi]$, then $f(n_1 - n_2) = J_0(2\pi f_{\max}(n_1 - n_2)T_s)$, where $J_0(\cdot)$ is the Bessel function of order 0 and f_{\max} is the maximum Doppler frequency. If it is also considered that all the subchannels have the same PDP composed of P paths, then $\widetilde{\Sigma}^2 = \mathbf{I}_{N_T N_R} \otimes \Sigma_e^2$ and $\mathcal{F} = \mathbf{I}_{N_T N_R} \otimes \mathbf{G}_e$, where $\Sigma_e^2 \in \mathbb{R}^{P \times P}$ is a diagonal matrix containing the gains of the paths and $\mathbf{G}_e \in \mathbb{R}^{L \times P}$ is calculated as in (8). However, assuming that the paths of all the subchannels have the same delay, then (11) transforms into (12), which coincides with the model proposed in [16]:

$$\begin{aligned} \mathbf{R}_{\mathbf{H}^T}(n_1, n_2) &= \left((\mathbf{C}_R \otimes (\mathbf{C}_T \otimes \mathbf{I}_L)^T) (\mathbf{I}_{N_T N_R} \otimes \mathbf{G}_e) \right. \\ &\quad \cdot (\mathbf{I}_{N_T N_R} \otimes \Sigma_e^2) (\mathbf{I}_{N_T N_R} \otimes \mathbf{G}_e)^H \\ &\quad \cdot (\mathbf{C}_R \otimes (\mathbf{C}_T \otimes \mathbf{I}_L)^T)^H \Big) J_0(2\pi f_{\max}(n_1 - n_2)T_s) \\ &= \left(((\mathbf{C}_R \otimes \mathbf{C}_T^T) \otimes \mathbf{I}_L^T) (\mathbf{I}_{N_T N_R} \otimes \mathbf{G}_e \Sigma_e^2 \mathbf{G}_e^H) \right. \\ &\quad \cdot ((\mathbf{C}_R \otimes \mathbf{C}_T^T) \otimes \mathbf{I}_L^T)^H \Big) J_0(2\pi f_{\max}(n_1 - n_2)T_s) \\ &= \left(((\mathbf{C}_R \otimes \mathbf{C}_T^T) (\mathbf{C}_R \otimes \mathbf{C}_T^T)^H) \otimes (\mathbf{G}_e \Sigma_e^2 \mathbf{G}_e^H) \right) \end{aligned}$$

$$\begin{aligned} \cdot J_0(2\pi f_{\max}(n_1 - n_2)T_s) &= (\mathbf{C}_R \mathbf{C}_R^H \otimes \mathbf{C}_T^T (\mathbf{C}_T^T)^H) \\ &\quad \otimes (\mathbf{G}_e \Sigma_e^2 \mathbf{G}_e^H) J_0(2\pi f_{\max}(n_1 - n_2)T_s). \end{aligned} \quad (12)$$

3. GPU Implementation

The simulator implementation takes advantage of the parallel capabilities of General-Purpose Computing on GPU (GPGPU) and the use of the VexCL library [19]. VexCL is an OpenCL/CUDA library developed in C++ by Denis Demidov. It supports multidevice, multiplatform computations and provides functions for floating-point vector/matrix operations. VexCL uses vector expressions, which are automatically processed in parallel across all devices.

The simulation process comprises two stages: channel coefficient generation and data frame processing. These stages are depicted in Figure 2. The first stage corresponds to the generation of the elements of matrix \mathbf{H} of (2); the second stage represents (1).

3.1. Complex Operations. GPU frameworks, like OpenCL and CUDA, do not provide complex data types; the closest data type is the 2-vector type `cl_double2` of OpenCL. Hence, custom vex functions were implemented to perform addition and multiplication of complex numbers. These functions are used in vector expressions. The codes implemented for performing the multiplication and addition of complex numbers are presented in Listings 1 and 2, respectively. The previous functions receive two 2-vectors used as complex numbers.

3.2. Channel Coefficient Generation. The channel coefficients require random numbers, which are filtered for generating the channel taps with specific PDS and correlation.

3.2.1. Random Number Generation. VexCL provides templates to generate random numbers; they are based on Random123 [20, 21]. The templates support the Philox generator family (based on integer multiplication) or the Threefry family (based on Threefish encryption). It is possible to generate uniformly distributed random numbers with the Random

```
VEX_FUNCTION(cl_double2, cmul,
             (cl_double2, a) (cl_double2, b),
             double2 c = {
                 a.x * b.x - a.y * b.y,
                 a.x * b.y + a.y * b.x
             });
return c;
);
```

LISTING 1: Multiplication code.

```
VEX_FUNCTION(cl_double2, csum,
             (cl_double2, a) (cl_double2, b),
             double2 c = {
                 a.x + b.x, a.y + b.y
             });
return c;
);
```

LISTING 2: Sum code.

template. Additionally, there are RandomNormal templates that use the Box-Muller transform to generate normally distributed random numbers. In this implementation,

```
vex::RandomNormal<cl_double2,
vex::random::threefry > random_numbers
```

are used as a C++ functor. A double random number vector is generated with

```
noise=random_numbers(vex::element_index(),
123),
```

where `noise` is a vector of $nSamples \times \sum_{i=1}^{N_T} \sum_{j=1}^{N_R} P_{i,j}$ of pairs of double precision floating-point numbers, `vex::element_index()` is the function to get the n th random number, and 123 is the seed for the generator. Instead of using doubles, the vector `noise` is composed of `cl_double2` numbers; for example, a pair of double precision numbers is used as complex numbers.

3.2.2. Doppler Filter. The generated complex random numbers are passed through a filter which provides the corresponding time domain statistics. The transfer function of this filter is the square root of the autocorrelation function in the time domain for each path. As a particular case where all the paths in all the subchannels follow the Jakes model, the impulse response of this filter is $\Gamma(3/4)(f_{\max}/(\pi|(k - tFilter/2)T_s|))^{1/4} J_{1/4}(f_{\max}|(k - tFilter/2)T_s|)$, where $\Gamma(\cdot)$ is the gamma function, $tFilter$ is the length of the filter, and $k = 0, \dots, tFilter$ is an index that enumerates the coefficients [22]. In order to perform the noise filtering, a custom function, named `convolution`, was coded; it receives pointers to arrays of 2-vectors corresponding to the noise and Doppler filter

```
VEX_FUNCTION_D(cl_double2, convolution,
               (size_t, i) (cl_double2*, x)
               (double*, y) (int, tF) (int, fS)
               (int, nS) (int, nP), (csum)
               (cmulscalar),
               double2 sum = {0.0, 0.0});
int tmp1 = i+(i/fS) * (nS-fS);
int tmp2 = tF * (i/(fS*nP)+1) - 1;
for(size_t j = 0; j < tF; j++)
    sum = csum(sum,
               cmulscalar(x[tmp1+j], y[tmp2-j]));
return sum;
);
```

LISTING 3: Filtering code.

coefficients, respectively. The code used for this convolution is presented in Listing 3, where `i` is the OpenCL's element index, `x` is the noise, `y` is the filter, `tF` is the length of the filter, `fS` is the number of samples to be filtered, `nS` is the number of samples, and `nP` is the number of paths. The convolution function processes in parallel the complete noise vector. It executes the function body for each noise sample.

3.2.3. Path Gains. They are implemented as the product of a vector and a scalar. Each path has its own gain.

3.2.4. Upsampling. The upsampling is a quadratic interpolation to a desired number of values of the noise vector.

3.2.5. Tap Generation. The resulting noise vector, representing the paths, is correlated with a matrix $\mathbf{G}_{i,j}$ (e.g., raised cosine). This correlation is implemented as a matrix-matrix product. A MIMO system has multiple channels; the correlation is done for each channel.

3.3. Data Frame Processing. This section describes the implementation of Figure 1 and (1): a transmitter and a receiver correlation stage and the discrete time-varying channel impulse response from the transmitter i to the receiver j .

3.3.1. Transmitter Correlation. The correlation on the transmitter side is implemented as a product of the data $\mathbf{x}(n)$ and correlation matrices \mathbf{C}_T ; the latter matrix contains the coefficients that correlate data frames and the transmit antennas.

3.3.2. FIR Filter. The transmitted data frames are filtered with the channel coefficients, $\mathbf{H}(n)$, described in Section 3.2. In order to achieve this goal, a convolution is implemented. The code used for this convolution is presented in Listing 4, where the variable `i` is the OpenCL's element index, the variable `x` is a pointer to the data to be processed, the variable `y` is a pointer to the generated channel coefficients, the variable `tRc` is the number of taps of the raised cosine, the variable `nD` is the data frame size, the variable `uS` is the size of the path, the variable

```

VEX_FUNCTION_D(c1_double2, convolution2,
(size_t, i) (c1_double2*, x)
(c1_double2*, y) (int, tRc) (int, nD)
(int, uS) (int, nT) (int, nR), (cmul)
(csum),
double2 sum = {0.0, 0.0};
int tmp1 = i/nD;
int tmp2 = i/nD;
int ext = uS * tRc;
int limt = tRc;
if(tmp1 < tRc)
    limt = tmp1 + 1;
for(size_t k=0; k<nT; k++)
    for(size_t j=0; j<limt; j++)
        sum = csum(sum, cmul(
            x[tmp1-j+k*nD],
            y[tmp1+j*uS+ext*(k*nR+tmp2)]
        ));
return sum;
);

```

LISTING 4: Convolution code.

TABLE 1: Power delay profiles for configuring the SISO subchannels of the MIMO 2×2 simulator.

Subchannel	Delay (nsec)
$\mathbf{h}_{1,1}$	[0, 310, 710, 1090, 1730, 2510]
$\mathbf{h}_{1,2}$	[0, 300, 8900, 12900, 17100, 20000]
$\mathbf{h}_{2,1}$	[0, 4450, 8900, 12300]
$\mathbf{h}_{2,2}$	[400, 710, 800, 920, 1200]
Gain (dB)	
$\mathbf{h}_{1,1}$	[0, -1, -9, -10, -15, -20]
$\mathbf{h}_{1,2}$	[-2.5, 0, -12.8, -10, -25.2, -16]
$\mathbf{h}_{2,1}$	[0, -1, -5, -8]
$\mathbf{h}_{2,2}$	[-2, 0, -2, -8, -9]

nT is the number of transmitters, and the variable nR is the number of receivers.

3.3.3. Receiver Correlation. The correlation on the receiver side is implemented as a product of the received data and the correlation matrix \mathbf{C}_R ; the latter matrix contains the coefficients that correlate data frames and the receive antennas.

4. Results

In this section, the time performance of the proposed simulator is evaluated. In order to achieve this goal, a MIMO 2×2 channel is considered, where all the subchannels have the same PDS with Jakes shape and $f_{\max} = 2000$ Hz. If a carrier frequency of 5.9 GHz is considered, then the assumed f_{\max} corresponds to a scenario where the speed of the mobile is 360 km/h. Likewise, the PDP of each SISO subchannel is fixed as described in Table 1. The PDPs are selected in order to prove the functionality of the simulator, with the

TABLE 2: Time consumption by each module of the proposed simulator considering an 8×8 MIMO simulator.

Module	Time (%)
Multiple matrix-matrix multiplications	74.23
Simulation	19.55
Upsampling	3.62
Gaussian random number generator	1.25
Doppler filter	.92
Path gain	.43

PDPs of $\mathbf{h}_{1,1}$ and $\mathbf{h}_{1,2}$ corresponding to the vehicular test environment channel A and channel B as defined in [23] respectively. The values of matrices \mathbf{C}_R and \mathbf{C}_T are fixed in such a way that they make $[\mathbf{C}_R \mathbf{C}_R^H]_{i,j} = 0.3^{|i-j|}$ and $[\mathbf{C}_T \mathbf{C}_T^H]_{i,j} = 0.9^{|i-j|}$, respectively [24]. It is assumed that the transmitter and the receiver filters are both a square root raised cosine with a rolloff factor of 0.5 and the duration of its convolution is $2T_B = 6T_s$, where the period symbol is fixed at $T_s = 0.1 \mu\text{s}$. According to the maximum delay values presented in Table 1, as well as the values of T_B and T_s , the parameter L is equal to 206 taps. Finally, the MIMO simulator generates channels assuming data frames composed of 1024 symbols.

Figure 3 shows a parallel realization of each MIMO subchannel using the proposed GPU-based simulator, where each of the subfigures presents the time-variation of the corresponding filter coefficients, which are associated with the assigned PDS. Moreover, it is possible to observe that each subchannel satisfies the specifications of the PDP assigned. Thus, PDPs with large delays correspond to filters with more coefficients, as observed in the channel realizations $\mathbf{h}_{1,2}$ and $\mathbf{h}_{2,1}$, respectively.

The time performance evaluation is carried out using a personal computer (PC) with the following specifications:

- (i) Fedora 25, 64 bits
- (ii) Intel core i7-920 (2.66 GHz)
- (iii) 12 GB DDR3 RAM
- (iv) Graphics card Asus GTX Titan Black with 6 GB of RAM and 2880 CUDA cores.

In order to evaluate the time performance, 15 different scenarios of triply selective $N_R \times N_T$ MIMO channels are considered: 2×2 , 3×3 , 4×4 , 5×5 , 6×6 , 7×7 , 8×8 , 10×10 , 12×12 , 14×14 , 16×16 , 18×18 , 20×20 , 22×22 , and 24×24 . For all the cases, it is assumed that all the subchannels are configured with the same PDP (vehicular test environment channel B) and PDS (Jakes with $f_{\max} = 2000$ Hz) statistics; moreover, the matrices \mathbf{C}_T and \mathbf{C}_R have identical values which make $[\mathbf{C}_T \mathbf{C}_T^H]_{i,j} = [\mathbf{C}_R \mathbf{C}_R^H]_{i,j} = 0.5^{|i-j|}$ for $i = 1, \dots, N_R$ and $i = 1, \dots, N_T$. The rest of the simulation parameters have the same values as described previously.

The simulations are carried out over 100 frames and the elapsed processing time per frame is obtained by averaging all the frames. Table 2 shows the time required to execute each of the simulator blocks.

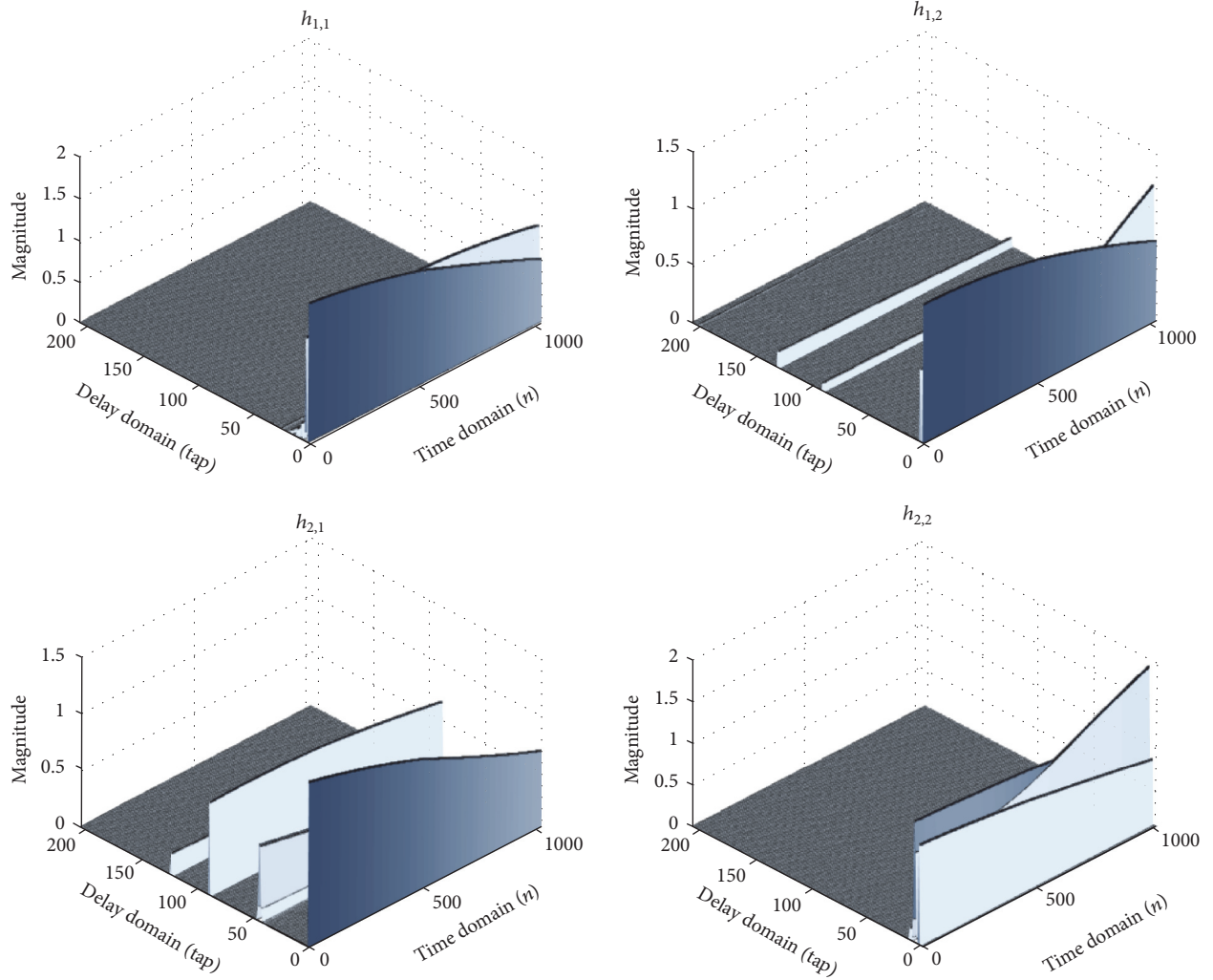


FIGURE 3: MIMO channel realizations.

Figure 4 presents the comparison of the time required to execute all the considered cases when the GPU-based simulator is used, as well as the sequential implementation of this simulator using C language. For a better appreciation, the results are plotted in logarithmic scale.

Table 3 summarizes the time consumption and also presents the x -fold time gain. This gain is calculated as the quotient of the time required by the sequential implementation divided by the GPU implementation. It is possible to observe that for the cases from 2×2 to 7×7 , as the complexity of simulator increments, the gain increments too. This is due to the fact that as more operations are required, better utilization of the parallel resources of the GPU is achieved. In the remaining cases, the gain is around 680; starting at the 7×7 case, the simulator simultaneously uses the available resources in the device. As a matter of fact, with the GPU considered for testing the simulator, the 24×24 case is the most complex MIMO channel that can be simulated; nevertheless, if the hardware is upgraded, then this inconvenience can be addressed, opening the possibility for the simulation of more complex scenarios, for example, massive MIMO.

4.1. Discussion. Recently, several channel simulator approaches have been introduced in the open literature. However, these implementations are based on field programmable gate array (FPGA) devices, and they are restricted to using a single configuration in the developed simulator; that is, the time- and frequency-selective correlations are fixed. As a result, setting new channel statistics in the simulator (new channel propagation conditions) implies the redesign of the implemented hardware. For example, in the channel simulator introduced by [16], the time selectivity is generated by using a sum of sinusoids, which approximates a Jakes PDS. This simulator uses uniform random number generators for defining the configuration of the parameters of these sinusoids. Thus, if one wishes to generate a channel with a different PDS, then this will imply changing the probability density function of the random number generator block. In contrast, for changing the statistics of the simulator proposed in this paper, it is necessary only to upgrade the coefficients of the filters, which allows for a quick redesign of the simulator.

As regards performance, even though the reported FPGA implementations can operate in real time, they are constrained in terms of the number of operations that they

TABLE 3: Time consumption for different MIMO channel realizations when the GPU-based simulator and a sequential implementation are used.

MIMO Size	GPU Implementation (ns)	Sequential Implementation (ns)	x -fold Gain
2×2	1703	504223	296
3×3	2456	1139590	464
4×4	3719	2037134	547
5×5	5318	3176655	597
6×6	7049	4578364	649
7×7	9096	6266204	688
8×8	12542	8160310	650
10×10	18854	12726565	675
12×12	26093	18376942	704
14×14	35766	25051177	700
16×16	50766	32819589	646
18×18	62645	41863632	668
20×20	75303	51563394	684
22×22	91884	62385816	678
24×24	110943	74266271	669

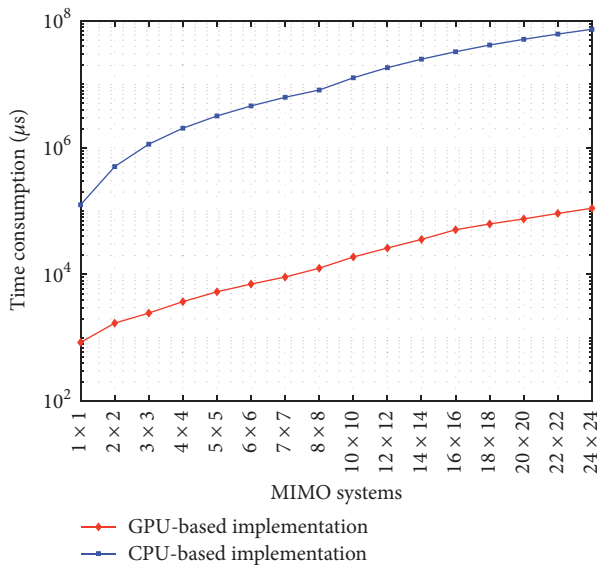


FIGURE 4: Comparison of execution time for different MIMO channels.

can execute. For example, in [16] it is reported that the MIMO channels which can be simulated should be limited to $N_R \times N_T \times L \leq 160$ total taps. Meanwhile, the tests performed on the proposed simulator with the selected GPU device reveal that the most complex channel that can be simulated contains 118656 total taps ($24 \times 24 \times 206$). Moreover, the implementations presented in the open literature for achieving the reported performance consider that the paths of the PDP occur in multiples of the symbol period and all the subchannels share the same PDP. This contrasts with our GPU-based implementation, which can deal with paths with arbitrary positions and distinct PDPs for

each subchannel. This is noteworthy because communication standards recommend PDPs with paths whose allocations are symbol period independent, while the flexibility of setting different PDPs for each subchannel makes it possible to simulate more complex scenarios. If the constraints assumed in the reported simulators were considered, then the proposed simulator could generate more total taps and consequently MIMO channels with larger numbers of antennas.

5. Conclusions

This paper presents a methodology for implementing a triply selective MIMO simulator based on GPUs. The proposed simulator considers the use of multiple SISO simulators, which are also implemented with GPUs, together with input and output correlation matrices in order to provide the corresponding space selectivity. This approach allows for great flexibility because each SISO subchannel can be set with different statistics and, therefore, more complex environments can be modeled. It is shown that under some considerations, the scheme fits with the more specific model proposed in the state of the art. Moreover, the implementations with GPUs considerably reduce the execution time compared with sequential implementations. Implementation results show a 688-fold gain for MIMO 7×7 when compared with sequential implementations. This suggests that this approach will enable more complex MIMO channels to be simulated with a greater number of antennas and a minimum penalty of time execution; in this way, communication systems can be tested in less time. Likewise, the considered model allows for the simulation of different scenarios, which are not forced to have the same statistics in each subchannel. Therefore, it becomes possible to simulate propagation environments that are more adequate for V2I and V2V communication systems.

Appendix

Implemented Codes

See Listings 1–4.

Conflicts of Interest

The authors declare that there are no conflicts of interest regarding the publication of this article.

Acknowledgments

This work was financed by the Mexican Council for Science and Technology (CONACYT) through the SEP-CONACYT Basic Research Program (no. 241272).

References

- [1] A. Goldsmith, *Wireless Communications*, Cambridge University Press, New York, NY, USA, 2005.
- [2] G. L. Stüber, *Principles of Mobile Communication*, Springer, New York, NY, USA, 3rd edition, 2012.
- [3] M. Pätzold, *Mobile Radio Channels*, Wiley, Chichester, UK, 2nd edition, 2011.
- [4] B. Talha and M. Pätzold, “Channel models for mobile-to-mobile cooperative communication systems: a state of the art review,” *IEEE Vehicular Technology Magazine*, vol. 6, no. 2, pp. 33–43, 2011.
- [5] J. Vázquez Castillo, L. Vela-García, C. Gutiérrez, and R. Parra-Michel, “A reconfigurable hardware architecture for the simulation of Rayleigh fading channels under arbitrary scattering conditions,” *AEÜ - International Journal of Electronics and Communications*, vol. 69, no. 1, pp. 1–13, 2015.
- [6] L. Vela-García, J. V. Castillo, R. Parra-Michel, and M. Pätzold, “An accurate hardware sum-of-cisoids fading channel simulator for isotropic and non-isotropic mobile radio environments,” *Modelling and Simulation in Engineering*, vol. 2012, Article ID 542198, 12 pages, 2012.
- [7] J. P. Kermaol, L. Schumacher, K. I. Pedersen, P. E. Mogensen, and F. Frederiksen, “A stochastic MIMO radio channel model with experimental validation,” *IEEE Journal on Selected Areas in Communications*, vol. 20, no. 6, pp. 1211–1226, 2002.
- [8] W. Weichselberger, M. Herdin, H. Özcelik, and E. Bonek, “A stochastic MIMO channel model with joint correlation of both link ends,” *IEEE Transactions on Wireless Communications*, vol. 5, no. 1, pp. 90–99, 2006.
- [9] R. Carrasco-Alvarez, J. Vázquez Castillo, A. Castillo Atoche, and J. Ortegón Aguilar, “A fading channel simulator implementation based on GPU computing techniques,” *Mathematical Problems in Engineering*, vol. 2015, Article ID 237061, 8 pages, 2015.
- [10] J. Tan, Z. Su, and Y. Long, “A full 3-D GPU-based beam-tracing method for complex indoor environments propagation modeling,” *IEEE Transactions on Antennas and Propagation*, vol. 63, no. 6, pp. 2705–2718, 2015.
- [11] Z. B. Loo, P. K. Chong, K. Y. Lee, and W.-S. Yap, “Improved path loss simulation incorporating three-dimensional terrain model using parallel coprocessors,” *Wireless Communications and Mobile Computing*, vol. 2017, Article ID 5492691, 11 pages, 2017.
- [12] Z. Yun and M. F. Iskander, “Ray tracing for radio propagation modeling: Principles and applications,” *IEEE Access*, vol. 3, pp. 1089–1100, 2015.
- [13] S. Roger, C. Ramiro, A. Gonzalez, V. Almenar, and A. M. Vidal, “Fully parallel GPU implementation of a fixed-complexity soft-output MIMO detector,” *IEEE Transactions on Vehicular Technology*, vol. 61, no. 8, pp. 3796–3800, 2012.
- [14] C. Zhang, L. Liu, D. Marković, and V. Öwall, “A heterogeneous reconfigurable cell array for MIMO signal processing,” *IEEE Transactions on Circuits and Systems I: Regular Papers*, vol. 62, no. 3, pp. 733–742, 2015.
- [15] Y. Karasawa, K. Nakada, G. Sun, and R. Kotani, “MIMO Fading Emulator Development with FPGA and Its Application to Performance Evaluation of Mobile Radio Systems,” *International Journal of Antennas and Propagation*, vol. 2017, Article ID 4194921, 15 pages, 2017.
- [16] F. Ren and Y. R. Zheng, “A novel emulator for discrete-time MIMO triply selective fading channels,” *IEEE Transactions on Circuits and Systems I: Regular Papers*, vol. 57, no. 9, pp. 2542–2551, 2010.
- [17] A. Alimohammad and S. F. Fard, “A compact architecture for simulation of spatio-temporally correlated MIMO fading channels,” *IEEE Transactions on Circuits and Systems I: Regular Papers*, vol. 61, no. 4, pp. 1280–1288, 2014.
- [18] K. Yu and B. Ottersten, “Models for MIMO propagation channels: a review,” *Wireless Communications and Mobile Computing*, vol. 2, no. 7, pp. 653–666, 2002.
- [19] D. Demidov, *VexCL – a vector expression template library for OpenCL/CUDA*, 2017, <https://github.com/ddemidov/vexcl>.
- [20] D. E. S. Research, *Random123*, 2017, https://www.deshawresearch.com/resources_random123.html.
- [21] J. K. Salmon, M. A. Moraes, R. O. Dror, and D. E. Shaw, “Parallel random numbers: As easy as 1, 2, 3,” in *Proceedings of 2011 International Conference for High Performance Computing, Networking, Storage and Analysis*, pp. 16:1–16:12, ACM, New York, NY, USA, 2011.
- [22] C.-D. Iskander, “A MATLAB-based objectoriented approach to multipath fading channel simulation,” Hi-Tek Multisystems, 2008.
- [23] “TR 101 112 V3.1.0,” Tech. Rep, 2008, http://www.etsi.org/deliver/etsi_tr/101100_101199/101112/03.01.00_60/tr_101112v030100p.pdf.
- [24] “3GPP TR 36.817 V10.0.0,” Tech. Rep, 2011, <http://www.qtc.jp/3GPP/Specs/36817-a00.pdf>.

Research Article

A Novel Simulation Model for Nonstationary Rice Fading Channels

Kaili Jiang,¹ Xiaomin Chen ,¹ Qiuming Zhu ,^{1,2} Lele Chen,¹ Dazhuan Xu,¹ and Bing Chen ¹

¹Jiangsu Key Laboratory of Internet of Things and Control Technologies, Nanjing University of Aeronautics and Astronautics, Nanjing 211106, China

²Institute of Sensors, Signals and Systems, School of Engineering & Physical Sciences, Heriot-Watt University, Edinburgh EH14 4AS, UK

Correspondence should be addressed to Qiuming Zhu; zhuqiuming@nuaa.edu.cn

Received 28 September 2017; Revised 7 December 2017; Accepted 19 December 2017; Published 18 January 2018

Academic Editor: Carlos A Gutierrez

Copyright © 2018 Kaili Jiang et al. This is an open access article distributed under the Creative Commons Attribution License, which permits unrestricted use, distribution, and reproduction in any medium, provided the original work is properly cited.

In this paper, we propose a new simulator for nonstationary Rice fading channels under nonisotropic scattering scenarios, as well as the improved computation method of simulation parameters. The new simulator can also be applied on generating Rayleigh fading channels by adjusting parameters. The proposed simulator takes into account the smooth transition of fading phases between the adjacent channel states. The time-variant statistical properties of the proposed simulator, that is, the probability density functions (PDFs) of envelope and phase, autocorrelation function (ACF), and Doppler power spectrum density (DPSD), are also analyzed and derived. Simulation results have demonstrated that our proposed simulator provides good approximation on the statistical properties with the corresponding theoretical ones, which indicates its usefulness for the performance evaluation and validation of the wireless communication systems under nonstationary and nonisotropic scenarios.

1. Introduction

The channel simulator has the ability to reproduce the statistical properties of propagation channels and has become a very important software-assisted tool for the performance evaluation of wireless communication systems. There are a number of research papers on designing accurate and efficient simulators [1–19]. For the good fitting with plan-wave propagation channels, the sum-of-sinusoids (SoS) [1, 2] or sum-of-cisoids (SoC) [3] based simulators and their derivatives [4–8] have gained the most widespread acceptance.

It should be highlighted that the traditional SoC simulators are only suitable to reproduce wide-sense stationary (WSS) fading channels, which means the statistical properties of output channels are time-invariant. However, measurement campaigns have proved that the WSS assumption is only valid for a short time interval [20]. Therefore, several modified SoC-based simulators were proposed in [9–19] to generate nonstationary fading channels. For example, the WINNER+ model [9] was simulated by generating several

independent channel segments with different simulation parameters. Simulation parameters were updated according to the fixed trajectories of transceivers and clusters in [10, 11, 13, 14], which improves the continuity of adjacent channel states.

However, we have found that the generated channel phases of these simulators in [9–11, 13, 14] cannot guarantee a smooth transition between adjacent channel states, which makes the output Doppler frequency shifts not very accurate. To overcome this shortcoming, a new method, namely, sum of frequency modulation signals [12, 15–18] or sum of chirp signals [19], was proposed to simulate nonstationary Rayleigh channels very recently, but it lacked implementation details and performance analyses. To fill this gap, this paper develops a new simulator based on this idea to generate the nonstationary Rice fading channels under nonisotropic scattering scenarios, as well as the upgraded computation methods of simulation parameters. Moreover, the time-variant statistical properties of the proposed simulator, that is, the probability density functions (PDFs) of the envelope

and phase, autocorrelation function (ACF), and Doppler power spectral density (DPSD), are derived in detail and also verified by numerical simulations.

The rest of this paper is organized as follows. In Section 2, we introduce the reference model and traditional SoC simulators for stationary fading channels. Section 3 proposes a new simulator for the nonstationary Rice channels, as well as computation methods of the time-variant simulation parameters. The theoretical results of PDF, ACF, and DPSD for the proposed simulator are derived in detail in Section 4. In Section 5, simulation results are given and compared with the corresponding derivation results. Finally, conclusions are drawn in Section 6.

2. Reference and Simulation Models for Stationary Fading Channels

Under the nonstationary condition, the reference model for Rice fading channels can be written as [3]

$$v(t) = \sqrt{\frac{\Omega_v}{K+1}} \mu(t) + \sqrt{\frac{K\Omega_v}{K+1}} m(t), \quad (1)$$

where Ω_v and K are the mean power and Rice factor, and the non-line-of-sight (NLOS) component $\mu(t)$ denotes a normalized zero-mean complex Gaussian process. In (1), $m(t) = \exp(j(2\pi f_\rho t + \theta_\rho))$ represents the line-of-sight (LOS) component, where f_ρ and θ_ρ are the Doppler frequency and phase of the LOS component, respectively. From (1), we can easily obtain the reference model for Rayleigh fading channels by omitting the LOS component ($K = 0$).

The characteristics of reference model are determined by its first- and second-order statistical properties, that is, PDF, ACF, and DPSD. Given the envelope $\xi(t) \triangleq |v(t)|$ and phase $\vartheta(t) \triangleq \arg\{v(t)\}$, the reference PDFs can be expressed as [3]

$$p_\xi(z) = \frac{2z(K+1)}{\Omega_v} e^{-z^2(K+1)/\Omega_v - K} \quad (2)$$

$$\cdot I_0\left(\frac{2z}{\sqrt{\Omega_v}} \sqrt{K(K+1)}\right), \quad z \geq 0$$

$$p_\vartheta(\theta) = \frac{e^{-K}}{2\pi} \left\{ \left[1 + \operatorname{erf}\left(\sqrt{K} \cos(\theta - 2\pi f_\rho t - \theta_\rho)\right) \right] \cdot \sqrt{K\pi} \cos(\theta - 2\pi f_\rho t - \theta_\rho) e^{K \cos^2(\theta - 2\pi f_\rho t - \theta_\rho)} + 1 \right\} \quad (3)$$

$$0 \leq \theta < 2\pi,$$

where $I_0(\cdot)$ and $\operatorname{erf}(\cdot)$ denote the modified Bessel function of the first kind of order zero and complementary error function, respectively. The ACF of $v(t)$ is defined by $r_{vv}(\tau) = E\{v^*(t)v(t+\tau)\}$, where $E\{\cdot\}$ and $(\cdot)^*$ denote the statistical expectation and complex conjugation operator, respectively. Finally, the DPSD can be obtained by the Fourier transform of ACF as $S_{vv}(f) = \int_{-\infty}^{\infty} r_{vv}(t, \tau) e^{-j2\pi f \tau} d\tau$. For nonisotropic scattering scenarios, the von Mises (VM) distribution is

widely accepted to describe the angle of arrival (AoA) [8] and is given by

$$p_\alpha(\alpha) = \frac{e^{\kappa \cos(\alpha - m_\alpha)}}{2\pi I_0(\kappa)}, \quad (4)$$

where $\kappa > 0$ controls the angular spread and $m_\alpha \in (-\pi, \pi]$ denotes the mean value. Under the stationary VM scattering scenario, the references ACF and DPSD have been derived as [8]

$$r_{vv}(\tau) = \frac{\Omega_v I_0\left(\sqrt{\kappa^2 - (2\pi f_{\max} \tau)^2} + j4\pi \kappa f_{\max} \cos(m_\alpha) \tau\right)}{(K+1) I_0(\kappa)} + \frac{K\Omega_v}{K+1} e^{j2\pi f_\rho \tau}, \quad (5)$$

$$S_{vv}(f) = \frac{\Omega_v \operatorname{rect}(f) \cosh\left(\kappa \sin(m_\alpha) \sqrt{1 - (f/f_{\max})^2}\right) e^{\kappa \cos(m_\alpha) f/f_{\max}}}{\pi f_{\max} (K+1) I_0(\kappa) \sqrt{1 - (f/f_{\max})^2}} + \frac{K\Omega_v \delta(f - f_\rho)}{K+1}, \quad (6)$$

where $f_{\max} = v f_c / c$ denotes the maximum Doppler frequency and v , c , and f_c are the movement speed, light speed, and carrier frequency, respectively.

The traditional SoC simulator can be expressed as [8]

$$\hat{v}(t) = \sqrt{\frac{\Omega_v}{K+1}} \underbrace{\sum_{n=1}^N \sqrt{\frac{1}{N}} e^{j(2\pi \hat{f}_n t + \hat{\theta}_n)}}_{\hat{\mu}(t)} + \sqrt{\frac{K\Omega_v}{K+1}} \underbrace{e^{j(2\pi \hat{f}_\rho t + \hat{\theta}_\rho)}}_{\hat{m}(t)}, \quad (7)$$

where N is the number of simulation paths, \hat{f}_n , \hat{f}_ρ , $\hat{\theta}_n$, and $\hat{\theta}_\rho$ are the time-invariant simulation parameters, mean Doppler frequencies, initial phases of the NLOS, and LOS component, respectively. Note that the frequency parameters \hat{f}_n , $n = 1, \dots, N$ and \hat{f}_ρ are determined by the ACF or DPSD of the reference model, while the phase $\hat{\theta}_n$, $n = 1, \dots, N$ and $\hat{\theta}_\rho$ are generated randomly and uniformly over $(0, 2\pi]$.

3. A New Simulator for Nonstationary Fading Channels

Under the nonstationary condition, the statistical properties of channels would change over time [20], and this makes channel parameters time-variant. In order to apply the classic SoC method, some modified simulators [9–11, 13, 14] directly use $2\pi \hat{f}_n(t)t$ and $2\pi \hat{f}_\rho(t)t$ to substitute $2\pi \hat{f}_n t$ and $2\pi \hat{f}_\rho t$ in (7), respectively. However, it can be proved that the output phases of these models are not accurate and the output Doppler frequencies do not agree with the theoretical ones [18]. In this

paper, we use $2\pi \int_0^t f_n(t') dt'$ and $2\pi \int_0^t f_\rho(t') dt'$ to replace $2\pi f_n(t)t$ and $2\pi f_\rho(t)t$, respectively, and the new simulator can be written as

$$\begin{aligned} \tilde{v}(t) = & \sqrt{\frac{\tilde{\Omega}_v(t)}{\tilde{K}(t)+1}} \underbrace{\sum_{n=1}^N \sqrt{\frac{1}{N}} e^{j(2\pi \int_0^t \tilde{f}_n(t') dt' + \tilde{\theta}_n)}}_{\tilde{\mu}(t)} \\ & + \sqrt{\frac{\tilde{K}(t) \tilde{\Omega}_v(t)}{\tilde{K}(t)+1}} \underbrace{e^{j(2\pi \int_0^t \tilde{f}_\rho(t') dt' + \tilde{\theta}_\rho)}}_{\tilde{m}(t)}. \end{aligned} \quad (8)$$

A key issue for the proposed simulator is to find a proper set of simulation parameters $\{\tilde{f}_\rho, \tilde{f}_n\}$, $n = 1, \dots, N$, which can guarantee that the output statistical properties are close to the desired ones. Several parameter computation methods have been proposed in the literature [8, 21–23], such as the Riemann sum method (RSM) [8], the extended method of exact Doppler spread (EMEDS) [21], the generalized method of equal areas (GMEA) [22], and the L_p -norm method [23]. However, these methods are only suitable for the time-invariant parametric simulator. Therefore, an upgraded computation method is required to make the proposed simulator realizable.

Since the WSS assumption is still valid for the nonstationary channels during a short time interval [20], it is reasonable to assume that the statistical properties keep unchanged during a short time duration T_u , namely, the updating interval of channel states. Thus, the parameters $\tilde{\Omega}_v(t)$ and $\tilde{K}(t)$ within the l th interval can be denoted as $\tilde{\Omega}_v^l$ and \tilde{K}^l , where $l = \lfloor t/T_u \rfloor + 1$ ($l = 1, 2, 3, \dots$) and $\lfloor \cdot \rfloor$ means the integer part. The corresponding DPSD within the l th interval can be defined by

$$S_{\tilde{v}\tilde{v}}^l(f) = \frac{\tilde{\Omega}_v^l}{\tilde{K}^l + 1} S_{\tilde{\mu}\tilde{\mu}}^l(f) + \frac{\tilde{K}^l \tilde{\Omega}_v^l}{\tilde{K}^l + 1} S_{\tilde{m}\tilde{m}}^l(f), \quad (9)$$

where $S_{\tilde{\mu}\tilde{\mu}}^l(f)$ and $S_{\tilde{m}\tilde{m}}^l(f)$ are the DPSDs of the NLOS component and LOS component, respectively, and can be obtained by (6) under the VM scattering scenario or measured under other realistic scenarios. Then, by using aforementioned methods [8, 21–23], the frequency parameters of the l th interval, denoted as $\{\tilde{F}_\rho^l, \tilde{F}_n^l\}$, $n = 1, \dots, N$, can be calculated. Hence, the time-variant frequency parameters can be computed by $\tilde{f}_\rho(t) = \tilde{F}_\rho^l$ and $\tilde{f}_n(t) = \tilde{F}_n^l$. Although this computation method is straightforward and has been applied to simulate WINNER+ model [9] and 3GPP-3D model [24], it does not consider the fact that channel properties in reality usually change smoothly along time. On the other hand, measurement campaigns [20] have shown that the stationary interval is very short, that is, 9 ms in 80% of the case and 20 ms in 60% of the case under the high speed train (HST) scenario. In this paper, we assume that the Doppler frequency changes linearly within the stationary interval, so $\tilde{f}_\rho(t)$ can be calculated by

$$\tilde{f}_\rho(t) = \tilde{F}_\rho^l + \frac{\tilde{F}_\rho^{l+1} - \tilde{F}_\rho^l}{T_u} [t - (l-1)T_u]. \quad (10)$$

Taking the fact into account that the simulations of MIMO channels often demand for generating multiple uncorrelated Rayleigh or Rice fading waveforms, the new calculation method of $\tilde{f}_n(t)$ is given as

$$\tilde{f}_n(t) = b_n^l + k_n^l [t - (l-1)T_u] + \Delta_n^l(t), \quad (11)$$

where b_n^l , k_n^l , and $\Delta_n^l(t)$ denote the initial value, the slope, and the small random offset of the frequency parameter of the n th path, respectively. b_n^l ($l = 1$) is generated randomly and uniformly over $[\tilde{F}_{n-1}^1, \tilde{F}_n^1]$, while b_n^l ($l > 1$) holds the value at the end of the previous interval. The slope k_n^l is calculated by

$$k_n^l = \begin{cases} N_{sf} \frac{(\tilde{F}_n^l - \tilde{F}_{n-1}^l) + (\tilde{F}_n^{l+1} - \tilde{F}_{n-1}^{l+1})}{2T_u}, & \tilde{f}_n(t) < B_n^{\text{low}}(t) \\ N_{sf} \frac{(\tilde{F}_{n-1}^l - \tilde{F}_n^l) + (\tilde{F}_{n-1}^{l+1} - \tilde{F}_n^{l+1})}{2T_u}, & \tilde{f}_n(t) > B_n^{\text{upper}}(t), \end{cases} \quad (12)$$

where N_{sf} refers to the number of period within each interval, and the upper boundary $B_n^{\text{upper}}(t)$ and low boundary $B_n^{\text{low}}(t)$ are used to keep the frequencies changing within valid ranges, which are defined by

$$\begin{aligned} B_n^{\text{upper}}(t) &= \tilde{F}_n^l + \frac{(\tilde{F}_n^{l+1} - \tilde{F}_n^l)(t - (l-1)T_u)}{T_u} \\ B_n^{\text{low}}(t) &= \tilde{F}_{n-1}^l + \frac{(\tilde{F}_{n-1}^{l+1} - \tilde{F}_{n-1}^l)(t - (l-1)T_u)}{T_u}. \end{aligned} \quad (13)$$

Note that the parameter computation method in [19] can be viewed as a special case of (11) with $N_{sf} = 1$. To visualize and demonstrate the proposed computation method, let us consider the reference DPSDs of $S_{\tilde{\mu}\tilde{\mu}}(t, f)$ and $S_{\tilde{m}\tilde{m}}(t, f)$ under VM scattering environment as shown in Figure 1. The parameters are configured as follows, $T_u = 10$ ms, $N = 8$, and $N_{sf} = 2$. The frequencies and boundaries can be calculated by using (10)–(13) and are also shown in Figure 1. It is clear that the frequencies are continuous and change linearly within the upper and lower boundaries. The frequencies also include a small and random offset, which is to guarantee the generated multiple fading channels are uncorrelated.

4. Time-Variant Statistical Properties of the Proposed Simulator

4.1. The PDFs of Envelope and Phase. In order to derive the PDFs of envelope and phase for the proposed simulator, let

us set $\tilde{v}(t) = \tilde{v}_1(t) + j\tilde{v}_2(t)$, where $\tilde{v}_1(t)$ and $\tilde{v}_2(t)$ are defined by

$$\begin{aligned} \tilde{v}_1(t) &= \underbrace{\sqrt{\frac{\bar{K}(t)\bar{\Omega}_v(t)}{\bar{K}(t)+1}} \cos\left(2\pi\int_0^t \tilde{f}_\rho(t') dt' + \tilde{\theta}_\rho\right)}_{\bar{m}_1(t)} \\ &+ \underbrace{\sqrt{\frac{\bar{\Omega}_v(t)}{\bar{K}(t)+1}} \sum_{n=1}^N \sqrt{\frac{1}{N}} \cos\left(2\pi\int_0^t \tilde{f}_n(t') dt' + \tilde{\theta}_n\right)}_{\bar{\mu}_1(t)} \end{aligned} \quad (14)$$

$$\begin{aligned} \tilde{v}_2(t) &= \underbrace{\sqrt{\frac{\bar{K}(t)\bar{\Omega}_v(t)}{\bar{K}(t)+1}} \sin\left(2\pi\int_0^t \tilde{f}_\rho(t') dt' + \tilde{\theta}_\rho\right)}_{\bar{m}_2(t)} \\ &+ \underbrace{\sqrt{\frac{\bar{\Omega}_v(t)}{\bar{K}(t)+1}} \sum_{n=1}^N \sqrt{\frac{1}{N}} \sin\left(2\pi\int_0^t \tilde{f}_n(t') dt' + \tilde{\theta}_n\right)}_{\bar{\mu}_2(t)}. \end{aligned}$$

In the following, the joint distribution of $\tilde{v}_1(t)$ and $\tilde{v}_2(t)$ can be expressed as $p_{\tilde{v}_1\tilde{v}_2}(t, z_1, z_2) = p_{\tilde{v}_1}(t, z_1)p_{\tilde{v}_2}(t, z_2)$, where $p_{\tilde{v}_i}(t, z_i)$ denotes the PDF of $\tilde{v}_i(t)$ ($i = 1, 2$) and can be calculated by

$$p_{\tilde{v}_i}(t, z_i) = p_{\bar{\mu}_i}(t, z_i) p_{\bar{m}_i}(t, z_i). \quad (15)$$

$$\begin{aligned} p_{\tilde{\xi}\tilde{\vartheta}}(t, \theta, z) &= z p_{\tilde{v}_1\tilde{v}_2}(t, z \cos \theta, z \sin \theta) = 2\pi z \int_0^\infty \left[\prod_{n=1}^N J_0 \left(2\pi x \sqrt{\frac{\bar{\Omega}_v(t)}{N(\bar{K}(t)+1)}} \right) \right] \\ &\cdot J_0 \left(2\pi x \sqrt{z^2 + \frac{\bar{K}(t)\bar{\Omega}_v(t)}{\bar{K}(t)+1}} - 2z \sqrt{\frac{\bar{K}(t)\bar{\Omega}_v(t)}{\bar{K}(t)+1}} \cos \left(\theta - 2\pi \int_0^t \tilde{f}_\rho(t') dt' - \tilde{\theta}_\rho \right) \right) x dx, \end{aligned} \quad (18)$$

where $z \geq 0$ and $\theta \in (-\pi, \pi)$. Finally, $p_{\tilde{\xi}}(t, z)$ can be obtained by integrating (18) over θ with [26, (6.684-1)] as

$$\begin{aligned} p_{\tilde{\xi}}(t, z) &= \int_{-\pi}^{\pi} p_{\tilde{\xi}\tilde{\vartheta}}(t, \theta, z) d\theta = (2\pi)^2 \\ &\cdot z \int_0^\infty \left[\prod_{n=1}^N J_0 \left(2\pi x \sqrt{\frac{\bar{\Omega}_v(t)}{N(\bar{K}(t)+1)}} \right) \right] \\ &\cdot J_0 \left(2\pi x \sqrt{\frac{\bar{K}(t)\bar{\Omega}_v(t)}{\bar{K}(t)+1}} \right) J_0(2\pi z x) x dx, \quad z \geq 0. \end{aligned} \quad (19)$$

Eq. (19) shows that $p_{\tilde{\xi}}(t, z)$ is completely determined by the parameters of N , $\bar{\Omega}_v(t)$, and $\bar{K}(t)$, whereas the frequency parameters have no influence. Since $\bar{\Omega}_v(t)$ and $\bar{K}(t)$ are fixed at any given time instant, by using [26, (6.618-5)] one

can demonstrate that the PDF tends to the theoretical Rice distribution as (2) with $N \rightarrow \infty$. Similarly, by integrating $p_{\tilde{\xi}\tilde{\vartheta}}(t, \theta, z)$ over z and using [26, (6.52)], the instantaneous phase PDF at any time instant can be proved to tend to the reference PDF as (3).

4.2. ACF. The ACF of nonstationary channels is also no longer time-invariant as (5) and becomes a function of both time lag τ and time t . The time-variant ACF of (8) can be defined as

$$\begin{aligned} r_{\tilde{v}\tilde{v}}(t, \tau) &= E[\tilde{v}(t)\tilde{v}^*(t+\tau)] \\ &= \frac{\bar{\Omega}_v(t)}{\bar{K}(t)+1} r_{\bar{\mu}\bar{\mu}}(t, \tau) \\ &+ \frac{\bar{K}(t)\bar{\Omega}_v(t)}{\bar{K}(t)+1} r_{\bar{m}\bar{m}}(t, \tau), \end{aligned} \quad (20)$$

$$p_{\bar{m}_i}(t, z_i) = \delta(z_i - \bar{m}_i(t)). \quad (16)$$

Using [25, (2.15)] and the relationship between the distribution and the characteristic function, the PDF of $\bar{\mu}_i(t)$ ($i = 1, 2$) can be proved as

$$\begin{aligned} p_{\bar{\mu}_1}(t, z_1) &= \int_{-\infty}^{\infty} \Psi_{\bar{\mu}_1}(t, x) e^{-j2\pi x z_1} dx \\ &= 2 \int_0^\infty \left[\prod_{n=1}^N J_0 \left(2\pi x \sqrt{\frac{\bar{\Omega}_v(t)}{N(\bar{K}(t)+1)}} \right) \right] \\ &\cdot \cos(2\pi x z_1) dx. \end{aligned} \quad (17)$$

Substituting (16) and (17) into (15), we can obtain the joint distribution $p_{\tilde{v}_1\tilde{v}_2}(t, z_1, z_2)$ of two random variables $\tilde{v}_1(t)$ and $\tilde{v}_2(t)$.

Then, let us set $z_1 = z \cos \theta$ and $z_2 = z \sin \theta$ [25]; the time-variant joint PDF of the envelope $\tilde{\xi}(t) = |\tilde{v}(t)|$ and phase $\tilde{\vartheta}(t) = \arg\{\tilde{v}(t)\}$ can be derived as

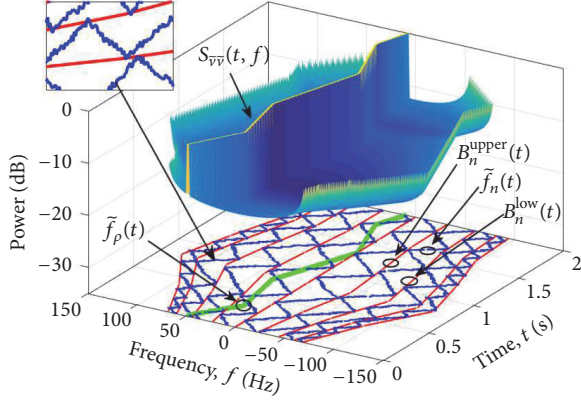


FIGURE 1: The computation method of frequency parameters.

where $r_{\bar{\mu}\bar{\mu}}(t, \tau)$ and $r_{\bar{m}\bar{m}}(t, \tau)$ denote the ACFs of the NLOS component and LOS component, respectively. In reality, the time lag range is much smaller than the updating interval ($\tau \ll T_u$), and $r_{\bar{m}\bar{m}}(t, \tau)$ can be approximately calculated by

$$r_{\bar{m}\bar{m}}(t, \tau) = e^{j2\pi \int_t^{t+\tau} \tilde{f}_\rho(t') dt'} = e^{j\pi\tau(\tilde{f}_\rho(t) + \tilde{f}_\rho(t+\tau))}. \quad (21)$$

The result in (21) clearly shows that the ACF of the LOS component changes over time. It reduces to the corresponding part of reference result as (5) when the frequency parameter $\tilde{f}_\rho(t)$ is constant.

$$r_{\bar{\mu}\bar{\mu}}(t, \tau) = \frac{I_0 \left(\sqrt{\kappa^2 + j2\pi\kappa f_{\max} \tau (\cos(\bar{m}_{\alpha_n}(t)) + \cos(\bar{m}_{\alpha_n}(t) - \Delta_n(t, \tau)))} - 2(\pi f_{\max} \tau)^2 (\cos(\Delta_n(t, \tau)) + 1) \right)}{I_0(\kappa)}. \quad (25)$$

Finally, the theoretical ACF $r_{\bar{v}\bar{v}}(t, \tau)$ of the proposed simulator can be obtained by substituting (21) and (25) into (20).

4.3. *DPSD*. The time-variant DPSD of (8) can be defined as

$$S_{\bar{v}\bar{v}}(t, f) = \frac{\bar{\Omega}_v(t)}{\bar{K}(t) + 1} S_{\bar{\mu}\bar{\mu}}(t, f) + \frac{\bar{K}(t) \bar{\Omega}_v(t)}{\bar{K}(t) + 1} S_{\bar{m}\bar{m}}(t, f). \quad (26)$$

Combining with (10), the DPSD of LOS component can be calculated as

$$S_{\bar{m}\bar{m}}(t, f) = \delta \left(f - \bar{F}_\rho^l - \frac{\bar{F}_\rho^{l+1} - \bar{F}_\rho^l}{T_u} [t - (l-1)T_u] \right). \quad (27)$$

The time-variant ACF of the NLOS component with the VM distribution for AoAs can be expressed as follows:

$$r_{\bar{\mu}\bar{\mu}}(t, \tau) = \frac{1}{2\pi I_0(\kappa)} \int_{-\pi}^{\pi} \sqrt{e^{\kappa \cos(\alpha_n(t) - \bar{m}_{\alpha_n}(t))}} \cdot \sqrt{e^{\kappa \cos(\alpha_n(t+\tau) - \bar{m}_{\alpha_n}(t+\tau))}} e^{j2\pi \int_t^{t+\tau} \tilde{f}_n(t') dt'} d\alpha_n. \quad (22)$$

The distribution factor κ is almost unchanged during a short time interval, so $r_{\bar{\mu}\bar{\mu}}(t, \tau)$ can be simplified by using $\alpha_n(t+\tau) - \bar{m}_{\alpha_n}(t+\tau) \approx \alpha_n(t) - \bar{m}_{\alpha_n}(t)$ as

$$r_{\bar{\mu}\bar{\mu}}(t, \tau) = \frac{1}{2\pi I_0(\kappa)} \int_{-\pi}^{\pi} e^{\kappa \cos(\alpha_n(t) - \bar{m}_{\alpha_n}(t))} \cdot e^{j2\pi \int_t^{t+\tau} f_{\max} \cos(\alpha_n(t')) dt'} d\alpha_n = \frac{1}{2\pi I_0(\kappa)} \cdot \int_{-\pi}^{\pi} e^{\kappa \cos(\alpha_n(t) - \bar{m}_{\alpha_n}(t))} \cdot e^{j\pi f_{\max} \tau (\cos(\alpha_n(t+\tau)) + \cos(\alpha_n(t)))} d\alpha_n, \quad (23)$$

where $\bar{m}_{\alpha_n}(t)$ denotes the mean angle of AoAs. Setting and substituting $\Delta_n(t, \tau) = \alpha_n(t+\tau) - \alpha_n(t)$ into (23), it yields

$$r_{\bar{\mu}\bar{\mu}}(t, \tau) = \frac{1}{2\pi I_0(\kappa)} \int_{-\pi}^{\pi} e^{\kappa \cos(\alpha_n(t) - \bar{m}_{\alpha_n}(t))} \cdot e^{j2\pi f_{\max} \tau \cos(\Delta_n(t, \tau)/2) \cos(\alpha_n(t) + \Delta_n(t, \tau)/2)} d\alpha_n. \quad (24)$$

With the help of [26, (3.338-4)], the closed-form solution of $r_{\bar{\mu}\bar{\mu}}(t, \tau)$ is given as

Base on (11), we can obtain the instantaneous phase caused by the time-variant frequency of NLOS component as

$$\tilde{\phi}_n(t) = 2\pi \int_0^t \tilde{f}_n(x) dx = 2\pi \left(b_n^l t - (l-1) k_n^l T_u t + \frac{k_n^l}{2} t^2 \right). \quad (28)$$

Substituting (28) into (8), the NLOS component can be rewritten as

$$\bar{\mu}(t) = \sum_{n=1}^N \sqrt{\frac{1}{N}} e^{j[2\pi(b_n^l t - (l-1)k_n^l T_u t + (k_n^l/2)t^2) + \bar{\theta}_n]}. \quad (29)$$

With the help of the Wigner-Ville distribution [19, 27], the DPSD of (29) can be expressed as

$$\begin{aligned}
 W_{\tilde{\mu}\tilde{\mu}}(t, f) &= \sum_{n=1}^N \frac{1}{N} \delta(f - (b_n^l - (l-1)k_n^l T_u + k_n^l)t) \\
 &\quad + 4 \sum_{n=1}^{N-1} \sum_{m=2, m>n}^N \frac{1}{\sqrt{\beta_{nm}}} \cos\left(\frac{\pi}{4} + \alpha_{nm} - \frac{4\pi\gamma_{nm}^2}{\beta_{nm}}\right), \quad (30)
 \end{aligned}$$

where

$$\begin{aligned}
 \alpha_{nm} &= \tilde{\theta}_n - \tilde{\theta}_m + \pi(k_n^l - k_m^l)t^2 \\
 &\quad + 2\pi(b_n^l - b_m^l - (l-1)(k_n^l - k_m^l)T_u)t \\
 \beta_{nm} &= |k_n^l - k_m^l| \\
 \gamma_{nm} &= f - \frac{b_n^l + b_m^l - (l-1)(k_n^l + k_m^l)T_u}{2} - \frac{k_n^l + k_m^l}{2}t. \quad (31)
 \end{aligned}$$

The initial phase is random and uniformly distributed over $(0, 2\pi]$, so the second term in (30) can be removed by averaging over the phases. Therefore, the DPSD of NLOS component can be rewritten as

$$\begin{aligned}
 S_{\tilde{\mu}\tilde{\mu}}(t, f) &= W_{\tilde{\mu}\tilde{\mu}}(t, f)|_{\tilde{\theta}_n} \\
 &= \sum_{n=1}^N \frac{1}{N} \delta(f - (b_n^l - (l-1)k_n^l T_u + k_n^l)t). \quad (32)
 \end{aligned}$$

Finally, substituting (27) and (32) into (26), the theoretical DPSD $S_{\tilde{v}\tilde{v}}(t, f)$ of the proposed simulator can be obtained.

5. Simulation and Validation

We validate the proposed simulator in a typical downlink channel of the mobile communication systems. The base station (BS) and MS are both equipped with normalized omnidirectional antennas, the carrier frequency is 2.4 GHz, and the AoAs follow the VM distribution with $\kappa = 3$. The initial distance between the BS and MS is 140 m, and the MS moves away from the BS with the angle of $\theta = 45^\circ$ and the speed of $v = 20$ m/s. It is also assumed that the LOS and NLOS components exist during the simulation.

The simulator is configured as $N = 32$, $N_{sf} = 10$, and $T_u = 20$ ms. The generated channel phase, fading envelope, and Doppler frequency within 2 s are given in Figure 2. For comparison purpose, the corresponding output results of the simulators in [10, 11, 13, 14] and the theoretical Doppler frequency are also given in the figure. It shows that the output phases of two kinds of simulators are different, which results in the difference of channel envelopes. Moreover, the Doppler frequency of the proposed simulator is much closer to the theoretical one. Submitting $N = 32$ and other channel parameters into (19), the theoretical PDF can be obtained and given in Figure 3. It is clearly showed that the PDF changes

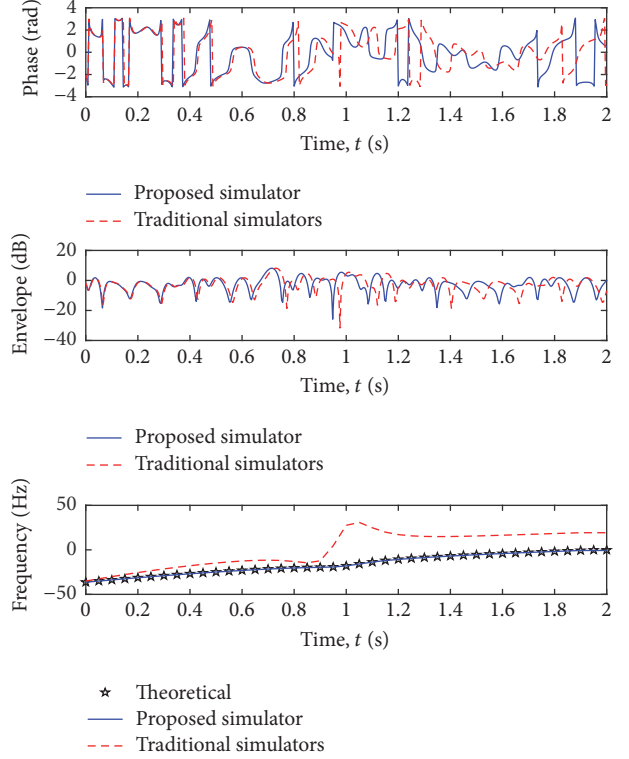


FIGURE 2: Output channel fading phases, envelopes, and Doppler frequencies of the proposed simulator and traditional simulators in [10, 11, 13, 14].

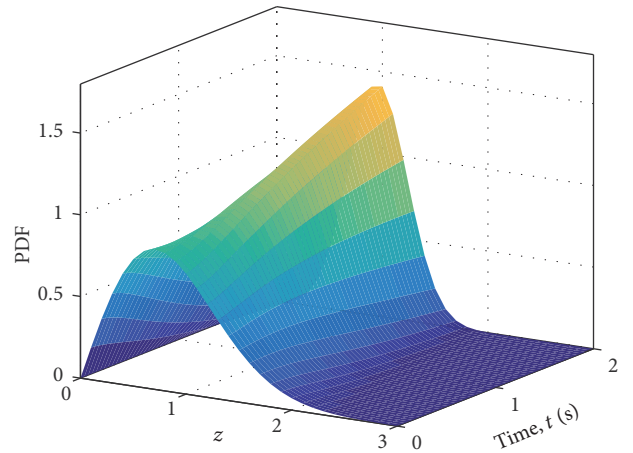


FIGURE 3: Time-variant theoretical PDF of channel fading envelope ($N = 32$).

over time due to the time-variant channel parameters. In addition, the output PDFs of the proposed simulator at three time instants $t = 0$ s, 1 s and 2 s are compared with the corresponding theoretical results in Figure 4. The reference PDFs which can be viewed as the theoretical results with $N = \infty$ are also given in Figure 4. It is showed that the simulated results match well with the corresponding theoretical and reference ones, which verifies the theoretical derivations as well as the simulator.

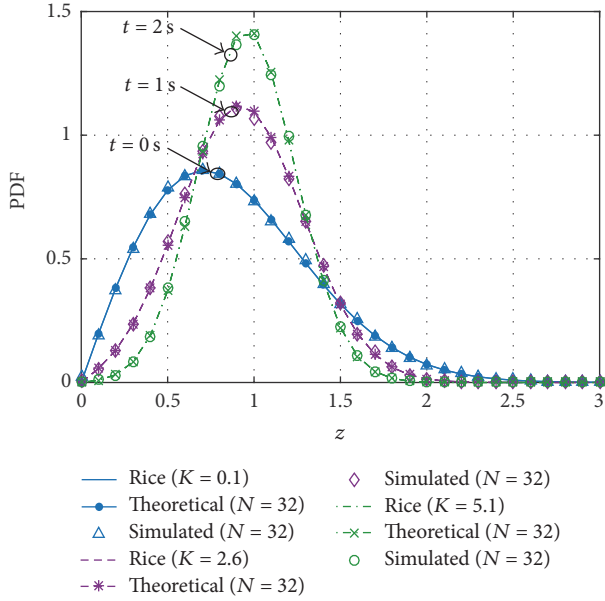


FIGURE 4: Theoretical and simulated PDFs of fading envelopes at different time instants ($f_c = 2.4$ GHz, $\kappa = 3$, $D_0 = 140$ m, $\theta = 45^\circ$, $v = 20$ m/s, $N_{sf} = 10$, $N = 32$, and $T_u = 20$ ms).

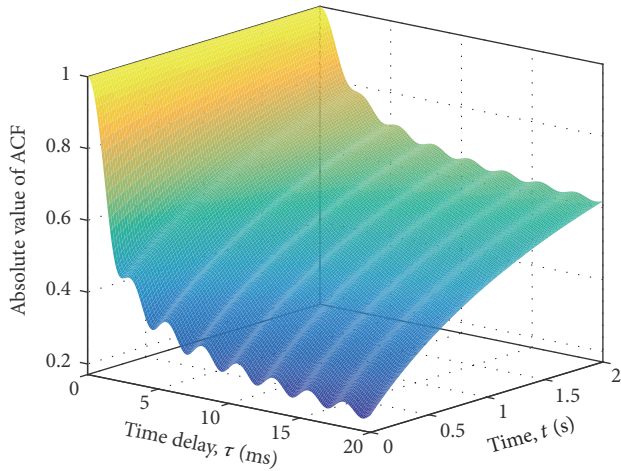


FIGURE 5: Absolute values of the time-variant theoretical ACF ($f_c = 2.4$ GHz, $\kappa = 3$, $D_0 = 140$ m, $\theta = 45^\circ$, and $v = 20$ m/s).

Under the same condition, by using (20), the absolute value of the theoretical ACF is calculated and given in Figure 5. For comparison purpose, the theoretical ACFs at three time instants $t = 0$ s, 1 s, and 2 s are extracted from Figure 5 and the corresponding simulated ACFs are shown in Figure 6. Similarly, the theoretical DPSDs calculated by (26) are given in Figure 7(a) and the simulation results are given in Figure 7(b). Figure 7 clearly demonstrates the time-variety of the LOS component and NLOS components along the trajectory of the MS. It also can be seen that Figure 7 has an asymmetric DPSD, which is the consequence of the nonisotropic scattering condition. In addition, the trends and

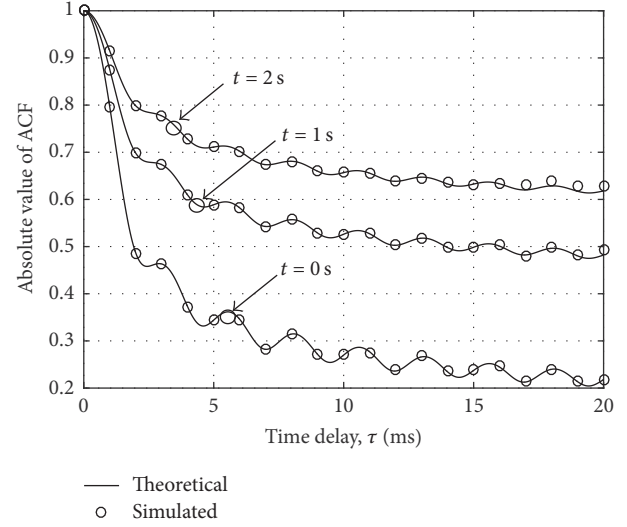


FIGURE 6: Absolute values of theoretical and simulated ACF at different time instants ($f_c = 2.4$ GHz, $\kappa = 3$, $D_0 = 140$ m, $\theta = 45^\circ$, $v = 20$ m/s, $N_{sf} = 10$, $N = 32$, and $T_u = 20$ ms).

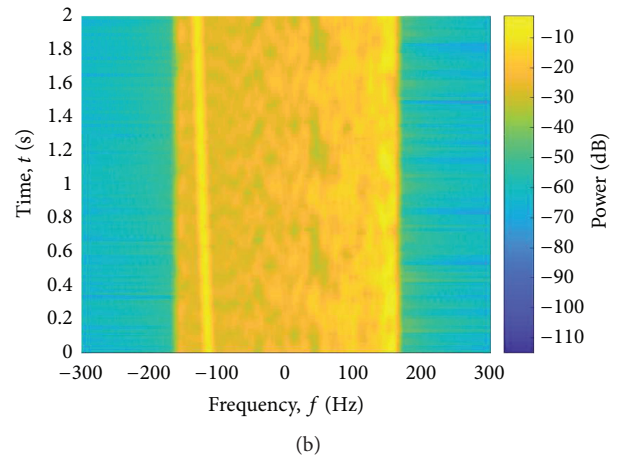
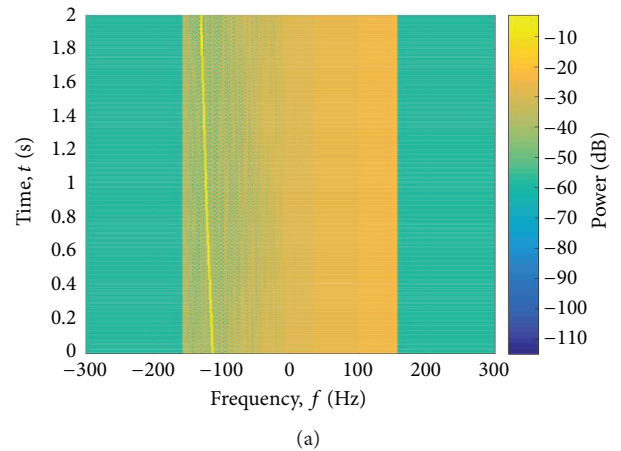


FIGURE 7: (a) Theoretical and (b) simulated time-variant DPSDs ($f_c = 2.4$ GHz, $\kappa = 3$, $D_0 = 140$ m, $\theta = 45^\circ$, $v = 20$ m/s, $N_{sf} = 10$, $N = 32$, and $T_u = 20$ ms).

shapes of theoretical and simulated DPSDs are very similar, which verifies the correctness of both the simulator and derivations. Finally, the good agreements of theoretical and simulated results in Figures 6 and 7 confirm the derivations of (25) and (32), as well as the proposed simulator.

6. Conclusion

Further research on the simple and efficient nonstationary channel simulators is highly desirable for the development and performance evaluation of future wireless communication systems. In this paper, we have presented a new simulator to reproduce the nonstationary Rice fading channels under nonisotropic scattering scenarios. The proposed simulator can also be applied to simulate Rayleigh fading channels by adjusting channel parameters. The computation methods of time-variant simulation parameters, that is, initial phases and frequencies of the LOS component and NLOS component, have been analyzed and given in detail. Based on the new simulator, the theoretical expressions for the PDFs of envelope and phase, ACF, and DPSD under VM distribution scattering environment have also been derived. Finally, the simulation results have demonstrated that our proposed simulator can reproduce the nonstationary fading channels with accurate statistical properties such as PDF, ACF, and DPSD.

Conflicts of Interest

The authors declare that they have no conflicts of interest.

Acknowledgments

This work is supported by Fundamental Research Funds for the Central Universities (Grant no. NS2015046).

References

- [1] R. H. Clarke, "A statistical theory of mobile-radio reception," *Bell Labs Technical Journal*, vol. 47, no. 6, pp. 957–1000, 1968.
- [2] W. C. Jakes, *Microwave Mobile Communications*, Wiley-IEEE Press, Piscataway, NJ, USA, 2nd edition, 1994.
- [3] M. Pätzold, U. Killat, Y. Li, and F. Laue, "Modeling, analysis, and simulation of nonfrequency-selective mobile radio channels with asymmetrical Doppler power spectral density shapes," *IEEE Transactions on Vehicular Technology*, vol. 46, no. 2, pp. 494–507, 1997.
- [4] C.-X. Wang, M. Pätzold, and D. Yuan, "Accurate and efficient simulation of multiple uncorrelated Rayleigh fading waveforms," *IEEE Transactions on Wireless Communications*, vol. 6, no. 3, pp. 833–839, 2007.
- [5] C. Xiao, Y. R. Zheng, and N. C. Beaulieu, "Novel sum-of-sinusoids simulation models for Rayleigh and Rician fading channels," *IEEE Transactions on Wireless Communications*, vol. 5, no. 12, pp. 3667–3679, 2006.
- [6] M. Pätzold, C.-X. Wang, and B. O. Hogstad, "Two new sum-of-sinusoids-based methods for the efficient generation of multiple uncorrelated rayleigh fading waveforms," *IEEE Transactions on Wireless Communications*, vol. 8, no. 6, pp. 3122–3131, 2009.
- [7] A. G. Zajić and G. L. Stüber, "Efficient simulation of rayleigh fading with enhanced de-correlation properties," *IEEE Transactions on Wireless Communications*, vol. 5, no. 7, pp. 1866–1875, 2006.
- [8] C. A. Gutiérrez and M. Pätzold, "The design of sum-of-cisoids rayleigh fading channel simulators assuming non-isotropic scattering conditions," *IEEE Transactions on Wireless Communications*, vol. 9, no. 4, pp. 1308–1314, 2010.
- [9] J. Meinila, P. Kyosti, L. Hentila et al., "WINNER+ final channel models," 2010, <http://projects.celtic-initiative.org/winner+/>.
- [10] A. Ghazal, C.-X. Wang, B. Ai, D. Yuan, and H. Haas, "A nonstationary wideband MIMO channel model for high-mobility intelligent transportation systems," *IEEE Transactions on Intelligent Transportation Systems*, vol. 16, no. 2, pp. 885–897, 2015.
- [11] Y. Yuan, C.-X. Wang, Y. He, M. M. Alwakeel, and E.-H. M. Aggoune, "3D Wideband Non-Stationary Geometry-Based Stochastic Models for Non-Isotropic MIMO Vehicle-to-Vehicle Channels," *IEEE Transactions on Wireless Communications*, vol. 14, no. 12, pp. 6883–6895, 2015.
- [12] A. Borhani, G. L. Stuber, and M. Patzold, "A random trajectory approach for the development of nonstationary channel models capturing different scales of fading," *IEEE Transactions on Vehicular Technology*, vol. 66, no. 1, pp. 2–14, 2016.
- [13] A. Ghaza, Y. Yuan, and C.-X. Wang, "A non-stationary IMT-A MIMO channel model for high-mobility wireless communication systems," *IEEE Trans. Wireless Commun.*, vol. 16, no. 4, pp. 2057–2068, 2017.
- [14] J. Bian, J. Sun, C. Wang et al., "A WINNER+ based 3-D non-stationary wideband MIMO channel model," *IEEE Transactions on Wireless Communications*, 2017.
- [15] Q. Zhu, K. Jiang, X. Chen, C.-X. Wang, X. Hu, and Y. Yang, "A modified non-stationary MIMO channel model under 3D scattering scenarios," in *Proceedings of the IEEE/CIC International Conf. on IEEE*, pp. 1–5, Qingdao, China, 2017.
- [16] W. Dahech, M. Pätzold, C. A. Gutiérrez, and N. Youssef, "A Non-Stationary Mobile-to-Mobile Channel Model Allowing for Velocity and Trajectory Variations of the Mobile Stations," *IEEE Transactions on Wireless Communications*, vol. 16, no. 3, pp. 1987–2000, 2017.
- [17] X. Liu, Q. Zhu, X. Chen, and K. Jiang, "A new simulation model for non-stationary fading channel," in *Proceedings of the 3rd International Conference on Electronic Design, ICED 2016*, pp. 66–69, ta, August 2016.
- [18] Q. Zhu, X. Liu, X. Yin, X. Chen, and C. Xue, "A novel simulator of nonstationary random mimo channels in rayleigh fading scenarios," *International Journal of Antennas and Propagation*, vol. 2016, Article ID 3492591, 2016.
- [19] M. Patzold and C. A. Gutierrez, "The wigner distribution of sum-of-cisoids and sum-of-chirps processes for the modelling of stationary and non-stationary mobile channels," in *Proceedings of the 83rd IEEE Vehicular Technology Conference, VTC Spring 2016*, pp. 1–5, Nanjing, China, May 2016.
- [20] B. Chen, Z. Zhong, and B. Ai, "Stationarity intervals of time-variant channel in high speed railway scenario," *China Communications*, vol. 9, no. 8, pp. 64–70, 2012.
- [21] B. Hogstad, M. Patzold, N. Youssef, and . Dongwoo Kim, "A MIMO mobile-to-mobile channel model: Part II-The simulation model," in *Proceedings of the 16th IEEE PIMRC 2005*, pp. 562–567, Berlin, Germany, 2005.
- [22] C. A. Gutiérrez and M. Pätzold, "The generalized method of equal areas for the design of sum-of-cisoids simulators

- for mobile Rayleigh fading channels with arbitrary Doppler spectra,” *Wireless Communications and Mobile Computing*, vol. 13, no. 10, pp. 951–966, 2013.
- [23] M. Patzold, *Mobile Fading Channels*, John Wiley Sons, Chichester, UK, 2002.
- [24] T. A. Thomas, F. W. Vook, E. Visotsky, E. Mellios, G. S. Hilton, and A. R. Nix, “3D extension of the 3GPP/ITU channel model,” in *Proceedings of the 2013 IEEE 77th Vehicular Technology Conference, VTC Spring 2013*, Dresden, Germany, June 2013.
- [25] A. Papoulis and S. Pillai, *Probability, Random Variables, and Stochastic Processes*, McGraw-Hill, New York, NY, USA, 4th edition, 2002.
- [26] I. S. Gradshteyn and I. M. Ryzhik, *Table of Integrals, Series, and Products*, Academic press, 2014.
- [27] A. Bruscatto and C. M. Toli, “Spectral analysis of non-stationary processes using the Fourier transform,” *Brazilian Journal of Probability and Statistics*, vol. 18, no. 1, pp. 69–102, 2004.